GAZİ ÜNİVERSİTESİ

Gazi

1926

THERMAL DESIGN OF BRAKE DISKS USED IN RAIL VEHICLES

A THESIS SUBMITTED TO
THE GRADUATE SCHOOL OF NATURAL AND APPLIED SCIENCES
OF
GAZİ UNIVERSITY

BY

Yusuf ÇATI

IN PARTIAL FULFILLMENT OF THE REQUIREMENTS
FOR
THE DEGREE OF DOCTOR OF PHILOSOPHY
IN
AUTOMOTIVE ENGINEERING

FEBRUARY 2023

ETHICAL STATEMENT

I hereby declare that in this thesis study I prepared in accordance with thesis writing rules of Gazi University Graduate School of Natural and Applied Sciences;

- All data, information and documents presented in this thesis have been obtained within the scope of academic rules and ethical conduct,
- All information, documents, assessments and results have been presented in accordance with scientific ethical conduct and moral rules,
- All material used in this thesis that are not original to this work have been fully cited and referenced,
- No change has been made in the data used,
- The work presented in this thesis is original,

or else, I admit all loss of rights to be incurred against me.

Yusuf ÇATI
16/02/2023

RAYLI SİSTEM ARAÇLARINDA KULLANILAN FREN DİSKLERİNİN TERMAL YÖNDEN TASARIMI

(Doktora Tezi)

Yusuf ÇATI

GAZİ ÜNİVERSİTESİ
FEN BİLİMLERİ ENSTİTÜSÜ

Şubat 2023

ÖZET

Zorlu koşullar altında fren diski termal davranışının tahmini, acil durum ve sabit hızda frenleme durumları için önemli bir mühendislik problemi haline gelmiştir. Tezin ilk bölümünde, gerçekçi ve zamana bağlı sınır koşulları ile sonlu farklar yöntemi (FDM) kullanılarak bir termal model geliştirilmiştir. Diskteki termal gerilmeler için pratik bir tahmin yöntemi, en yüksek sıcaklığa sahip konumlardan çeşitli zamanlardaki eksenel sıcaklık dağılımları kullanılarak uygulanmıştır. Bunun dışında, modeldeki disk/balata ikilisinin bire bir konfigürasyonu, geliştirilen model ile karşılaştırmak için doğrulanmış bir ticari CFD yazılımı olan Simcenter STAR-CCM+'da modellenmiştir. Bu model kullanılarak, sıcaklığa bağlı malzeme özelliklerinin termal davranış üzerindeki etkisi incelenmiştir. Geliştirilen model, nispeten yeni bir standartta (EN 14535-3) bir demiryolu fren diskinin maruz kaldığı koşulları oldukça hızlı ve makul bir doğrulukla benzeştirebilmektedir. Modeldeki fren diskinin farklı noktalarından alınan veriler ile, 110-160 km/h hız seviyelerinden durma anına kadar ki zamana bağlı sıcaklık dağılımları, ayrıntılı şekilde ortaya konulmuştur. Geliştirilen model Simcenter STAR-CCM+'a göre yaklaşık 94 kat daha hızlı bir şekilde çözüm elde etmektedir. Tezin ikinci bölümünde, deneysel konvektif ısı transferi çalışmaları yürütülmüş ve yeni bir yaklaşımla Nusselt sayısı korelasyonları, yaklaşık 3.75×10^5 dönel Reynolds sayısına kadar belirlenmiştir. Isı transferinin dönen disk üzerindeki akışın kararlılığı üzerindeki etkisi niteliksel olarak gösterilmiştir. Bunun dışında, sabit hızda frenleme durumunda serbest dönen diskin simülasyonu için kompleks bir CFD modeli geliştirilmiş. Bu CFD modelinin yapılan deneylerle doğrulanmıştır. Geliştirilen CFD modelindeki metodoloji kullanılarak düşük dönüş hızı için soğutma kanatçıklarına sahip bir fren diski simüle edilmiştir. CFD modelinin sonuçları, kompleks geometriye sahip fren diskinin gerçekçi test durumunu simüle edebildiği görülmüştür. Tezin çıktıları, fren diskinin acil durumlara yönelik optimizasyon çalışmalarına katkıda bulunacak niteliktedir. Bir diğer katkı ise, yeni deneysel yöntemle doğrulanan CFD modelinden elde edilen Nusselt korelasyonlarının sabit hızda frenleme durumları için hesaplamalarda kullanılabilmesidir.

Bilim Kodu	:	93006
Anahtar kelimeler	:	Raylı araç fren diski, zamana bağlı termal modeli, ısıl gerilme, deneysel konvektif ısı transferi, CFD modellemesi
Sayfa Adedi	:	129
Danışman	:	Prof. Dr. Mesut DÜZGÜN
İkinci Danışman	:	Prof. Dr.-Ing. habil. Stefan aus der WIESCHE

THERMAL DESIGN OF BRAKE DISKS USED IN RAIL VEHICLES

(Ph. D. Thesis)

Yusuf ÇATI

GAZİ UNIVERSITY

GRADUATE SCHOOL OF NATURAL AND APPLIED SCIENCES

February 2023

ABSTRACT

The prediction of brake disk thermal behavior under challenging conditions has become an important engineering issue for emergency and drag braking cases. In the first part of the thesis, a thermal model is developed using the finite difference method (FDM) with realistic and time-dependent boundary conditions. A practical prediction method for thermal stresses in the disk is applied using the axial temperature distributions at several time instants from locations with highest temperature. Apart from that same configuration of the disk with the pad is modelled in Simcenter STAR-CCM+ which is a well-validated commercial CFD software to compare the results. Using this model, an investigation has been conducted on the effect of temperature-dependent material properties on thermal behavior. The developed numerical model can simulate the conditions experienced by a railway brake disk in a relatively new standard (EN 14535-3) with relatively low computational time and reasonable accuracy. Using the data taken from different points of the brake disk in the model, time-dependent temperature and thermal stress distributions from speed levels of 110-160 km/h until the moment of stopping are presented in detail. The developed model obtains a solution approximately 94 times faster than the Simcenter STAR-CCM software. In the second part of the thesis, experimental convective heat transfer studies are conducted and the Nusselt number correlations are determined up to the rotational Reynolds number 3.75×10^5 with a novel approach. The influence of heat transfer on stability of flow over rotating disk is qualitatively shown. Apart from that, a complex CFD model is developed and validated by experiments with the aim of implementation of that CFD model for drag braking case. Finally, brake disk with cooling ribs for a low rotational speed is simulated using the methodology of the developed CFD model. The results of the CFD model shows that it is capable of simulating the realistic test case of brake disk with complex geometry. Outcomes of the thesis contributes to optimization studies of railway brake disk with respect to emergency cases using the developed fast thermal model. Another contribution is that Nusselt correlations can be used for drag braking calculations that are obtained through CFD model which is validated by novel experimental method.

Science Code	:	93006
Key Words	:	Railway brake disk, transient thermal model, thermal stress, experimental convective heat transfer, CFD modeling
Page Number	:	129
Supervisor	:	Prof. Dr. Mesut DÜZGÜN
Co-Supervisor	:	Prof. Dr.-Ing. habil. Stefan aus der WIESCHE

ACKNOWLEDGMENTS

I would like to give my sincere thanks to my advisors Prof. Dr. Mesut Düzgün and Prof. Dr.-Ing. habil. Stefan aus der Wiesche. Also, I thank the members of thesis monitoring committee Prof. Dr. Halit Karabulut and Assoc. Prof. Dr. Serdar Göktepe for their valuable recommendations on this subject during his PhD studies. I am glad that my company TCDD (Turkish State Railways) for giving me opportunity to conduct doctoral studies while working in the company. I am also grateful to the members of the Laboratory for Thermal and Power Engineering for their helpful and friendly contributions during my research stay in Germany with DAAD scholarship.

TABLE OF CONTENTS

Page

Page

LIST OF TABLES

LIST OF FIGURES

Figure **Page**

Figure **Page**

LIST OF ABBREVIATIONS AND SYMBOLS

Abbreviations and symbols which are used in this thesis are elaborated down-below

Symbols	Meanings
A	Surface area, mm2
a_{dec}	Angular deceleration, rad/s2
C	Specific heat, J/ (kg K)
cR	Exponent of Reynolds number
D	Thickness, mm
E	Elasticity modulus, GPa
F	Braking force, N
h	Heat transfer coefficient, W/m2K
K	Coefficient of Nusselt number
k	Thermal conductivity, W/mK
m_{lump}	Parameter in the lumped analysis
Nu	Nusselt number
P	Pressure, Pa
Pr	Prandtl number
q	Heat flux, W/m2
r	Radial coordinate, m
Re	Reynolds number
R_w	Radius of the wheel, m
T	Temperature, °C
t	Time, s
V	Linear velocity, km/h
V_0	Initial linear velocity, km/h
z	Axial coordinate, m
α_T	Thermal expansion coefficient, 1/K
β (1…6)	Coefficients of polynomials
δ	Thickness of the boundary layer, m
ε	Perturbation parameter
η	Dynamic viscosity, Pa.s

Symbols	Meanings
θ	Tangential coordinate, rad
λ	Thermal diffusivity, m2/s
μ	Friction coefficient
ν	Kinematic viscosity, m2/s
ρ	Density, kg/m3
σ_T	Axial thermal stress, MPa
τ	Wall shear stress, MPa
υ	Poisson ratio
ϕ_P	Coverage angle of the pad, deg
ω	Rotational speed, rad/s
ω_0	Initial rotational speed, rad/s

Subscripts	Meanings
∞	Ambient air
d	Disk
fill	Filling time
i	Inner
m	Mean
n	Time counter
o	Outer
p	Pad
w	Wall
ω	Rotational

Abbreviations	Meanings
CFD	Computational fluid dynamics
RPM	Revolution per minute

1. INTRODUCTION

A moving railway vehicle has a kinetic energy due to its mass and speed. In addition, if it is on an inclined line, it has potential energy due to its mass and vertical distance to the ground plane. To slow down or stop the vehicle, the energy of the vehicle must be partially or completely dissipated. The main purpose of braking systems is to achieve this dissipation. In addition, the brake systems have two other task that first one is ensuring the constant speed of the rail vehicle on inclined tracks and the second one is that rail vehicle remains motionless (parked) when needed. In order to provide these tasks, this decelerating force can be applied through different systems. These systems are mainly given in the following:

- Friction brake,
- Dynamic braking (switching the traction engine to the generator mode) and
- Friction-independent braking (based on electromagnetics and often used in emergency situations)

These systems can be found together on a train set and can work as complementary elements under different conditions. The common restrictive requirement for all systems is the adhesion between the wheel and the rail.

In braking designs, the most important factor in medium-speed transport, i.e., at speeds of approximately 160 km/h, is the adhesion between wheel and rail. For this reason, friction braking systems are the most widely used braking systems in passenger and freight in medium speed transportation. Since the amount of energy that needs to be converted at higher speeds is very high (at the level of 3-11 MJ in passenger trains with a speed of 100-160 km/h), additional braking systems are activated. Friction systems convert the vehicle's kinetic energy (potential energy if any) into heat energy through friction.

Two types of friction braking systems are available. The first is the shoe-brake system that is in direct contact with the wheel, and the second is the disk-brake system. Shoe-brake system is mostly used in freight trains. The friction braking system, which is widely used in vehicles for passenger transportation, is the disk brake system. The system consists mainly of the disk, pad and caliper component, Figure 1.1. The caliper component works in connection with the pneumatic pressure system of the train, and they perform the contact of the pad and the disk by applying pressure to the pads. Thus, the vehicle begins to decelerate.

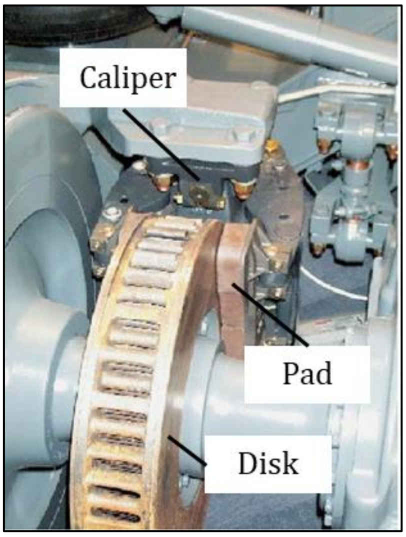

Figure 1.1. Schematic representation of the axle-mounted brake system [1]

A modern brake disk system usually has cooling fins in the disk component and the thermal behavior of the system varies with the number fins and their geometries. The disk system does not create thermal stresses in the wheels as in the shoe-brake system when a large amount of energy conversion is required. Thermal gradients resulting from the contact between disk and pad produce thermal gradients, which in turn cause thermal strains and cracks/hot spots in the disk. Example of thermal cracks in a railway brake disk are shown in Figure 1.2. If the magnitude of wear and faults exceed certain values, the braking system may become inefficient [2]. Laboratory tests of train (TGV) disks used in operation in France have also shown that thermal interaction leads to different types of faults [3]. Wear is not always a safety hazard but can lead to significant cost increase when they occur with a high frequency. In recent years, with the increase of sensitivities regarding the environment and public health, the particles emitted by the wearing of the disk-pad system have started to cause more awareness about the problem and academic research has been initiated for the investigation on the issue [4,5].

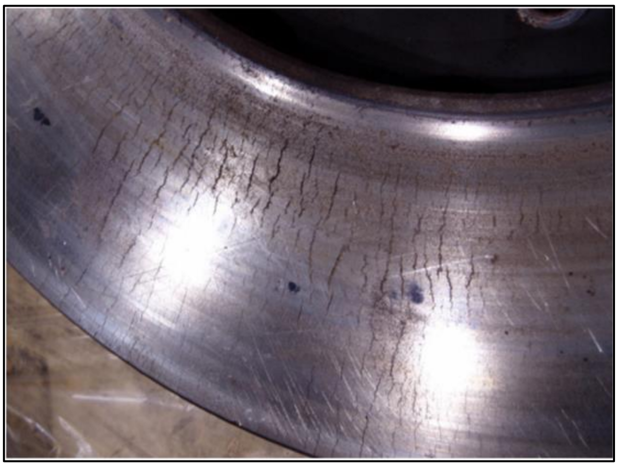

Figure 1.2. Thermal cracks in a railway brake disk [6]

In addition, if the disk becomes thermally unstable because of an overheating during a braking process, the coefficient of friction between the disk and the pad is significantly reduced (brake fading), see Figure 1.3. and the braking distance is extended. Aforementioned situations have a negative impact on rail transportation, both in terms of LCC and safety. Due to the fact that there is some freedom in the selection of disk and pad materials and that it is possible to change their geometric designs, there are a number of areas of improvement in the disk system through the engineering science approach.

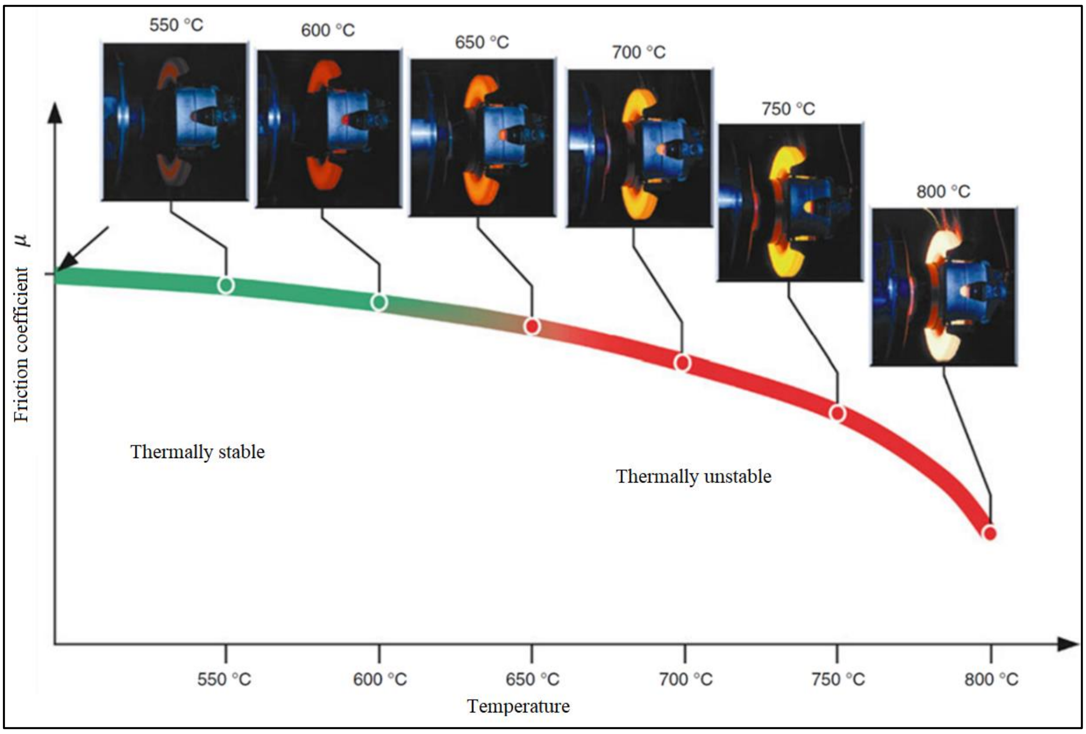

Figure 1.3. Friction coefficient behavior during testing [7]

Analysis methods and solutions have been developed through different scientific approaches against problems such as disk-pad wear caused by thermal interaction and driving safety [6,8]. Some of the given references also include the disk system in automobiles because there is a similar thermal interaction between the disk and the pad. In many related research studies, analysis and experimental studies have been carried out mainly from the point of view of the sciences of heat transfer, fluid mechanics and solid mechanics. In these studies, they have generally focused individually on convective cooling of the disk or the analysis of temperature distribution and thermal stresses on the solid disk.

The fields of heat transfer and fluid mechanics are sub-branches of applied engineering sciences. And the following scientific methods within the context of applied engineering are used to analyze problems and generate new knowledge on the subject:

- Experimental,
- Theoretical (with analytical methods) and
- Computational (with numerical methods)

Many studies involve a combination of these because the validation of the theory/computational model must be done experimentally. In some cases, numerical calculations are performed in the studies that mainly utilizes a theoretical method [9]. The advantages and disadvantages of the methods are mainly shown in Table 1.1. The method where computational methods are used in the fields of heat transfer and fluid mechanics is called Computational Fluid Dynamics (CFD).

Table 1.1. Comparison of methods in heat transfer and fluid mechanics [9]

Method	Advantages	Disadvantages
Experimental	Closest to the realistic results	Equipment requirement Scaling problem Measurement challenges Costs
Theoretical	Formulates general information.	1. It can be applied to problems with simple geometry and physics. 2. It is usually applied to linear problems.
Computational	1. There is no requirement to be linear. 2. Complex physics can be addressed.	1. Discretization errors 2. The problem of defining boundary conditions 3. Computational costs

In the future, the integration of CFD, theory, advanced manufacturing techniques (e.g., 3D printing) and experimentation will lead to more economical and faster development of prototypes and systems that will be ready for market use [10]. This technological quartet and its interactions are conceptually shown in Figure 1.4. The steps in a modern research & development process can be considered as:

- first it will be guided by theory,
- CFD will be used to predict the behavior of the system,
- advanced manufacturing techniques will be used to manufacture prototypes, and
- experiments will also confirm their design performance.

The process will then be repeated until a design meets the desired design performance metrics (e.g. low flow resistance, higher thermal efficiency, etc.). This point of view is a modern and reasonable approach. In a sense, the study involving a brake system under the consideration includes the analysis of the problem resulting from the existing designs and the goal of producing possible solutions to them. In the light of these reasoning and information given above, the CFD (enhanced with experimental data) approach is adopted in this thesis.

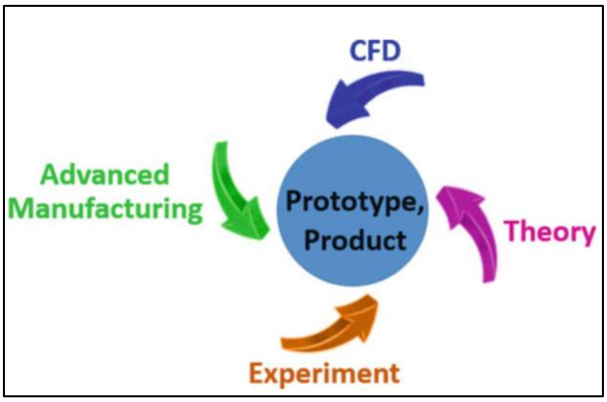

Figure 1.4. Modern R&D process and its subcomponents [10]

When the studies of recent years are examined, it is observed that the heat transfer, flow field and fluid-solid interaction are discussed and the regarding problems are investigated to find optimum designs. In the case of railway systems, there are experimental-computational studies aimed at the analysis and optimization of convective heat transfer over disk [11,12]. It was also mentioned that there are studies involving the analysis of heat dissipation and thermal stresses on the disk [13] . In parallel with the increasing computational capacities of computers, some recent studies have turned to the solid fluid coupled heat transfer (conjugate heat transfer) [14] . During braking of a car or train, the flow speed on the disk surfaces changes as the vehicle slows down. This change affects the convective heat transfer coefficients at each point on the disk surface, subsequently thermal behavior of the disk and its temperature distributions. Convective heat transfer coefficients change at each point on the disk surface and at different times. Therefore, it is not realistic to analyze the thermal behavior of the disk with a constant convective heat transfer coefficients especially for the case of low deceleration rates.

Another problematic case is the drag braking which is applied to have a constant velocity during a downhill travel on the railway track. Convective heat transfer then occurs at a constant rotational speed and that case poses a great challenge for a disk pad system. There are standard-normative tests for railway disk-pad system in the laboratory environment to simulate the drag braking case under challenging conditions. Again, the prediction of a new design or various boundary conditions on an existing design is quite beneficial in terms of LCC (Life Cycle Costs). At this point the determination of the heat transfer coefficients on friction and ribbed surface of the disk is crucial to conduct accurate thermal calculations.

Therefore, a comprehensive analysis and approach using the convective heat transfer phenomena can be adopted at this point to achieve a reliable and cost-effective system. Convective flow over a rotating disk which can be seen as a simplified version of brake disk has been a subject a wide range of research studies [15–19]. The subject has also been an active research & development area in turbomachinery and other related areas. Convective heat transfer on a rotating disk has been investigated by several authors for a long time with different crossflow combinations such as free, axial flow and parallel flow on a rotating disk. The initial investigation point for a brake disk is the configuration of the free rotating disk or in some literature "rotating disk in still (stagnant) air" [20]. The free rotating disk has a three-dimensional boundary layer. At high rotational Reynolds number Re_{ω}, three flow regimes (laminar, transition and turbulent) may coexist on the rotating disk in radial direction. Boundary layer formation schematically is shown in Figure 1.5 for an easy visualization on a free rotating disk. The center of disk has thin and constant thickness laminar boundary layer and at some point, the instability starts (the onset of instability) and transition region begins with an increasing thickness of boundary layer, then, turbulent region at the third sector. In the figure, spiral vortices are shown as spline curves that are signature of onset on instability at the end of laminar region. All three regions have different convective heat transfer rates which must be determined through rigorous experiments. Precise determination of onset of instability for different fluids is still a significant subject in current research scene both theoretically and experimentally [21–23]. Particularly the effect of different heating rates on the stability are at the focus of some recent studies. Therefore, the convective experimental studies are conducted for the thesis study as an enhancement on the brake disk subject. Aims of the experiment were precise measurement of the Nusselt number on a free rotating disk with different heating rates for fluid air with the Infrared Thermography.

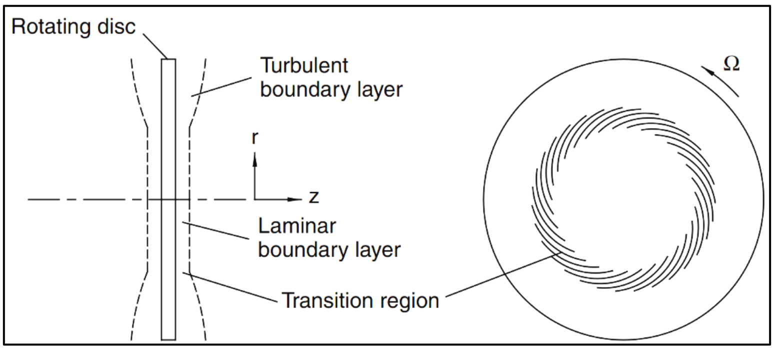

Figure 1.5. Schematic representation of the boundary layers on a disk [24]

An accurate and fast numerical model with realistic boundary conditions is essential for investigating thermal and thermal stress distributions of disk since there could be many scenarios and/or design configurations to consider in R&D processes. The main aim of the first part of the thesis to build a fast, robust, and accurate three-dimensional transient numerical thermal model which can incorporate the constant or time-dependent convective heat transfer correlations and the heat flux boundary condition primarily derived for the rotating brake disk without a parallel flow. This modeling will also be useful in the case of railway disks in the brake test rig for performance evaluations and certification processes. Regarding that, the convective experimental correlations from literature are used in the developed thermal model. The developed thermal model with constant convection coefficients is compared for the validation with the results of the numerical-experimental study by Grzes et al [25] considering the case of initial speed 110.1 km/h until the stop in the test-rig. Apart from that, two models;

1. Variable convection and variable thermal properties
2. Variable convection and constant thermal properties

were built to investigate the effect of variable thermal properties on the thermal behavior and stress distribution of railway disk using the commercial software Simcenter STAR-CCM+ software for initial speed of 120 km/h. The same geometry, material parameters, and mesh structure are used in Simcenter STAR-CCM+. It was also possible to compare results and the computational times of the developed model with the Simcenter STAR-CCM+, which represents a widely accepted software for three-dimensional CFD/heat transfer analyses in the industry [26]. Then, a comparison between constant and variable convection cases on the friction plate of the disk for the initial speed of 120 km/h was made using the developed model. The calculation of thermal stress distributions for several time instants has been done and presented using the temperature distributions data of the developed model and Simcenter STAR-CCM+ models. Regarding the thermal stress analysis, results of some test cases are shown namely the effects of the various initial velocities and various friction coefficients on the thermal stress distribution of the disk. Main findings from the developed thermal model and methodology adopted for the investigation of thermal stresses on the brake disk suggest that the model yields fast and accurate results for such engineering analysis in the area. Apart from that, significant indications on the effect of variable thermal properties of the disk and convection correlations are obtained.

CFD models as mentioned are quite valuable in design processes. Regarding this view, it is considered that the use of conjugate heat transfer method for a better understanding of the convective heat transfer coefficients will be beneficial to develop a design framework for the railway brake disks. Therefore, second part focuses on developing a novel conjugate heat transfer model (the CFD model) of a brake disk with cooling ribs. This part of study is mainly aimed for the determination of the Nusselt numbers in drag braking case with longer durations. So that these Nusselt number correlations from friction plate and ribbed surface can be used in thermal calculations and thermal models.

To achieve a reliable CFD model, a novel convective experimental approach on a simplified heated rotating disk developed and experiments are performed on an experimental setup. The investigations included the effect of the heating on the onset of instability of the flow over a rotating disk, so that more precise Nusselt correlations can be obtained. To have a non-invasive measurement system, the experimental setup does not include thermocouples and HWA (Hot-Wire Anemometry). Transient temperature data with the help of an in-house developed Python code is performed to reconstruct the precise transient temperature distributions over the radius of the disk. The directly measured transient temperature distributions are used for calculation of the Nusselt number distributions for a range of rotational speeds and heating rates. Then, they are compared with the previous literature data. The results are presented in a way so that the effect of heat transfer strength on the onset of instability on the rotating disk for several rotational speeds are tractable. This experimental setup is adopted in developing CFD model of the heated rotating disk in Simcenter Star-CCM+. The boundary conditions in experiments are also implemented in the model. In the end, convection over a rotating disk coupled with conduction of the disk (conjugate heat transfer) is modelled. The model includes a transitional flow modelling through the Gamma-transition model [27] that is developed to be used in conjunction with K-Omega SST turbulence model [28]. For flow-related quantities, a comparison is made with previously published experimental data. Additionally, the resulting thermal parameters are validated against the experimental setup that forms the basis of CFD model and with an analytical solution developed for the laminar thermal boundary layer calculations.

Using the methodology of that CFD model, a model of brake disk with cooling ribs is developed and simulated. However, simulations are only performed for a low rotational speed because of time limitations. Results of CFD model of the brake disk seem to be accurate for free rotating brake disk case. Correlations from that model can be used in thermal calculation models or the developed thermal model in Python in this thesis for further analysis and optimization studies.

2. LITERATURE SEARCH

In the studies of the railway vehicle disk system, convective cooling, conductive heat transfer on the disk and thermo-mechanical behavior of the disk are generally emphasized. Conjugate heat transfer, which includes disk and air flow, has been investigated for automobile and rail vehicle braking systems only in recent years. Apart from the brake disk studies, studies on convection heat transfer over a rotating disk will be summarized as these are part of the experimental study and the related CFD modeling in this thesis study.

2.1. Previous Studies on the Brake Disk

There are several studies on disk brake systems with the focus on conducting analyses for temperature distributions and thermal stresses via experimental [25,29], numerical [7], and analytical methods [31]. In a study using the analytical method, the integral transform technique is applied for transient thermal analysis of motorbike brake disks. In that study, the temperature field as a function of radius and time is derived for the thin disk subject to non-symmetrical rotating heat flux capable of fast and efficient calculation of the temperature distributions [31]. However, this assumption does not hold for the thick railway brake disks with a high axial thermal gradient under hard braking conditions. Apart from that, the integral transform technique is quite cumbersome to be used for three-dimensional railway brake disks with complex space-time-dependent boundary conditions.

Apart from performance evaluations, there is also concern about fatigue life prediction of thermally loaded brake disks in automobiles and regional trains [32,33]. Among others, any regional train usually must brake more often, and therefore fatigue issues are considered highly important for that application cases. Fatigue life predictions for a gray cast iron disk of a regional train are investigated in a study [33] using the temperature history of the disk, S–N data of the material, and modified Miner's rule. The study concluded that temperature history and thermal stresses obtained from temperature history using modified Miner's rule give sufficient insights about fatigue life of the disk when the study results were compared with the corresponding experimental data.

One significant study [25] was performed on railway brake disks with the assumption of a constant heat transfer coefficient (HTC) and thermal properties, including the numerical model development and experimental method [25]. The purpose of the study was to build a numerical model using commercial finite element modeling software. The temperature fields of the model are comparable to the results of test-rig experiments. Comparison of temperature distributions between numerical and experimental studies showed good agreement in the study. Also, the developed model in the present article is compared with the results of this study [25] for validation purposes.

In an early and significant experimental study on automobile disks (grey cast iron), it was found that the convection and variable thermal properties are important factors for the analysis of thermal stresses and surface cracks under hard braking conditions [34]. Thermal stress distribution due to non-linear temperature distribution is calculated with an equation derived from the stress analysis presented in [35] with the assumption that the disk is restrained under the pad area where the disk also experiences the highest increase during the braking.

The focus in a study is to estimate the impact of various design parameters of the brake disk on the thermal performance of the brake disk and optimize it for a given heat loss rate. CFD simulations were [36] used to validate the experimental formulas of Limpert's convective heat transfer coefficients [37].

In these modeling/simulation-based studies, the focus is usually on calculating convection heat transfer coefficients from the perspective of CFD or on conduction modeling in disk/pad. A review article [38] on the cooling in automobile brake systems states that when the two situations are examined together, in other words, solid and fluid solvers should be coupled and flow-temperature field changes should be taken into consideration, and therefore these studies are found to be of high difficulty.

Some recent studies have focused on coupled (conjugate) simulation of brake disk [39,40] for the drag braking case. These studies used weak coupling methods that is thermal field of the disk is solved in a FEM solver and resulting temperature data are then used as boundary condition in CFD solver which is requires some coupling algorithms. Strong coupling method at this point is considered to be more practical and realistic

2.2. Previous Studies on the Convection over Rotating Disk

Convective flow on a rotating disk has been the subject of a wide variety of research studies [15–19]. The subject has also been an active R&D area in turbomachinery and brake disk and other related areas. Convective heat transfer on a rotating disk has been investigated by several authors for a long time with different crossflow combinations such as axial flow and parallel flow on a rotating disk. Convective heat transfer studies were mainly aimed for the determination of local or average Nusselt number dependence on rotational Reynolds ($Re_{\omega} = \omega r^2 / \nu$) and Prandtl numbers for different fluids [22,41,42]. It is important to emphasize that De Vere's doctoral dissertation [20] contains a comprehensive and relevant work on free rotating disk and parallel flow configurations. His research yielded accurate determination of heat transfer coefficients/Nusselt numbers with and main parameters of the hydrodynamic boundary layer for various flow configurations and rotating speeds. Even though the experimental equipment was not well-sophisticated in his time he managed long ago to have accurate and precise results that were relatively in good agreement both with theoretical studies (before him) and experimental studies (after him).

The transition of boundary layer on a rotating disk in a still (stagnant) fluid has also attracted considerable attention [43,44], since some practical systems can be idealized using the physical interaction over the rotating disk and the transitional flow is one of the typical phenomena in a three-dimensional boundary layer accompanied by a secondary flow, which is complex in principle [45]. In those studies, one of the objectives was the determination of the critical Reynolds number $Re_{\omega,cr}$; the point at which a given infinitesimal perturbation is amplified and thus the laminar flow becomes destabilized.

The heat transfer is reported to have a significant influence in the stability investigations as early as in 1960 by Schlichting [46]. Temperature dependent properties of a fluid poses a challenge for a precise stability analysis. Therefore, a physical concept named perturbation parameter is invented for this kind of analysis.

$$\varepsilon = \frac{T_w - T_\infty}{T_\infty} \tag{2.1}$$

The perturbation parameter given in equation (2.1) with the Kelvin unit is an essential and carefully reasoned concept in the early investigations [47,48] on the convective flat plate flow. It defines the strength of the heat transfer. The critical Reynolds number dependence on the perturbation parameter is given in [49] for a flat plate flow as

$$\mathrm{Re}_{cr} = \mathrm{Re}_0\left(1+\varepsilon\left(A_\rho B_\rho + A_\mu B_\mu\right)+O\left(\varepsilon^2\right)\right) \tag{2.2}$$

This general expression is valid for every Newtonian fluid and with small perturbation parameter. The thermophysical coefficients in equation (2.2)

$$A_\rho = \frac{T}{\rho}\frac{\partial \rho}{\partial T}\bigg|_0 \quad \text{and} \quad A_\mu = \frac{T}{\mu}\frac{\partial \mu}{\partial T}\bigg|_0 \tag{2.3}$$

And the coefficients B_ρ and B_μ depend on both Prandtl number and mean flow. Equation (2.2) represents the change of the critical Reynolds number Re_{cr} for sufficiently normalized wall temperature differences for both two-dimensional and three-dimensional boundary layers [21]. It is also important to mention that the air shows a destabilized convective behavior with the temperature increase which also means a higher perturbation parameter ε. On the other hand, the water shows a stabilized behavior with a higher perturbation parameter.

Although, it has been known for a long time that the heating can considerably influence the stability of laminar boundary layer flows [46,50], only a few recent studies have focused on this issue for the rotating disk case. A linear stability analysis of the flow over a rotating disk is conducted considering the temperature-dependent thermophysical properties of a fluids in a study [23]. Recent experimental studies [21,22] on the subject have focused on Prandtl number effect combined with different wall temperature effects on water over a rotating disk. However, the air as a fluid in these experimental studies has not been investigated since an experimental study with such a fluid arises some challenges due to its rather low rate of change of thermophysical parameters with respect to the temperature than the liquids like water.

Another issue regarding the experiments with the air is the effect from the vibrations of the rotating equipment since the air is very sensitive to these vibrations so that in some cases dominate the behavior of the boundary layer. The problem was reported in several instability studies on rotating disk flow in still air [43,44]. It has been stated in a previous study [44] that the data from Hot-Wire Anemometry (HWA) device has an artificial noise arising from the vibration of the experimental setup and in turn these considerably affect the investigation particularly the onset of instability. This was also an observed fact in the initial phase of the current study. The measurements with HWA that is less than 1 mm close to the rotating disk surface had a highly noisy data especially around the frequencies under the investigation.

Experimental convective heat transfer research with air has been also conducted with infrared thermal cameras in several studies [41,51–53]. As known to the authors, first study with IR camera on rotating is done by Cardone et. al [51] and they have conducted experiments on a heated disk with (only one wall temperature) constant wall heat flux. It has been demonstrated that using an IR camera for such a study is advantageous, as their Nusselt number correlations agreed well with previous theoretical studies. Later, same authors investigated the existence of spiral vortices with IR camera [54] and they visualized the spiral vortices in transitional regime on a heated rotating disk. With their approach, they were unable to explain the effect of heating on rotating disk. This is because that only with one wall temperature is considered and their statement was “the stability characteristics may, therefore, change significantly” with the heating.

In other related studies, [52,53], main objective was the heat transfer in a rotor (rotating disk)-stator system with an air gap in between. However, in those experiments they also measured the case of rotating free disk in still air, and they applied a novel method for determination of the Nusselt numbers. In this novel method, they first calculated the local heat flux heat transfer from the known transient temperature obtained by IR camera and interface temperatures measured by thermocouples. After calculating the local heat flux, they obtained the local heat transfer coefficients and hence Nusselt numbers. In another study with IR camera on a rotating disk in still air has been conducted for only laminar flow with low rotational speed [41]. Their experimental correlation was in good agreement with laminar correlations developed earlier.

3. THEORETICAL BACKGROUND

3.1. Conservation Equations

Conservation equations are mathematical expressions derived from the fundamental laws of physics. In this section, equations will be presented, starting from three physical principles:

1. Conservation of mass
2. Newton's second law (conservation of momentum)
3. Conservation of energy

In fluid mechanics, analyses are performed after a certain CV (Control Volume) is determined. The change of physical properties with time within the control volume can be analyzed by applying the Reynolds transport theorem. In summary, the Reynolds transport theorem describes the relationship between the quantities of properties entering and leaving the control volume and their variation in the volume with time. Therefore, derivations are based Reynolds transport theorem.

3.1.1. Conservation of mass (Continuity equation)

The equation of conservation of mass can be obtained by considering a cube element perpendicular to the coordinate system components with the mass input and output in three dimensions. The components of the velocity vector in the x, *y* and *z* directions will be taken as *u*, *v* and w.

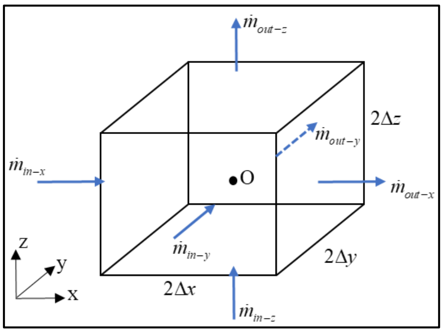

Figure 3.1. Mass inflow and outflow on a differential CV

If the Taylor series expansion is used for the change of mass with respect to the center of the cube volume, the definitions of the quantities of mass entering and leaving the control volume can be obtained. These quantities are given in Table 3.1.

Table 3.1. Definitions of inlet and outlet mass flow rates for a CV

Axis	Inlet mass flow rate $\dot{m}_{in}$	Outlet mass flow rate $\dot{m}_{out}$
x	$\left(\rho u-\frac{\partial(\rho u)}{\partial x}\Delta x\right)2\Delta y2\Delta z$	$\left(\rho u+\frac{\partial(\rho u)}{\partial x}\Delta x\right)2\Delta y2\Delta z$
y	$\left(\rho v-\frac{\partial(\rho v)}{\partial y}\Delta y\right)2\Delta x2\Delta z$	$\left(\rho v+\frac{\partial(\rho v)}{\partial y}\Delta y\right)2\Delta x2\Delta z$
z	$\left(\rho w-\frac{\partial(\rho w)}{\partial z}\Delta z\right)2\Delta x2\Delta y$	$\left(\rho w+\frac{\partial(\rho w)}{\partial z}\Delta z\right)2\Delta x2\Delta y$

Since the selected cube element is taken so that it is too small, the volume integral of time derivative of mass can be expressed as a differential. Then, the relationship between inlet and outlet mass flow rates together with the time change can be written according to the Reynolds transport theorem as in the following

$$\frac{\partial\rho}{\partial t}2\Delta x2\Delta y2\Delta z=-\frac{\partial(\rho u)}{\partial x}2\Delta x2\Delta y2\Delta z-\frac{\partial(\rho v)}{\partial y}2\Delta x2\Delta y2\Delta z-\frac{\partial(\rho w)}{\partial z}2\Delta x2\Delta y2\Delta z \tag{3.1}$$

After arrangements in equation (3.1), the conservation of mass for compressible flow becomes (also presented in vectorial form)

$$\begin{gathered}\frac{\partial\rho}{\partial t}+\frac{\partial(\rho u)}{\partial x}+\frac{\partial(\rho v)}{\partial y}+\frac{\partial(\rho w)}{\partial z}=0\\ \frac{\partial\rho}{\partial t}+\nabla\cdot(\rho\vec{V})=0\end{gathered} \tag{3.2}$$

The density for incompressible flow does not vary by time or location. The mass conservation for incompressible flow in this case is:

$$\vec{\nabla}\cdot(\vec{V}) = \frac{\partial u}{\partial x} + \frac{\partial v}{\partial y} + \frac{\partial w}{\partial z} = 0 \qquad (3.3)$$

3.1.2. Conservation of momentum

We can write the Reynolds Transport equation for the magnitude of momentum in a control volume as follows:

$$\frac{d}{dt}(m\vec{v}) = \sum \vec{F} = \frac{\partial}{\partial t}\int_{CV}(\rho\vec{v})dV + \int_{CS}(\rho\vec{v})\vec{v}\cdot\vec{n}dA \qquad (3.4)$$

Using the divergence theorem, it follows (3.4)

$$\frac{d}{dt}(m\vec{v}) = \sum \vec{F} = \int_{CV}\frac{\partial}{\partial t}(\rho\vec{v})dV + \int_{CV}\nabla\cdot(\rho\vec{v}\vec{v})dV \qquad (3.5)$$

Equation is (3.5) used to obtain the balance of forces in the x-direction:

$$\sum F_x = \sum F_{x,body} + \sum F_{x,surface} = \int_{CV}\frac{\partial}{\partial t}(\rho u)dV + \sum_{out}\dot{m}u - \sum_{in}\dot{m}u \qquad (3.6)$$

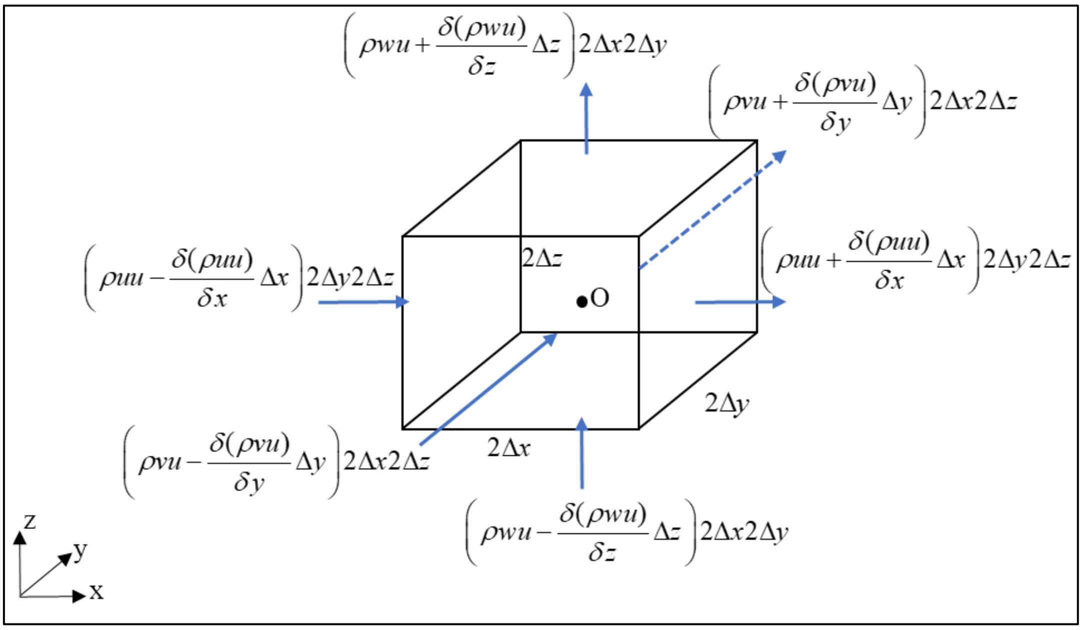

Figure 3.2. Momentum fluxes in a differential CV

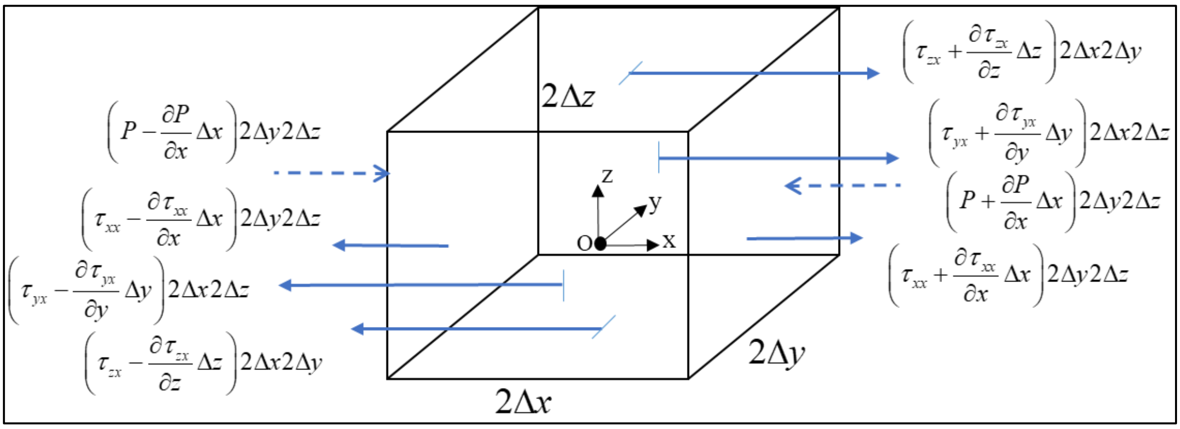

Figure 3.3. Surface forces acting on the differential CV in the x-direction

Substituting all momentum fluxes and surface forces as well as body forces into equation (3.6) yields the most general expression for conservation of momentum in three directions.

$$
\begin{aligned}
&\frac{\partial}{\partial t}(\rho u)+\frac{\partial}{\partial x}(\rho uu)+\frac{\partial}{\partial y}(\rho vu)+\frac{\partial}{\partial z}(\rho wu)=\rho g_x-\frac{\partial P}{\partial x}+\frac{\partial \tau_{xx}}{\partial x}+\frac{\partial \tau_{yx}}{\partial y}+\frac{\partial \tau_{zx}}{\partial z}\\
&\frac{\partial}{\partial t}(\rho v)+\frac{\partial}{\partial x}(\rho uv)+\frac{\partial}{\partial y}(\rho vv)+\frac{\partial}{\partial z}(\rho wv)=\rho g_y-\frac{\partial P}{\partial y}+\frac{\partial \tau_{xy}}{\partial x}+\frac{\partial \tau_{yy}}{\partial y}+\frac{\partial \tau_{zy}}{\partial z}\\
&\frac{\partial}{\partial t}(\rho w)+\frac{\partial}{\partial x}(\rho uw)+\frac{\partial}{\partial y}(\rho vw)+\frac{\partial}{\partial z}(\rho ww)=\rho g_z-\frac{\partial P}{\partial z}+\frac{\partial \tau_{xz}}{\partial x}+\frac{\partial \tau_{yz}}{\partial y}+\frac{\partial \tau_{zz}}{\partial z}
\end{aligned}
\tag{3.7}
$$

If the exact derivative expression is used, the equation (3.7) is:

$$
\begin{aligned}
&\rho\frac{Du}{Dt}=\rho g_x-\frac{\partial P}{\partial x}+\frac{\partial \tau_{xx}}{\partial x}+\frac{\partial \tau_{yx}}{\partial y}+\frac{\partial \tau_{zx}}{\partial z}\\
&\rho\frac{Dv}{Dt}=\rho g_y-\frac{\partial P}{\partial y}+\frac{\partial \tau_{xy}}{\partial x}+\frac{\partial \tau_{yy}}{\partial y}+\frac{\partial \tau_{zy}}{\partial z}\\
&\rho\frac{Dw}{Dt}=\rho g_z-\frac{\partial P}{\partial z}+\frac{\partial \tau_{xz}}{\partial x}+\frac{\partial \tau_{yz}}{\partial y}+\frac{\partial \tau_{zz}}{\partial z}
\end{aligned}
\tag{3.8}
$$

<u>Navier–Stokes Equation</u>

The (3.8) momentum equations in Equation contain a total of 9 stress components, 6 of which are independent (due to symmetry). In this case, there are a total of 10 (3 velocity component + 1 pressure + 3 stress component) unknowns. We have a total of 4 equations, 1 equation is for the conservation of mass and other 3 equations are for the conservation of momentum. In this case, 6 additional equations are required to perform the analysis.

These equations are required for analysis constitutive equations. They allow us to write down the stress components in terms of velocity field and pressure field. For that reason, it is necessary to separate pressure and viscous stresses.

When the fluid is in motion, the pressure and viscous stresses coexist then the stress tensor becomes

$$\sigma_{ij} = \begin{bmatrix} \sigma_{xx} & \tau_{xy} & \tau_{xz} \\ \tau_{yx} & \sigma_{yy} & \tau_{yz} \\ \tau_{zx} & \tau_{zy} & \sigma_{zz} \end{bmatrix} = \begin{bmatrix} -P & 0 & 0 \\ 0 & -P & 0 \\ 0 & 0 & -P \end{bmatrix} + \begin{bmatrix} \tau_{xx} & \tau_{xy} & \tau_{xz} \\ \tau_{yx} & \tau_{yy} & \tau_{yz} \\ \tau_{zx} & \tau_{zy} & \tau_{zz} \end{bmatrix} \tag{3.9}$$

If the equation (3.9) is expressed according to tensor notation:

$$\sigma_{ij} = -P\delta_{ij} + \tau_{ij} \tag{3.10}$$

Here the tensor τ_{ij} is called the viscous tensor or the deviatoric stress tensor. We can define the constitutive equations, the i.e., tensor τ_{ij}, in terms of the velocity and pressure fields. The regarding assumptions are:

- Flow is incompressible
- Isothermal flow

Viscous tensor for an incompressible Newtonian fluid with constant properties $\tau_{ij} = 2\mu s_{ij}$, here s_{ij} is the deformation tensor (rate of strain or rate of deformation). In Cartesian coordinates, the viscous tensor consists of nine components, six of which are independent due to the symmetry:

$$\tau_{ij}=\begin{bmatrix}\tau_{xx} & \tau_{xy} & \tau_{xz}\\ \tau_{yx} & \tau_{yy} & \tau_{yz}\\ \tau_{zx} & \tau_{zy} & \tau_{zz}\end{bmatrix}=2\mu\begin{bmatrix}\frac{\partial u}{\partial x} & \frac{1}{2}\left(\frac{\partial u}{\partial y}+\frac{\partial v}{\partial x}\right) & \frac{1}{2}\left(\frac{\partial u}{\partial z}+\frac{\partial w}{\partial x}\right)\\ \frac{1}{2}\left(\frac{\partial v}{\partial x}+\frac{\partial u}{\partial y}\right) & \frac{\partial v}{\partial y} & \frac{1}{2}\left(\frac{\partial v}{\partial z}+\frac{\partial w}{\partial y}\right)\\ \frac{1}{2}\left(\frac{\partial w}{\partial x}+\frac{\partial u}{\partial z}\right) & \frac{1}{2}\left(\frac{\partial w}{\partial y}+\frac{\partial v}{\partial z}\right) & \frac{\partial w}{\partial z}\end{bmatrix}\tag{3.11}$$

On the right side of the equation, (3.11) the components of the viscous tensor are given as function of the deformation rate and viscosity of the fluid. The stress tensor then becomes

$$\sigma_{ij}=\begin{bmatrix}\sigma_{xx} & \tau_{xy} & \tau_{xz}\\ \tau_{yx} & \sigma_{yy} & \tau_{yz}\\ \tau_{zx} & \tau_{zy} & \sigma_{zz}\end{bmatrix}=\begin{bmatrix}-P & 0 & 0\\ 0 & -P & 0\\ 0 & 0 & -P\end{bmatrix}+\mu\begin{bmatrix}2\frac{\partial u}{\partial x} & \left(\frac{\partial u}{\partial y}+\frac{\partial v}{\partial x}\right) & \left(\frac{\partial u}{\partial z}+\frac{\partial w}{\partial x}\right)\\ \left(\frac{\partial v}{\partial x}+\frac{\partial u}{\partial y}\right) & 2\frac{\partial v}{\partial y} & \left(\frac{\partial v}{\partial z}+\frac{\partial w}{\partial y}\right)\\ \left(\frac{\partial w}{\partial x}+\frac{\partial u}{\partial z}\right) & \left(\frac{\partial w}{\partial y}+\frac{\partial v}{\partial z}\right) & 2\frac{\partial w}{\partial z}\end{bmatrix}\tag{3.12}$$

The momentum equations can be transformed into the Navier–Stokes equations:

$$\begin{aligned}\rho\left(\frac{\partial u}{\partial t}+u\frac{\partial u}{\partial x}+v\frac{\partial u}{\partial y}+w\frac{\partial u}{\partial z}\right)&=\rho g_x-\frac{\partial P}{\partial x}+\mu\left[\frac{\partial^2 u}{\partial x^2}+\frac{\partial^2 u}{\partial y^2}+\frac{\partial^2 u}{\partial z^2}\right]\\ \rho\left(\frac{\partial v}{\partial t}+u\frac{\partial v}{\partial x}+v\frac{\partial v}{\partial y}+w\frac{\partial v}{\partial z}\right)&=\rho g_y-\frac{\partial P}{\partial y}+\mu\left[\frac{\partial^2 v}{\partial x^2}+\frac{\partial^2 v}{\partial y^2}+\frac{\partial^2 v}{\partial z^2}\right]\\ \rho\left(\frac{\partial w}{\partial t}+u\frac{\partial w}{\partial x}+v\frac{\partial w}{\partial y}+w\frac{\partial w}{\partial z}\right)&=\rho g_z-\frac{\partial P}{\partial z}+\mu\left[\frac{\partial^2 w}{\partial x^2}+\frac{\partial^2 w}{\partial y^2}+\frac{\partial^2 w}{\partial z^2}\right]\end{aligned}\tag{3.13}$$

With another notation:

$$\begin{aligned}\rho\frac{Du}{Dt}&=\rho g_x-\frac{\partial P}{\partial x}+\mu\left[\frac{\partial^2 u}{\partial x^2}+\frac{\partial^2 u}{\partial y^2}+\frac{\partial^2 u}{\partial z^2}\right]\\ \rho\frac{Dv}{Dt}&=\rho g_y-\frac{\partial P}{\partial y}+\mu\left[\frac{\partial^2 v}{\partial x^2}+\frac{\partial^2 v}{\partial y^2}+\frac{\partial^2 v}{\partial z^2}\right]\\ \rho\frac{Dw}{Dt}&=\rho g_z-\frac{\partial P}{\partial z}+\mu\left[\frac{\partial^2 w}{\partial x^2}+\frac{\partial^2 w}{\partial y^2}+\frac{\partial^2 w}{\partial z^2}\right]\end{aligned}\tag{3.14}$$

3.1.3. Conservation of energy

The energy equation is based on the first law of thermodynamics. This law states that the difference of entering and leaving energies through the system will be equal to the change of the total energy of the system:

$$E_{in} - E_{out} = \Delta E_{total} \tag{3.15}$$

In the absence of electrical, magnetic, and surface tension effects (i.e., for simple compressible systems), the change in the total energy of a system during a process is the sum of changes in its internal, kinetic, and potential energies.

If the total amount of energy per unit mass (specific energy) is written:

$$\begin{aligned} E_{in} - E_{out} &= \left(Q_{in} - Q_{out}\right) + \left(W_{in} - W_{out}\right) = \Delta E_{total} \\ E_{in} - E_{out} &= \Delta Q + \Delta W = \Delta E_{total} \end{aligned} \tag{3.16}$$

Energy transfer to a system takes place in three ways, heat transfer, work transfer and mass flow. In the case that the mass does not change, the equation (3.15) can be expressed as follows:

$$\begin{aligned} E_{in} - E_{out} &= \left(Q_{in} - Q_{out}\right) + \left(W_{in} - W_{out}\right) = \Delta E_{total} \\ E_{in} - E_{out} &= \Delta Q + \Delta W = \Delta E_{total} \end{aligned} \tag{3.17}$$

Thu units of energy expressions in equation (3.17) are J (Joule). When these are written per unit mass

$$de_{total} = dq + d\varpi \tag{3.18}$$

The unit of (3.18) is J / kg. If the two sides of the equation are multiplied by the expression density, their unit become, J / m^3 and this equation expresses the energy as per unit volume. If we then express them in terms of their changes in unit time with material time derivative:

$$\rho\frac{De_{total}}{Dt}=\rho\frac{dq}{dt}+\rho\frac{d\varpi}{dt} \tag{3.19}$$

To derive the term $\rho dq/dt$ in this equation, it is necessary to express the equations of heat transfer over the surface area of the medium for a CV based on the definition of Fourier's law. According to Fourier's law, the amount of heat transfer per unit time is

$$\dot{Q}=-kA\frac{dT}{dn} \tag{3.20}$$

Here, $\dot{Q}$ is the amount of heat transfer per unit of time, k is coefficient of thermal conductivity, A is the surface area where heat transfer takes place, and the length of the surface is n on which the heat transfer occurs.

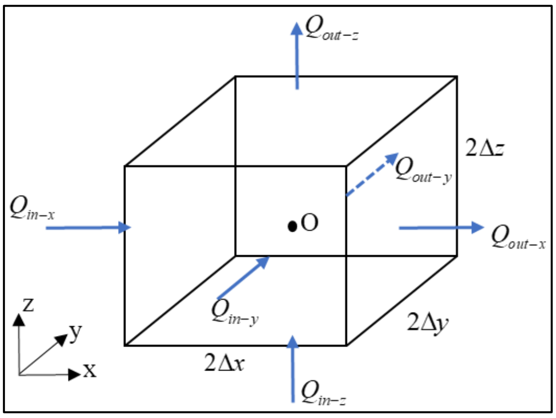

Figure 3.4. A CV with heat input and output

Using the Taylor series, the amount of heat energy entering and leaving in all directions are defined over time interval Δt is given in Table 3.2.

Table 3.2. Definitions of heat input and output in a differential volume

Axis	Heat input E_{in}	Heat output E_{out}
x	$-k\left(\frac{\partial T}{\partial x}-\frac{\partial^2 T}{\partial x^2}\Delta x\right)2\Delta y2\Delta z\Delta t$	$-k\left(\frac{\partial T}{\partial x}+\frac{\partial^2 T}{\partial x^2}\Delta x\right)2\Delta y2\Delta z\Delta t$
y	$-k\left(\frac{\partial T}{\partial y}-\frac{\partial^2 T}{\partial y^2}\Delta y\right)2\Delta x2\Delta z\Delta t$	$-k\left(\frac{\partial T}{\partial y}+\frac{\partial^2 T}{\partial y^2}\Delta y\right)2\Delta x2\Delta z\Delta t$
z	$-k\left(\frac{\partial T}{\partial z}-\frac{\partial^2 T}{\partial z^2}\Delta z\right)2\Delta x2\Delta y\Delta t$	$-k\left(\frac{\partial T}{\partial z}+\frac{\partial^2 T}{\partial z^2}\Delta z\right)2\Delta x2\Delta y\Delta t$

After arrangements the term $\rho dq/dt$ in (3.19) is obtained as in the following

$$\rho\frac{dq}{dt}=k\left(\frac{\partial^2 T}{\partial x^2}+\frac{\partial^2 T}{\partial y^2}+\frac{\partial^2 T}{\partial z^2}\right) \tag{3.21}$$

The work done on the differential CV is equal to the sum of the work done by the surface forces and the body forces.

$$W = W_{body} + W_{surface} \tag{3.22}$$

The surface forces and body forces in x-direction on the CV element are shown in Figure 3.5.

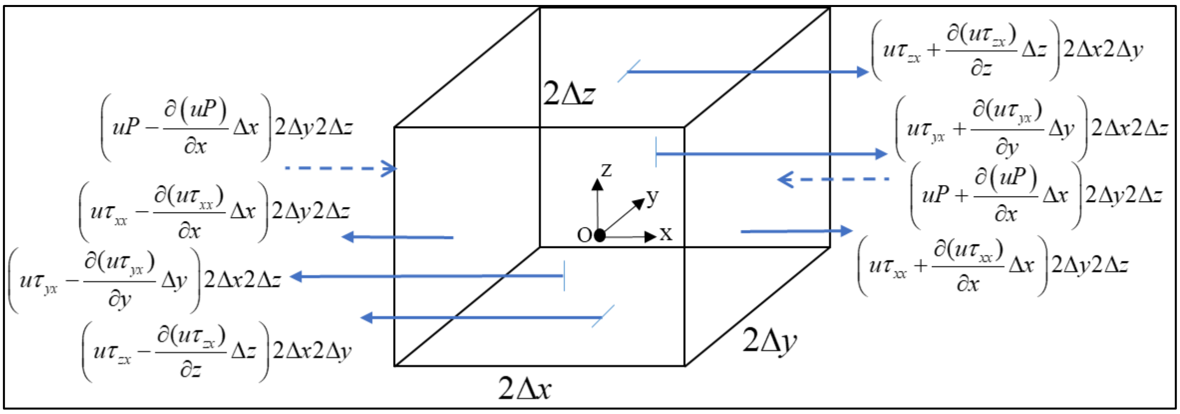

Figure 3.5. The surface forces and body forces in x-direction

When the surface and body forces are summed up and substituted in to equation (3.19), the energy equation becomes

$$\rho c\underbrace{\left(\frac{\partial T}{\partial t}+u\frac{\partial T}{\partial x}+v\frac{\partial T}{\partial y}+w\frac{\partial T}{\partial z}\right)}_{\frac{DT}{Dt}}=k\left[\frac{\partial^2 T}{\partial x^2}+\frac{\partial^2 T}{\partial y^2}+\frac{\partial^2 T}{\partial z^2}\right] \tag{3.23}$$

Since moving flows are analyzed in fluid mechanics, it is more useful to write the energy equation in terms of the enthalpy of the fluid. The total energy for deriving the enthalpy equation is h_{total} to be written in terms of the total enthalpy via Legendre transformation:

$$\begin{aligned} h_{total} &= \underbrace{i+\frac{P}{\rho}}_{h}+\frac{1}{2}(u^2+v^2+w^2)=e_{total}+\frac{P}{\rho} \\ e_{total} &= h_{total}-\frac{P}{\rho} \end{aligned} \tag{3.24}$$

Here, *h* presents the specific enthalpy for this section. The general enthalpy equation is then given as

$$\rho c_p\underbrace{\left(\frac{\partial T}{\partial t}+u\frac{\partial T}{\partial x}+v\frac{\partial T}{\partial y}+w\frac{\partial T}{\partial z}\right)}_{\frac{DT}{Dt}}=k\left[\frac{\partial^2 T}{\partial x^2}+\frac{\partial^2 T}{\partial y^2}+\frac{\partial^2 T}{\partial z^2}\right]+\frac{DP}{Dt} \tag{3.25}$$

3.2. Boundary Layer

In a flow field, a fairly thin region associated with high momentum and heat transfer rates is usually known as shear layer. The most common shear layer in heat transfer problems is the boundary layer, because that one of the main subjects in an engineering analysis is usually the heat transfer to or from a solid to a fluid [55].

If the flow occurs on a solid body or inside a body with a closed geometry, this flow can be analyzed using conservation equations obtained from the laws of physics. To do that, the boundary layer theory must first be taken into account. The boundary layer theory was developed in 1904 by the German engineer Ludwig Prandtl. In summary, the theory states that the flow field on a solid body consists of two region, in one region the viscous effects are important in a very small area in direct contact with the body, while in the other region it is possible to apply the potential flow approach (the assumption of non-viscous flow). A basic convective heat transfer problem will be presented through boundary layer approach in next section.

3.3. Fundamentals of the Convective Heat Transfer Problem

Convective heat transfer, by definition, refers to the situation where flow and heat transfer are combined. The problem of heat transfer from a solid plate to a fluid in the case of an external flow is shown schematically in Figure 3.6.

In this configuration, the solid plate having a higher temperature value then the fluid temperature. The plate is subjected to a uniform flow field and the formation of a hydrodynamic boundary layer on the left side and a thermal boundary layer on the right side is observed.

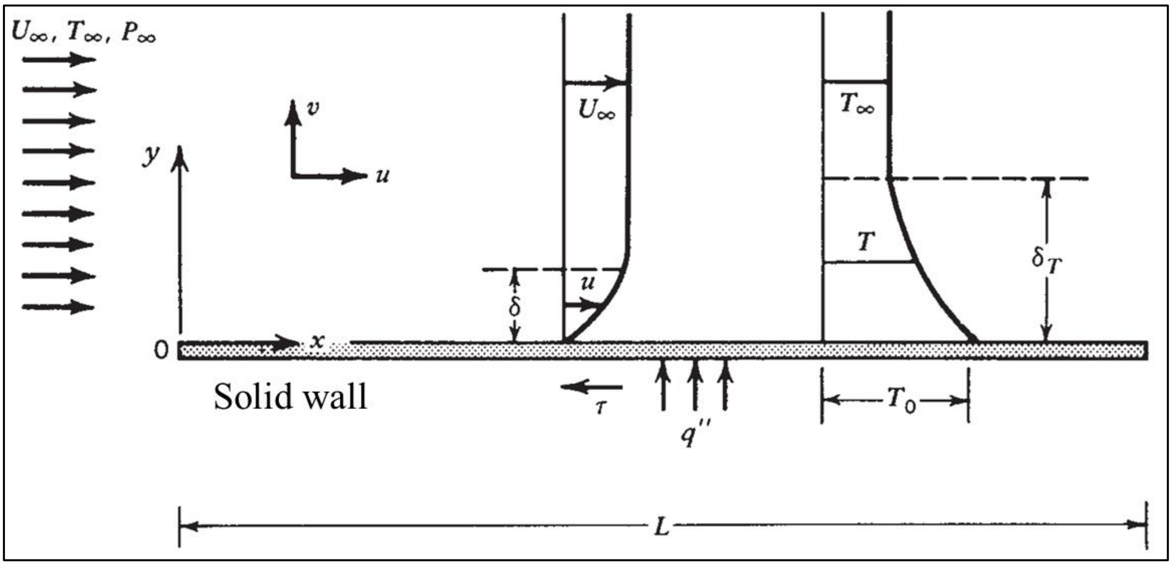

Figure 3.6. Formation of hydrodynamic and temperature boundary layers

By finding the net force exerted on the plate by the flow, we can obtain the friction (or drag) force. This value is also used to calculate magnitudes such as the pressure drop in the flow or the required pump force. The force exerted on the plate

$$F = \int_0^L \tau W dx \tag{3.26}$$

Heat transfer per unit time

$$q = \int_0^L q'' W dx \tag{3.27}$$

The shear stress at the wall (skin friction)

$$\tau = \mu \left(\frac{\partial u}{\partial y} \right)_{y=0} \tag{3.28}$$

And the wall heat flux:

$$q'' = h\left(T_0 - T_\infty\right) \tag{3.29}$$

Here h is the heat transfer coefficient. It is assumed that the non-slip hypothesis which is an empirically observed condition is valid. The non-slip condition implies that the transfer of heat to the fluid at the position $0<y<0^+$ occurs through a pure conduction

$$q'' = -k \left(\frac{\partial T}{\partial y} \right)_{y=0} \tag{3.30}$$

If the last two equations are used and the temperature distribution above the plate is known, the heat transfer coefficient is:

$$h = \frac{-k \left(\frac{\partial T}{\partial y} \right)_{y=0}}{T_0 - T_\infty} \tag{3.31}$$

For a two-dimensional problem, if conservation equations are written using incompressible flow assumption with constant properties, steady-state case, the equations read as

$$\frac{\partial u}{\partial x}+\frac{\partial v}{\partial y}=0 \tag{3.32}$$

$$u\frac{\partial u}{\partial x}+v\frac{\partial u}{\partial y}=-\frac{1}{\rho}\frac{\partial P}{\partial x}+\upsilon\left[\frac{\partial^2 u}{\partial x^2}+\frac{\partial^2 u}{\partial y^2}\right] \tag{3.33}$$

$$u\frac{\partial v}{\partial x}+v\frac{\partial v}{\partial y}=-\frac{1}{\rho}\frac{\partial P}{\partial y}+\upsilon\left[\frac{\partial^2 v}{\partial x^2}+\frac{\partial^2 v}{\partial y^2}\right] \tag{3.34}$$

$$u\frac{\partial T}{\partial x}+v\frac{\partial T}{\partial y}=\lambda\left[\frac{\partial^2 T}{\partial x^2}+\frac{\partial^2 T}{\partial y^2}\right] \tag{3.35}$$

where $\lambda = k/(\rho c)$ is the coefficient of thermal diffusivity. The equations contain four unknowns (u, v, P, T) and are subject to the following boundary conditions:

$$\left.\begin{array}{ll}\text{i) Non-slip} & u=0\\ \text{ii) Impermeable} & v=0\\ \text{iii) Wall temp.} & T=T_0\end{array}\right\}\text{ at the wall}$$

$$\left.\begin{array}{ll}\text{iv) Uniform flow} & u=U_\infty\\ \text{v) Uniform flow} & v=0\\ \text{vi) Uniform temp.} & T=T_\infty\end{array}\right\}\text{ perpendicular to the solid and infinitely far away} \tag{3.36}$$

Conservation equations and boundary conditions for a problem with a continuous regime apply for all points in the 2D flow field. A region close to the solid wall, where the speed reaches from $u = 0$ to $u = U_\infty$ and the temperature from $T = T_W$ to $T = T_\infty$ gives the essence of the boundary layer concept. In determining the size of this "close" zone, scale analysis can be used. In doing so, the free stream can be characterized by the following values

$$u=U_\infty,\quad v=0,\quad P=P_\infty,\quad T=T_\infty \tag{3.37}$$

Let the magnitude of the distance be δ through which u reaches from the point $u = 0$ on the wall to free stream value $u = U_\infty$. Then, a proper scaling of the parameters in a boundary layer yields

$$x \sim L, \quad y \sim \delta \text{ ve } u \sim U_\infty \tag{3.38}$$

The slenderness ($\delta \ll L$) of boundary layer is assumed, then the frictional force term $\partial^2 u / \partial x^2$ is negligible, and thus the x- momentum becomes

$$u\frac{\partial u}{\partial x} + v\frac{\partial u}{\partial y} = -\frac{1}{\rho}\frac{\partial P}{\partial x} + \nu\frac{\partial^2 u}{\partial y^2} \tag{3.39}$$

Again, using the slenderness of the boundary layer region assumption, the y-momentum becomes:

$$u\frac{\partial v}{\partial x} + v\frac{\partial v}{\partial y} = -\frac{1}{\rho}\frac{\partial P}{\partial y} + \nu\frac{\partial^2 v}{\partial y^2} \tag{3.40}$$

In general, pressure at any given point is the function of *x* and *y* and when it is expressed as the exact derivative, the differential pressure becomes

$$dP = \frac{\partial P}{\partial x}dx + \frac{\partial P}{\partial y}dy \tag{3.41}$$

If this expression is divided by *dx*:

$$\frac{dP}{dx} = \frac{\partial P}{\partial x} + \frac{\partial P}{\partial y}\frac{dy}{dx} \tag{3.42}$$

The pressure inside the boundary layer changes mainly in the x-direction; in other words, at any point *x*, the pressure inside the boundary layer is practically the same as the pressure immediately outside it:

$$\frac{\partial P}{\partial x} = \frac{dP_\infty}{dx} \tag{3.43}$$

Using the last equation, the x-momentum (3.39) becomes

$$u\frac{\partial u}{\partial x}+v\frac{\partial u}{\partial y}=-\frac{1}{\rho}\frac{dP_{\infty}}{dx}+\upsilon\frac{\partial^2 u}{\partial y^2} \tag{3.44}$$

That is the boundary layer equation for momentum, and keeping in mind how it is derived, it appears as an expression of the conservation of momentum in a unified way including both the *x* and *y* directions.

When we omit the term $\partial^2 T/\partial x^2$ thermal diffusion in equation (3.35) by analogy, the boundary layer equation for energy becomes

$$u\frac{\partial T}{\partial x}+v\frac{\partial T}{\partial y}=\alpha\frac{\partial^2 T}{\partial y^2} \tag{3.45}$$

The original problem in the beginning, with the application of boundary layer theory, is transformed into a problem with three equations and three unknowns *(u, v, T)* in the final state.

The thickness of the thermal boundary layer mainly depends on the Prandtl number. If the Prandtl number is in the order of 1 value, the values of the thermal and hydrodynamic boundary layer thicknesses are very close to each other. In the case of air, which is the fluid investigated in this thesis has the Prandtl number of 0.71 for a usual working condition in railway brake system.

3.4. Selection of Experimental Correlations

In many external flow problems, correlation functions are obtained by experimental method. These functions are constructed according to specific flow conditions and surface geometries. For the problem under consideration these steps can be followed,

1. Determination of the surface geometry,
2. Determination of the reference temperature value of the fluid,
3. Obtaining fluid properties for that temperature. (Film temperature or the property ratio method).

4. The Reynolds number must be calculated, and it must be determined whether the flow is laminar or turbulent.
5. It must be decided whether the use of the local or average heat transfer coefficient is appropriate.

After these stages are applied, appropriate experimental correlation selection can be done.

3.5. Turbulent Flow

In flows with low velocity and fluid having high viscosity, the streamlines are parallel to each other and transfer of momentum and energy between the streamlines occur only at the molecular level. This flow is called the laminar flow. In high velocity flow fields, the streamlines are distorted, and eddies are formed in the flow field. In this case, the transfer of physical properties takes place faster and the flow is called as the turbulent flow. The Reynolds number ($\mathrm{Re} = u\,L/\nu$) is used as a scale to determine the type of flow. In external flows, after the approximate Reynolds number 5×10^5, the flow becomes a turbulent flow. In Figure 3.7 the variables for the number Reynolds number are given and an internal flow as an example is shown. If the inertial force of the fluid is much greater than the viscous forces, instability begins in the flow and vortices form.

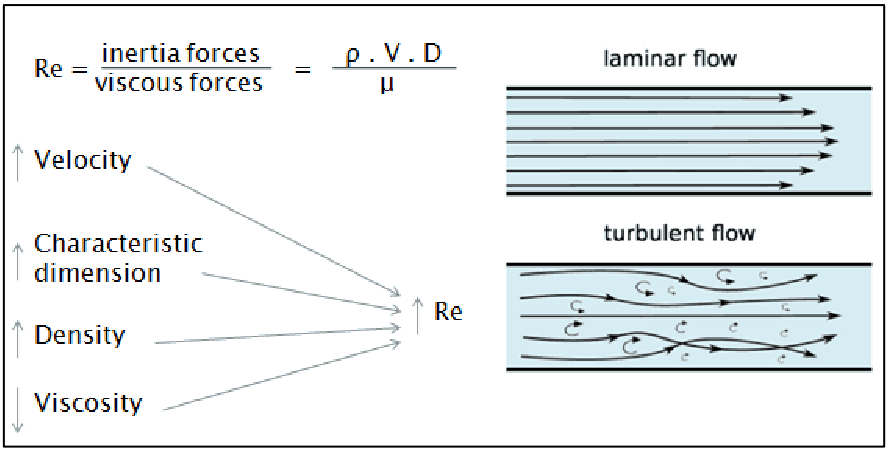

Figure 3.7. Parameters of Reynolds number

Turbulence is a flow of randomness and is extremely sensitive to changes in initial conditions. Boundary conditions and initial conditions play a decisive role in the change of parameters in turbulent flow. Very small differences in the initial conditions lead to the acquisition of different speed signals at a fixed location in turbulent region. Although careful testing is carried out, it is inevitable that each test will have different initial conditions. For this reason, statistical approaches have been developed for the analysis of turbulent flows.

Turbulence science is largely concerned with making statistical predictions about the solutions of nonlinear partial differential equations (Navier-Stokes Equations). Using statistical relations, the Reynolds averaged Navier-Stokes equation (RANS) has been derived. The derivation of these equations leads to an unknown term, the Reynolds stress tensor. At this point, new equations need to be derived to correspond to the unknowns and this is called the turbulence closure problem which will be explained in detail in the following sections.

It is difficult to talk about a phenomenon called the Turbulence Theory. Because there is no model of turbulence that can be universally adapted for all flow configurations. However, Kolmogorov's theory is able to explain the statistical properties of small-scale vortices in the flow for many conditions (jet flow, retardant trace, etc.) and boundary layer flows. Another example is the behavior of turbulent shear flow, which is very close to the solid wall, there are some statistical properties that are almost universal.

If the analysis of turbulent flow is to be performed, the solution of the Navier-Stokes momentum equations is required. In the end, the equation to be solved is a function of the flow speed *F(u)*, and the most compact form of this equation can be expressed as follows:

$$\frac{\partial u}{\partial t} = F(u) \tag{3.46}$$

This equation can be solved and obtained by direct numerical integral solution (DNS) method if we have boundary conditions and initial conditions. However, even for a simple geometry, this numerical solution is very time-consuming because of very small mesh size as a result of high Reynolds number. Engineering problems often involve geometries with complex structures. Solving overly complex systems by DNS is impossible with today's computers. Thus, the necessity of using statistical properties to solve the problem is realized again. Engineering research uses a combination of statistical methods, experiments and turbulence models.

3.5.1. Time-averaged equations of turbulent flow

It was mentioned that turbulence is a flow with highly random state. When the time-dependent average of this flow is examined by using statistical formulations, realistic analyzes can be made. The Figure 3.8 [56] shows the instantaneous formation of different vortices (eddy) of the turbulent flow zone around a sphere and the appearance of time-averaged vortices. Although this flow is turbulent, the time-averaged velocity field appears to be a smooth and regular function of the position. Reynolds-Averaged Navier-Stokes equations represent the actual flow in Figure 3.8 (a) as its time-averaged form in Figure 3.8 (b).

To obtain the RANS equations, the physical quantities are divided into their statistical components. As an example, if the velocity variable is divided into time-averaged $\overline{u}$ and the fluctuating variable $u'(t)$, the following expression is obtained.

$$u(t) = \overline{u} + u' \tag{3.47}$$

This process is called Reynolds averaging, and it can be applied to all variables of the flow. Since turbulence is three-dimensional, derivation operations should be conducted according to three dimensions.

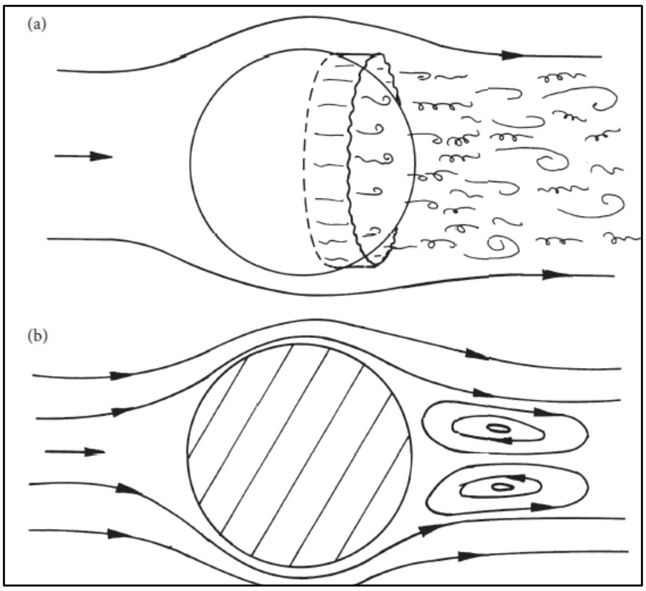

Figure 3.8. The velocity field of the flow around a sphere [56]

Reynolds averaged navier–stokes equations (RANS)

Application of the statistical rules yields the Reynolds-averaged equations for incompressible flow as

$$\frac{\partial \bar{u}}{\partial x}+\frac{\partial \bar{v}}{\partial y}+\frac{\partial \bar{w}}{\partial z}=0$$

$$\rho\left[\frac{\partial \bar{u}}{\partial t}+\bar{u}\frac{\partial \bar{u}}{\partial x}+\bar{v}\frac{\partial \bar{u}}{\partial y}+\bar{w}\frac{\partial \bar{u}}{\partial z}\right]=\rho g_x-\frac{\partial \bar{P}}{\partial x}$$

$$+\mu\left(\frac{\partial^2 \bar{u}}{\partial x^2}+\frac{\partial^2 \bar{u}}{\partial y^2}+\frac{\partial^2 \bar{u}}{\partial z^2}\right)-\rho\left[\frac{\partial \overline{u'u'}}{\partial x}+\frac{\partial \overline{u'v'}}{\partial y}+\frac{\partial \overline{u'w'}}{\partial z}\right]$$

$$\rho\left[\frac{\partial \bar{v}}{\partial t}+\bar{u}\frac{\partial \bar{v}}{\partial x}+\bar{v}\frac{\partial \bar{v}}{\partial y}+\bar{w}\frac{\partial \bar{v}}{\partial z}\right]=\rho g_y-\frac{\partial \bar{P}}{\partial y}$$

$$+\mu\left(\frac{\partial^2 \bar{v}}{\partial x^2}+\frac{\partial^2 \bar{v}}{\partial y^2}+\frac{\partial^2 \bar{v}}{\partial z^2}\right)-\rho\left[\frac{\partial \overline{v'u'}}{\partial x}+\frac{\partial \overline{v'v'}}{\partial y}+\frac{\partial \overline{v'w'}}{\partial z}\right]$$

$$\rho\left[\frac{\partial \bar{w}}{\partial t}+\bar{u}\frac{\partial \bar{w}}{\partial x}+\bar{v}\frac{\partial \bar{w}}{\partial y}+\bar{w}\frac{\partial \bar{w}}{\partial z}\right]=\rho g_z-\frac{\partial \bar{P}}{\partial z}$$

$$+\mu\left(\frac{\partial^2 \bar{w}}{\partial x^2}+\frac{\partial^2 \bar{w}}{\partial y^2}+\frac{\partial^2 \bar{w}}{\partial z^2}\right)-\rho\left[\frac{\partial \overline{w'u'}}{\partial x}+\frac{\partial \overline{w'v'}}{\partial y}+\frac{\partial \overline{w'w'}}{\partial z}\right] \quad (3.48)$$

In the tensorial form:

$$\rho\left[\frac{\partial \overline{u}_i}{\partial t}+u_j\frac{\partial \overline{u}_i}{\partial x_j}\right]=\rho g_i-\frac{\partial \overline{P}}{\partial x_i}+\mu\frac{\partial^2\overline{u}_i}{\partial x_j\partial x_j}-\rho\left(\frac{\partial \overline{u_i'u_j'}}{\partial x_j}\right)$$

or (3.49)

$$\frac{\partial \overline{u}_i}{\partial t}+u_j\frac{\partial \overline{u}_i}{\partial x_j}=g_i-\frac{1}{\rho}\frac{\partial \overline{P}}{\partial x_i}+\upsilon\frac{\partial^2\overline{u}_i}{\partial x_j\partial x_j}-\left(\frac{\partial \overline{u_i'u_j'}}{\partial x_j}\right)$$

The term $\rho\overline{u_i'u_j'}$ (usually referred as $\overline{u_i'u_j'}$) found in equation (3.49) refers to the Reynolds stress tensor R_{stress}. These stresses are due to turbulent flow, and it is an approach, supported by experiments to express the physical stresses in a turbulent flow more accurately in mathematical terms. It is also called the Boussinesq approximation. In some cases, it is recommended to use non-linear versions of this approach.

Reynolds stress tensor is

$$R_{stress}=\overline{u_i'u_j'}=\begin{pmatrix}\overline{u'u'} & \overline{u'v'} & \overline{u'w'}\\ \overline{v'u'} & \overline{v'v'} & \overline{v'w'}\\ \overline{w'u'} & \overline{w'v'} & \overline{w'w'}\end{pmatrix} \tag{3.50}$$

The diagonal elements of this tensor represent the normal stresses, while the other elements represent the shear stresses.

<u>Reynolds-averaged energy (enthalpy) equation</u>

When statistical operations are applied, the time-averaged energy (enthalpy) equation is:

$$\begin{aligned}\rho c_p\left[\frac{\partial \overline{T}}{\partial t}+u\frac{\partial \overline{T}}{\partial x}+v\frac{\partial \overline{T}}{\partial y}+w\frac{\partial \overline{T}}{\partial z}\right]&=k\left(\frac{\partial^2\overline{T}}{\partial x^2}+\frac{\partial^2\overline{T}}{\partial y^2}+\frac{\partial^2\overline{T}}{\partial z^2}\right)-\rho c_p\left[\frac{\partial \overline{T'u'}}{\partial x}+\frac{\partial \overline{T'v'}}{\partial y}+\frac{\partial \overline{T'w'}}{\partial z}\right]\\&+\left[\frac{\partial \overline{P}}{\partial t}+u\frac{\partial \overline{P}}{\partial x}+v\frac{\partial \overline{P}}{\partial y}+w\frac{\partial \overline{P}}{\partial z}+\frac{\partial \overline{P'u'}}{\partial x}+\frac{\partial \overline{P'v'}}{\partial y}+\frac{\partial \overline{P'w'}}{\partial z}\right]\end{aligned} \tag{3.51}$$

3.5.2. Turbulence models

In RANS, it was mentioned that the Reynolds tensor $\overline{u_i'u_j'}$ causes 6 unknown expressions to appear, resulting in a closure problem. In addition, there are unknowns in the energy/enthalpy equation that arise due to scalar (pressure and temperature) transported properties $\rho\overline{\varphi' u_i'}$. To close the problem, additional equations must be derived so that the number unknown variables and the number of equations is equal. There are number of turbulence models developed regarding this problem. Two equation turbulence models are among the most prevalent turbulence models. Models such as the k-epsilon and k-omega models have become standard tools in the industry and are utilized for the majority of engineering challenges. Two-equation turbulence models continue to be an important area of research, and new, enhanced two-equation models are being produced. Two-equation models require incorporate two additional transport equations to account for the turbulent features of the flow. This enables a two-equation model to account for history effects such as convection and diffusion of turbulent energy. A brief explanation and equations of k-epsilon model which is also the base of k-omega will be given in the following sections.

3.5.3. Eddy viscosity and eddy diffusivity

The k-epsilon turbulence model was created based on the assumption that there is a connection between the effects of viscous stresses and the effects of Reynolds stresses. Both stresses are seen on the right side of the momentum equation, and in Newton's law of viscosity it is assumed that viscous stresses are proportional to the deformation rate of fluid elements. Accordingly, if the stress tensor is remembered:

$$\tau_{ij} = \mu s_{ij} = \mu\left(\frac{\partial u_i}{\partial x_j} + \frac{\partial u_j}{\partial x_i}\right) \tag{3.52}$$

Boussinesq proposed in 1877 that Reynolds stresses could similarly be proportional to average deformation velocities:

$$R = \overline{u_i' u_j'} = \nu_t \left(\frac{\partial \overline{u_i}}{\partial x_j} + \frac{\partial \overline{u_j}}{\partial x_i} \right) - \frac{2}{3} k \, \delta_{ij}$$

$$k = \frac{1}{2}\left(\overline{u'^2} + \overline{v'^2} + \overline{w'^2}\right) = \frac{1}{2}\left(\overline{u_i'} \cdot \overline{u_i'}\right) \text{ and } \delta_{ij} = \begin{pmatrix} 1 & 0 & 0 \\ 0 & 1 & 0 \\ 0 & 0 & 1 \end{pmatrix} \tag{3.53}$$

Here, the term turbulent kinetic energy *k* per unit mass is used. The other term ν_t represents the kinematic turbulent viscosity. The term $2\,k\,\delta_{ij}\,/\,3$ considers the Reynolds stress in normal direction (the isotropic part of the tensor).

The temperature and other scalar features in a turbulent flow can be modeled in an analogous way. The transfer of a scalar magnitude in a turbulent flow can be taken as being proportional to the gradient of the average value of the transported quantity.

$$-\rho \overline{\mathrm{u}_i' \phi'} = \Gamma_t \frac{\partial \overline{\phi}}{\partial x_i} \tag{3.54}$$

Here Γ_t is used as the turbulence diffusivity. Since turbulent transfer of momentum and heat is caused by the same mechanism, i.e., vortex mixture- the turbulent diffusivity is quite close to the turbulent viscosity μ_t. For that reason, turbulent Prandtl/Schmidt number $\mathrm{Pr\,Sc}_t$ is used in RANS models

$$\mathrm{Pr\,Sc}_t = \frac{\mu_t}{\Gamma_t} \tag{3.55}$$

Many flow experiments have shown that the Prandtl/Schmidt number is almost constant. In addition, many CFD solver take this value as a unity [57].

Basically k-epsilon model [58] is a turbulence model that involves the transport of turbulence properties by convection and diffusion, and the effects of the production and destruction of turbulence. The model's assumption is that the turbulent viscosity is isotropic. In other words, the ratio between Reynolds stress and the average deformation rate is the same in all three directions. The standard k-epsilon model has equations, based on the corresponding processes that cause changes in k and epsilon (dissipation of kinetic energy) values. By performing dimensional analysis, turbulent viscosity is obtained:

$$\mu_t = C\rho v l = \rho C_\mu \frac{k^2}{\varepsilon} \tag{3.56}$$

Here it C_μ is a unitless constant. The standard model consists of the following equations

$$\frac{\partial(\rho k)}{\partial t} + div(\rho k\bar{u}) = div\left[\frac{\mu_t}{\sigma_k} grad(k)\right] + 2\mu_t \overline{s_{ij}} \cdot \overline{s_{ij}} - \rho\varepsilon \tag{3.57}$$

$$\frac{\partial(\rho\varepsilon)}{\partial t} + div(\rho\varepsilon\bar{u}) = div\left[\frac{\mu_t}{\sigma_\varepsilon} grad(\varepsilon)\right] + C_{1\varepsilon}\frac{\varepsilon}{k} 2\mu_t \overline{s_{ij}} \cdot \overline{s_{ij}} - C_{2\varepsilon}\rho\frac{\varepsilon^2}{k} \tag{3.58}$$

The constants in these equations are as follows as a result of extensive experiments

$$\begin{aligned} C_\mu &= 0.09 \\ C_k &= 1.00 \\ \sigma_\varepsilon &= 1.30 \\ \sigma_{1\varepsilon} &= 1.44 \\ \sigma_{2\varepsilon} &= 1.92 \end{aligned} \tag{3.59}$$

3.6. Convection over a Rotating Disk

The first significant understanding and similarity solutions of the flow over a rotating disk in still air has been realized by von Karman [59]. Flow over a rotating disk has its unique behavior such that rotating wall creates radial pump effect via the no-slip condition and centrifugal force. And because of the continuity (mass conversation), new fluid molecules are axially driven to the disk plane. This flow structure continuously repeating itself as the disk rotates. Regarding the flow behavior there exists three-dimensional flow with radial, tangential and axial velocity components (u_r, u_φ and u_z). These components form three boundary layers, and a temperature boundary layer also forms when the disk wall has a different temperature level than the ambient air, see Figure 3.9.

Figure 3.9 presents a schematic of a stationary axisymmetric problem of convective heat transfer over a rotating disk, in which the axis of symmetry is the z-axis with a stationary cylindrical coordinate system. The point $z = 0$ located on the disk surface. If the angular velocity is high, gravitational effects are insignificant. The Navier-Stokes and energy equations for laminar flow in the case in a stationary cylindrical coordinate system [60–62]

$$\frac{\partial u_r}{\partial r}+\frac{u_r}{r}+\frac{\partial u_z}{\partial z}=0 \tag{3.60}$$

$$\begin{aligned}
&u_r\frac{\partial u_r}{\partial r}+u_z\frac{\partial u_r}{\partial z}-\frac{u_\theta^2}{r}=-\frac{1}{\rho}\frac{\partial P}{\partial r}+\nu\left(\frac{\partial^2 u_r}{\partial r^2}+\frac{1}{r}\frac{\partial u_r}{\partial r}-\frac{u_r}{r^2}+\frac{\partial^2 u_r}{\partial z^2}\right)\\
&u_r\frac{\partial u_\theta}{\partial r}+u_z\frac{\partial u_\theta}{\partial z}+\frac{u_r u_\theta}{r}=\nu\left(\frac{\partial^2 u_\theta}{\partial r^2}+\frac{1}{r}\frac{\partial u_\theta}{\partial r}-\frac{u_\theta}{r^2}+\frac{\partial^2 u_\theta}{\partial z^2}\right)\\
&u_r\frac{\partial u_z}{\partial r}+u_z\frac{\partial u_z}{\partial z}=-\frac{1}{\rho}\frac{\partial P}{\partial z}+\nu\left(\frac{\partial^2 u_z}{\partial r^2}+\frac{1}{r}\frac{\partial u_z}{\partial r}+\frac{\partial^2 u_z}{\partial z^2}\right)
\end{aligned} \tag{3.61}$$

$$\frac{\partial T}{\partial t}+u_r\frac{\partial T}{\partial r}+u_z\frac{\partial T}{\partial z}=\lambda\frac{1}{r}\frac{\partial}{\partial r}\left[r\left(\frac{\partial T}{\partial r}\right)\right]+\lambda\frac{\partial^2 T}{\partial z^2} \tag{3.62}$$

In the region $z > 0$ and $r < R$, the no-slip boundary conditions for the rotating surface are as follows

$$\left.\begin{aligned}
u_r&=0,\\
u_\theta&=r\,\omega\\
u_z&=0\\
T&=T_w
\end{aligned}\right\}\text{at } z=0$$
$$\left.\begin{aligned}
u_r&=0\\
u_\varphi&=0
\end{aligned}\right\}\text{as } z\to\infty \tag{3.63}$$

The value of the axial velocity u_z is not given in boundary conditions as z approaches infinity. To supply the necessary flow for the disk pumping action, it adjusts to a nonzero negative value in the boundary layer.

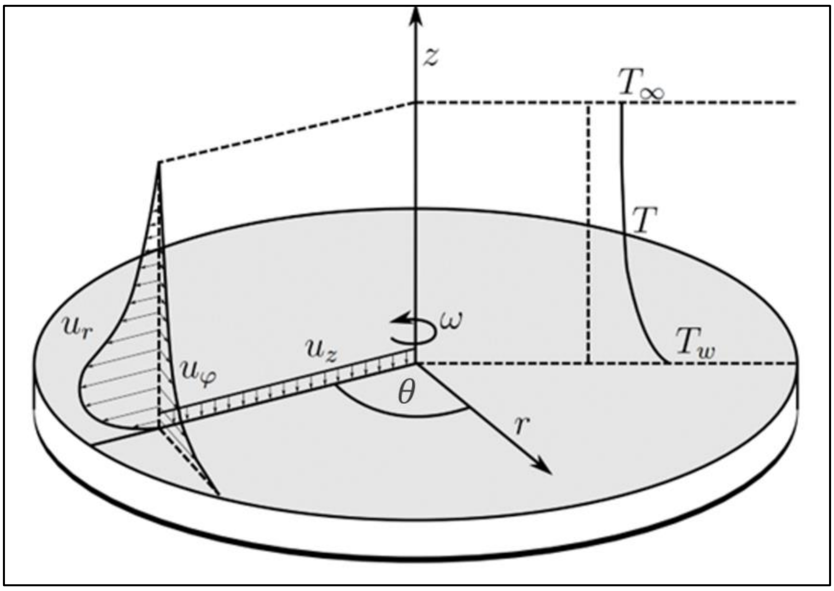

Figure 3.9. Boundary layers over a heated rotating disk in still air [63]

Assumptions in the case of boundary layer approximation [61,62]:

- u_r and u_θ the components are considerably larger than the u_z component,
- The speed and temperature vary more drastically in the z-direction than in the r-direction.
- The change of static pressure in the z-direction can be ignored.

Then the RANS equations for free rotating disk becomes

$$\frac{\partial u_r}{\partial r}+\frac{u_r}{r}+\frac{\partial u_z}{\partial z}=0 \tag{3.64}$$

$$u_r\frac{\partial v_r}{\partial r}+u_z\frac{\partial u_r}{\partial z}-\frac{u_\theta^2}{r}=-\frac{1}{\rho}\frac{\partial P}{\partial r}+\frac{1}{\rho}\frac{\partial u_r}{\partial z}$$

$$u_r\frac{\partial u_\theta}{\partial r}+u_z\frac{\partial u_\theta}{\partial z}+\frac{u_r u_\theta}{r}=\frac{1}{\rho}\frac{\partial u_\theta}{\partial z} \tag{3.65}$$

$$\frac{1}{\rho}\frac{\partial P}{\partial z}=0$$

$$\frac{\partial T}{\partial t}+u_r\frac{\partial T}{\partial r}+u_z\frac{\partial T}{\partial z}=-\frac{1}{\rho c_p}\frac{\partial q}{\partial z} \tag{3.66}$$

The boundary layer equations can be used with the following shear stress and heat flux definitions including turbulent diffusivities for the momentum and heat transfer.

$$\tau_r = \mu \frac{\partial u_r}{\partial z} - \rho \overline{u_r' u_z'}$$
$$\tau_\theta = \mu \frac{\partial u_\theta}{\partial z} - \rho \overline{u_\theta' u_z'} \tag{3.67}$$
$$q = -\left(\lambda \frac{\partial T}{\partial z} - \rho c_p \overline{T' u_z'} \right)$$

The pressure at edge of the boundary layer is equal to the pressure in the potential flow zone, that is, $P = P_\infty$ do not change in the z direction. In this case, the complementary equation in the potential flow (free-stream) region is

$$\frac{1}{2} \frac{\mathrm{d}u_{r,\infty}^2}{\mathrm{d}r} - \frac{u_{\varphi,\infty}^2}{r} = -\frac{1}{\rho} \frac{\mathrm{d}P_\infty}{\mathrm{d}r} \tag{3.68}$$

<u>Exact Navier-Stokes equations for laminar flow over a rotating disk</u>

The approach for an analysis is to translate the Navier-Stokes equations into an exact set of ordinary differential equations that can be solved numerically or with any other method. As indicated above, von Kármán were the first to explore this topic [59] and then Cochran's study [64] followed him.

There is also a similarity solution for the energy equation that satisfies von Karman similarity equations over the rotating disk. The solution of the energy equation was first realized by Kibel [65] for only Pr = 1. Two related study after Kibel has extended the range of Prandtl numbers with their new methods [66,67]. Then, the solutions have been found in a faster and more accurate way with the advances in numerical solutions of the differential equations using proper initial conditions [61].

In order to obtain the exact equations, non-dimensional parameters are defined

$$u_r = r\,\omega F(\zeta)$$
$$u_\varphi = r\,\omega G(\zeta) \tag{3.69}$$
$$u_z = \sqrt{\nu\,\omega}\, H(\zeta)$$
$$p = \rho\,\nu\,\omega P(\zeta)$$

Von Karman’s exact Navier-Stokes equations for laminar flow over a rotating disk is then by substitution of non-dimensional parameters in equation (3.69) become [50,61]

$$\begin{aligned} &H' + 2F = 0 \\ &F'' + G^2 - F^2 - F'H = 0 \\ &G'' - 2FG - HG' = 0 \\ &P' - 2FH + 2F' = 0 \end{aligned} \tag{3.70}$$

Where prime denotes for differentiation with respect to the non-dimensional axial coordinate $\zeta = z\left(\frac{\omega}{\nu}\right)^{\frac{1}{2}}$.

The boundary conditions of the equation (3.70) are given as

$$\begin{aligned} &F(0) = H(0) = P(0) = 0 \\ &G(0) = 1 \\ &F(\infty) = G(\infty) = 0 \end{aligned} \tag{3.71}$$

In equation (3.70) the *P* is not coupled to *F*, *G* and *H*, therefore it can be calculated after the *F*, *G* and *H* are obtained. The solution of the set of non-linear equations (3.70) is obtained by Python in this thesis with Runge-Kutta (RK4) method both for the exact Navier-Stokes equation and energy equations (this will be explained in the next paragraph). The step-size is $\Delta\zeta = 0.0033$. The terms *F, G, H* and *P* stands for non-dimensional variables u_r, u_φ, u_z and *p* (pressure). Graphical representation of the non-dimensional variables through the numerical solution of the equation is shown in Figure 3.10.

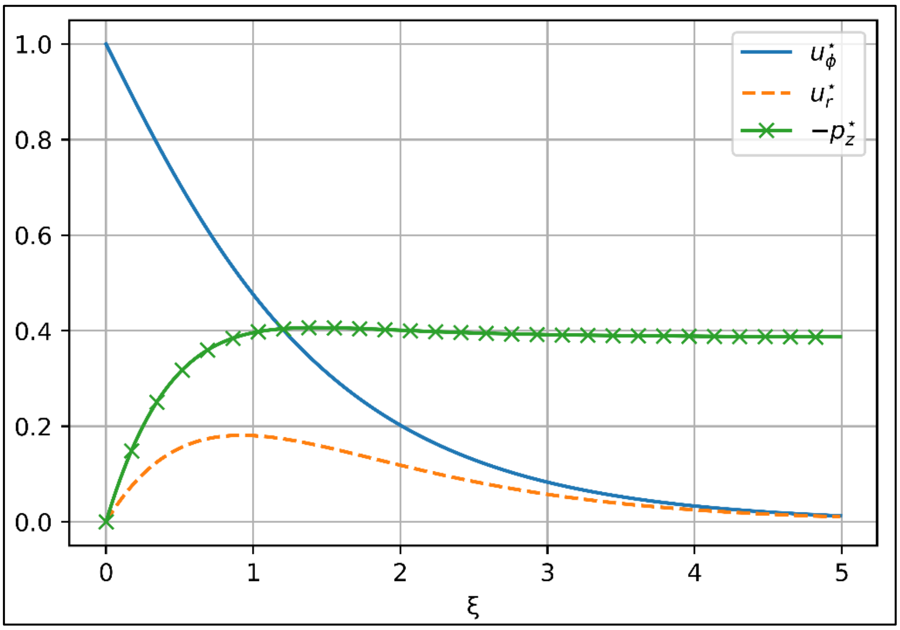

Figure 3.10. Non-dimensional flow variables over a rotating disk

Temperature distribution with the solution of exact energy equation

For a laminar flow over a heated rotating disk the temperature distribution assumes

$$T(r,\zeta) = T_\infty + \Theta_0(\zeta) + \left(\frac{r}{R}\right)^2 \Theta_2(\zeta) \tag{3.72}$$

The functions Θ_0 and Θ_2 are defined as

$$\begin{aligned} \Theta_0(\zeta) &= (T_{wall} - T_\infty)\,\alpha(\zeta) + \frac{\omega^2 r^2}{c_{p,\,air}} \frac{1}{\mathrm{Re}_\omega} \beta(\zeta) + \frac{1}{\mathrm{Re}_\omega} T_n\,\gamma(\zeta) \\ \Theta_2(\zeta) &= T_n\,\varepsilon(\zeta) + \frac{\omega^2 r^2}{c_{p,\,air}} \eta(\zeta) \end{aligned} \tag{3.73}$$

With boundary conditions

$$\begin{aligned} &\Theta_0(0) = T_w - T_\infty,\ \Theta_0(\zeta) \to 0 \ \ as\ \zeta \to \infty \\ &\Theta_2(0) = T_n,\ \Theta_0(\zeta) \to 0 \ \ as\ \ \zeta \to \infty \end{aligned} \tag{3.74}$$

For a disk having an isothermal temperature distribution, Θ_2 approaches zero. This will be the case in experimental investigations in this thesis.

Solutions of Θ_0 and Θ_2 in equation (3.73) are found by solution of the following set of equations [61]

$$\begin{aligned}
&\alpha'' - \Pr H\alpha' = 0\\
&\beta'' - \Pr H\beta' + 4\eta + 12\Pr F^2 = 0\\
&\gamma'' - \Pr H\gamma' + 4\varepsilon = 0\\
&\varepsilon'' - \Pr\left(H\varepsilon' - 2F\varepsilon\right) = 0\\
&\eta'' - \Pr\left(H\eta' + 2F\eta\right) - \Pr\left(F'^2 + G'^2\right) = 0
\end{aligned} \tag{3.75}$$

With the boundary conditions

$$\begin{aligned}
&\alpha(0) = \varepsilon(0) = 1, \quad \beta(0) = \gamma(0) = \eta(0) = 0\\
&\alpha(\zeta),\ \beta(\zeta),\ \gamma(\zeta),\ \varepsilon(\zeta),\ \eta(\zeta) \to 0 \ \ as\ \zeta \to \infty
\end{aligned} \tag{3.76}$$

The symbols $\alpha,\ \beta,\ \gamma,\ \varepsilon$ and η in equation (3.76) are used strictly for this chapter. Prandtl number for air is taken as 0.71. Non-dimensional u_r, u_θ and temperature profile in boundary layer are first calculated through the solution of the non-linear equation system, then they can be dimensionalized by substituting the necessary geometrical and physical parameters. These parameters are used for the validation of the developed conjugate heat transfer model of the rotating disk in this thesis.

Key parameter in the is experimental part of this thesis is the Nusselt number over a rotating disk. The experimental Nusselt number correlation for convective flow over a free rotating disk is defined in literature as [68]:

$$Nu = K \cdot Re_\omega^{c_R} \tag{3.77}$$

The coefficient K governed by the flow behavior (laminar, transition, or turbulent), Prandtl number of the air and the temperature distribution at the disk surface [69]. The coefficient K

for laminar flow is found within the range of 0.32 - 0.4 but a relatively recent study in this area has yielded K= 0.36 while c_R for laminar flow is 0.5 [42]. For a turbulent flow over a rotating disk, Dorfman [60] has derived a relation for the Nusselt number using an integral method.

$$K = 0.0186\left(n_* + 2.6\right)^{0.2} \mathrm{Pr}^{0.6} \tag{3.78}$$

Where n_* is 0.6 for the constant heat flux boundary condition and c_R is 0.8 in equation (3.77). Dorfman correlation will be used in the representation of the experimental results with the highest rotational Reynolds number.

Experimental studies on the determination of critical Reynolds number $Re_{\omega,cr}$ (at the onset of instability) have reported several values over the smooth rotating disk in still air. Experiments with HWA [44,45,70–72] showed consistently that the range of $Re_{\omega,cr}$ was between $8.6\times10^4 - 9.5\times10^4$. Other measurement techniques such as acoustic measurements, visualization with kaolin, naphthalene and mass transfer coefficient (electrochemistry) reported different values that are a bit apart from the range that is provided through HWA measurements given above [62]. Apart from the measurement technique, various levels of roughness, vibrations, and other factors that could have occurred during experimental investigations could have contributed to the discrepancies between various sets of data. Therefore, reference range for $Re_{\omega,cr}$ will be taken from the experiments with HWA [44,45,70–72].

Tangential skin friction over a rotating disk is one of the key parameters to obtain a good insight on the flow behavior. An experiment on a rotating disk in still air with high rotational Reynolds number ($\mathrm{Re}_\omega = \omega r^2 / \nu$) was performed to investigate and determine the parameters related to the turbulent boundary layer by Itoh&Hasegawa [73]. The study focused on very near-wall velocity profile and consequently the wall shear stress. They found out that resulting skin friction coefficient distribution over the disk radius has laminar, transitional and turbulent regime as expected. Skin friction coefficient in laminar regime was well-agreed with the theoretical relationship of Cochran [64] who solved the equations derived by von Karman [59]. Apart from that, Itoh&Hasegawa [73] has derived a relationship for the turbulent regime corresponding to their experimental results. These two relationships are given as

$$C_{f\theta} = 1.2308\,\mathrm{Re}_{\omega}^{-1/2} \tag{3.79}$$

$$C_{f\theta} = 0.0553\,\mathrm{Re}_{\omega}^{-1/5} \tag{3.80}$$

The equation (3.79) is for the laminar region while the equation (3.80) is for the turbulent regime. Turbulent kinetic energy (TKE) is also an important parameter on evaluating the structure of boundary layer of a flow under investigation. It is an experimentally determined parameter and it can be used as a step in the validation of a developed/simulated CFD model which simulates a turbulent flow. TKE is defined as the kinetic energy of fluctuating velocity in the turbulent flow.

$$TKE = \frac{1}{2}\left(\overline{u_r'^2} + \overline{u_\theta'^2} + \overline{u_z'^2}\right) \tag{3.81}$$

TKE distribution in boundary layer from Itoh&Hasegawa [73] will be used for comparing the results of CFD model in this study.

Last point regarding importance of CFD modeling of rotating disk is that the theoretical/analytic approaches yield satisfactory results in problems with simple geometry and boundary conditions [74]. However, in other cases, computational methods gain importance. In the studies on rotating disks, RANS approach, and LES (Large-Eddy Simulations) were used in commercial CFD codes [75]. Shevchuk noted that when a smooth mesh is used, the accuracy of the results produced by in-house code codes or commercial codes depends largely on the choice of the turbulence model.

3.7. Computational Fluid Dynamics

Partial differential equations obtained for fluid mechanics analysis can be solved analytically for some simple flow problems. In turn, solutions to complex problems can be obtained through numerical analysis. In numerical analysis, discretization methods are used. These convert differential equations into algebraic equations and allow the approximate solutions to be obtained. The approaches are applied to small regions of space and time, thus obtaining numerical results in discrete regions becomes possible. The accuracy of numerical solutions depends significantly on the quality of the decomposition.

There are differences between calculated results and "reality". These differences occur due to errors in the process of generating numerical solutions that result from each sub-process:

- Differential equations, approaches, or idealizations
- In the process of discretization
- Cyclic (iterative) methods used in the solution of discrete equations.

Unless the simulation time is kept too long, the exact (exact) solution of the discretized equations cannot be obtained. As mentioned, the use of models for numerical solution is becoming a necessity. To validate models, experimental data must be used.

Discretization errors can be reduced by using high-accuracy interpolation/approaches or by smaller discretization dimensions, but this often increases the time and cost of achieving good resolution. A compromise between the duration and the discretization is required.

Consensus is also needed in the solution of discrete equations. Direct solvers that achieve the accurate solutions are rarely used because they are very costly. Iterative methods are more common, but errors caused by stopping the iteration in early phase must be considered carefully.

The data obtained as a result of numerical solutions is converted into forms such as vectors or turbulent quantities. It is important to visualize and interpret the analysis through these forms. However, sometimes there are dangers in which a solution may look good, but not comply with real boundary requirements and fluid properties [76].

3.7.1. Components of numerical solution methods

1. Mathematical model: The starting point of any numerical method is the mathematical model, that is, partial differential equations and boundary conditions. As mentioned earlier, this model may include simplifications of the exact conservation laws.

2. Discretization method: There are many approaches, but the most important ones are: finite difference, finite volume, and finite element methods.
3. Coordinate and base system of vectors: We can choose coordinate systems such as cartesian, cylindrical, and spherical, to be fixed or moving. The choice depends on the problem of the targeted flow. This choice can affect the discretization method and grid type to use. In addition, the system of base vectors (constant or variable, covariant or contravariant, etc.) in which vectors and tensors will be defined should be chosen.
4. Numerical mesh: It divides the solution area into a limited number of subdomains (elements, control volumes, etc.). There are basically structured and unstructured mesh methods. The unstructured mesh is suitable for complex geometries and for the finite volume/element methods.
5. Finite Approximations: After the selection of the mesh type, it is necessary to choose the approximations to be used in the discretization process. In the finite differences method, approximations for derivatives at mesh points should be chosen. In the finite volume method, one of the approximation methods of surface and volume integrals should be selected. The choice affects the correctness of the results. This choice also affects the development speed of the code. There must be compromise here.
6. Solution Method: The result of discretization is a large and non-linear system of algebraic equations. For unstable flows, the initial value problem – the methods used in ordinary differential equations (with the progression of time) are used. If the equations are non-linear, a cyclic scheme is used to solve them. These methods use sequential linearization of equations, and the resulting linear systems are than solved. The choice of solver depends on the type of mesh and the number of nodes contained in each algebraic equation.
7. Convergence Criteria: Finally, the convergence criteria for the cyclic method should be determined. There are usually two cyclic levels: i) inner loops in which linear equations are solved, and ii) outer loops, which deal with the non-linearity and coupled of equations. Deciding when to stop the cyclic process at each level is important for both accuracy and efficiency.

3.7.2. Features of numerical solution methods

The solution method must have some features. In many cases, it is impossible to completely analyze the solution method. Instead, the components of the method are analyzed. It is necessary for the accuracy of the solution that the components have the desired properties.

Consistency

The difference between the discretized solution and the exact solution is called a truncation error. Typically, the Taylor series are expanded using the values of nodes around a point, resulting in a differential expression and a residual expression. For a method to be consistent, the truncation error must be zero when the grid dimension of space and time approaches zero. Truncation error is usually proportional to the mesh size and time-step size values. However, some terms (such as convection terms in high Reynolds number flows or diffusion terms in low Reynolds number flows) may be dominant in a given flow and it may be reasonable to treat them with more accuracy than the others. Therefore, all terms should be discretized with approximations of the same order of accuracy. Even if the approximations are consistent, it does not mean that the solution of the system of discrete equations and the exact solution will be equal (when the grid values approach zero). The solution method must be stable for this to occur, and this is defined below.

Stability

If the numerical solution method does not magnify the errors that arise during the numerical solution process, then this method is said to be stable. Analysis of stability can be difficult, especially when boundary conditions and non-linear conditions exist. Therefore, it is common to analyze the stability of a method for linear problems with fixed coefficients without boundary conditions. Experience shows that the results obtained in this way can often be applied to more complex problems, but there are notable exceptions. The most used approach in analyzing the stability of numerical schemas is the von Neumann method. However, when solving complex, non-linear and coupled equations with complex boundary conditions, we will have several consequences of stability, so we may have to rely on experience and intuition. Several solution methods demand the use of under-relaxation or a time step that is smaller than a predetermined threshold.

Boundedness

Numerical solutions must be within appropriate limits. Quantities that are not physically negative (such as density, kinetic energy of turbulence) must always be positive. In the absence of resources, some equations (for example, the heat equation for temperature when there is no heat source) require that the minimum and maximum values of the variable be located within the boundary conditions of the domain. These conditions must exist in the characteristics of the numerical approach.

The condition of boundedness is difficult to guarantee. Only some first-order schemes guarantee this requirement. All high-order schemes can produce unlimited solutions; But this usually happens with very coarse, so in a solution that involves undershoots or overshoots, it is usually an indication that the errors in the solution are large and that the mesh needs some improvement (at least locally). The problem is that schemes that tend to produce unbounded solutions are likely to have stability and convergence problems.

3.8. Conjugate Heat Transfer

Conjugate heat transfer refers to the state in which solid and fluid substances interact thermally with each other. The heat conduction equation for solid and the Navier-Stokes and energy equation for fluid need to be solved in a coupled way. The solution to such a problem gives the distribution of temperature and heat flux along the solid-fluid interface, and there is no need for a heat transfer coefficient as a boundary condition to calculate temperature distribution on the solid substance. Furthermore, conjugate heat transfer approach in CFD environment results in the determination of heat transfer coefficients and then they can used for further thermal calculations [77].

4. THERMAL MODELING

4.1. Derivation of Governing Equation for Python Model

The braking condition for a railway vehicle is shown in Figure 4.1. Here, the relationship between braking energy and heat flux will be shown with two different approaches.

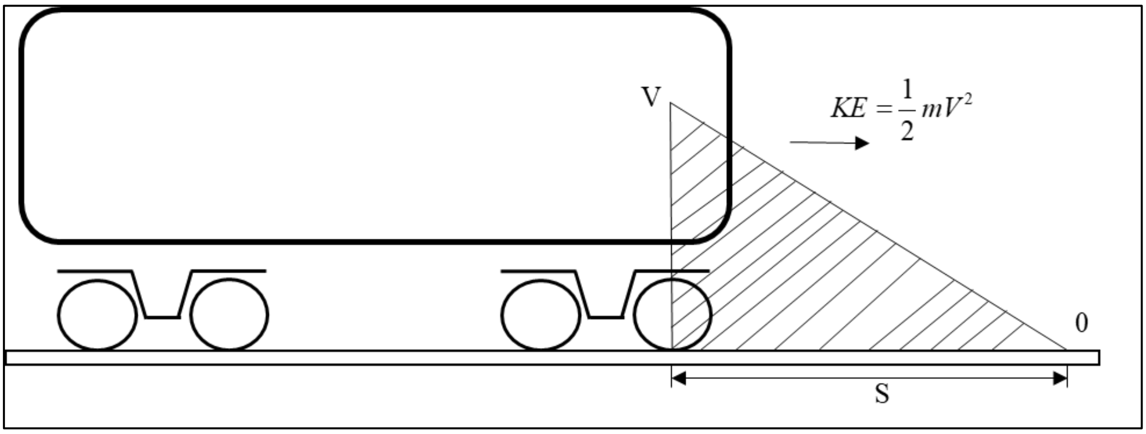

Figure 4.1. Kinetic energy change of a railway vehicle

Brake energy required to slow the railway vehicle from a certain speed

$$E_b = \frac{1}{2} m\left(V_i^2 - V_f^{\,2}\right) + \frac{1}{2} I_w \left(\omega_i^2 - \omega_f^2\right) \tag{4.1}$$

In the above equation, the effect of the vehicle components having rotational motion is considered together with the translational motion. If the angular velocity is expressed in terms of the linear velocity and the arrangement is made, the braking energy becomes

$$E_b = \frac{m}{2} \underbrace{\left(1 + \frac{I_w}{m\, r_w^2}\right)}_{C_{inertia}} \left(V_i^2 - V_f^{\,2}\right) \tag{4.2}$$

In the first approach, the required braking power is calculated by rate of change of kinetic energy $\dot{E}_b$ between the initial and final speeds, regardless of the pad pressure. For the case of slowing down the vehicle with a constant deceleration $\dot{E}_b$ [78]

$$P_b = \frac{dE_b}{dt} = \dot{E}_b \Rightarrow \frac{d\left[\frac{m}{2}C_{inertia}\left(V_i^2 - V_f^{\,2}\right)\right]}{dt}$$
$$\dot{E}_b = mC_{inertia}a\left(V_i - at\right) \tag{4.3}$$

The braking power expressed by this equation will be transferred to the disk and pad as heat energy. There is a heat partition ratio developed for the disk-pad system. The formula that gives the distribution of energy between the disk and pad component is given as [79].

$$\xi = \frac{q_d}{q_p} = \left(\frac{\rho_d C_d k_d}{\rho_p C_p k_p}\right)^{1/2} \tag{4.4}$$

However, for railway brake disk pad case this value can be so small for some cases that it can be ignored. Heat flux to disk with the first approach including the heat partition ratio is then becomes

$$q_d\left(t\right) = \frac{\xi}{A_p\left(\xi + 1\right)} mC_{inertia}a\left(V_i - at\right) \tag{4.5}$$

In the second approach, using the normal force applied to the disk, the normal pressure p_{brake} for a pad is obtained (multiplied by 0.5 to consider only one pad- corresponding the half of the disk-pad system due to the axial symmetry), and then the heat flux into the disk from the area covered by pad is calculated as

$$p_{brake}\left(t\right) = 0.5\frac{F_{brake}\left(t\right)}{A_p}$$
$$q_d\left(r,\theta,t\right) = \mu p_{brake}\left(t\right) r_{eq}\omega\left(t\right) \tag{4.6}$$

Where $\omega\left(t\right) = V\left(t\right)/r_w$.

The model of three-dimensional brake disk for temperature and thermal stress distribution investigation is built with the accurately derived heat flux expressions. The developed model is built using the Python programming language with Numpy [80] and Numba [81] libraries that are specially designed for fast and efficient numerical calculations. Although the developed model has some adjustments and improvements, it incorporated the methodology used in a study by Grzes et al. [25]. One key distinction is that, in this study, FDM (Finite Differences Method) rather than the finite element method is employed to discretize the transient solid energy equation. The use of FDM for structured grids is straightforward, quick, and produces precise solutions for conservation equations [82]. The shape of the pad-covered region and the brake disk's simplified geometry (hollow disk) enable the implementation of FDM in polar coordinates with structured grids. Another distinction is that the pad component's temperature field is not calculated in this study because of the consideration that primary function of the pad on the disk is to be a heat flux source. Furthermore, the pad has relatively low mass, volume, and small geometry compared to the disk. Thus, the computational time is somewhat lowered. The addition of additional time derivatives to boundary conditions is another distinction. This is significant because energy storage using time derivatives in boundary nodes or cells becomes a significant problem in transient solutions [83]. In the continuous braking case, the need for inclusion is considered to be more pronounced because the governing equation and boundary conditions are quite time dependent.

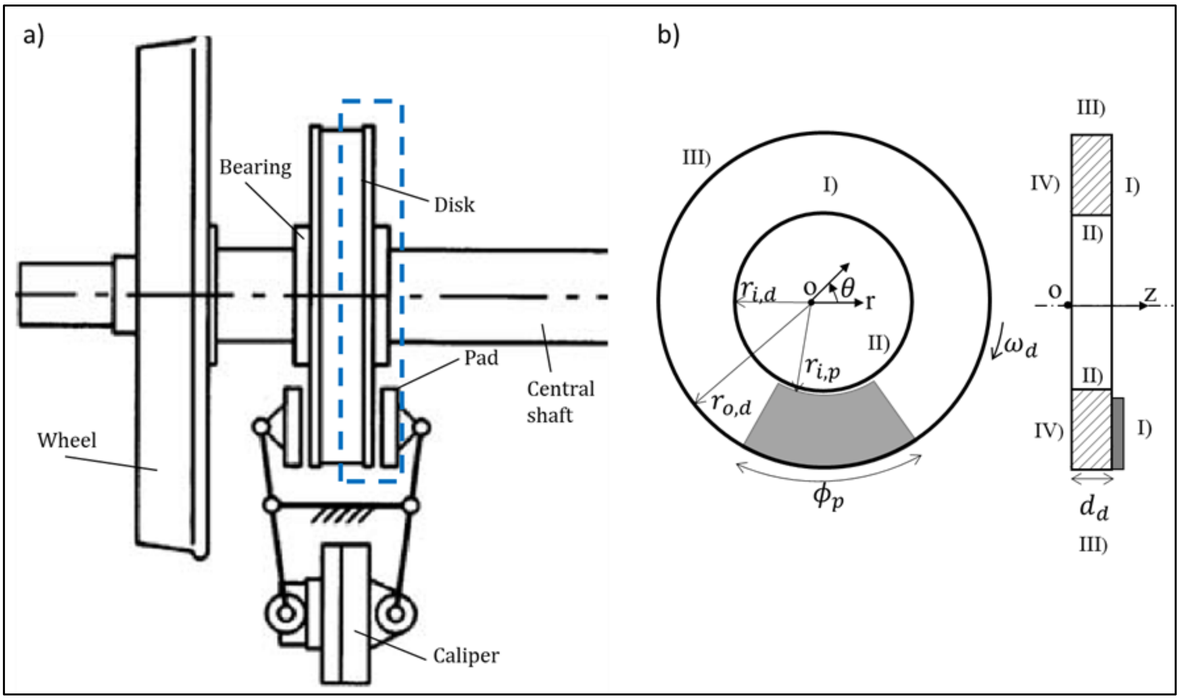

Figure 4.2. Schematic representation of disk-pad system

The 3D-time-dependent equation for the heat conduction in a solid body (disk), without energy generation in the cylindrical coordinate system:

$$\frac{\partial^2 T}{\partial r^2}+\frac{1}{r}\frac{\partial T}{\partial r}+\frac{1}{r^2}\frac{\partial^2 T}{\partial \theta^2}+\frac{\partial^2 T}{\partial z^2}=\frac{1}{\lambda}\frac{\partial T}{\partial t} \tag{4.7}$$

Where $\lambda = k/(\rho c)$. The governing equation (4.7) is discretized with the implicit finite difference scheme, which is unconditionally stable with respect to time-step size. Space derivatives are approximated with a second-order accurate central scheme. Gauss-Seidel iterative linear system solver is used for the solution of algebraic equations. Iterative convergence errors are calculated by L2-norm (i.e., the Euclidean norm), and convergence tolerance between each iteration is chosen as 10^{-7} which is found to be small enough. Discretized forms of the governing equation and boundary conditions are given in Appendix-1.

The disk in the experimental part of Grzes et al. [25] study has cooling ribs that is similar to the disk structure shown in Figure 4.2. Ribs geometry in the numerical model were ignored but their masses were included to account for their cooling effect implicitly. Therefore, thickness of the disk d_d is taken as 25 mm for the simulation in this study, same as the adapted study [25] by ignoring the geometry of the cooling ribs on the inner surface of the disk. However, the mass of ribs is considered by adjusting the thickness of the disk in the model. After initial analyses, this assumption did not significantly alter the results, according to the study [25]. The comparison of the numerical and experimental data in that work shown that, although this assumption slightly reduces the accuracy of the numerical model, it results in a good balance between precision and computational cost.

4.2. Initial and Boundary Conditions

The computational domain of the disk-pad system in Figure 4.2 (a) is highlighted inside the area with dashed lines. Disk and pad geometry with regard to the axial symmetry is shown in Figure 4.2 (b). This symmetry is utilized both in Grzes et al. [25] and the developed model.

Time-dependent heat flux and convection boundary conditions are applied interchangeably at friction plate, i.e., zone I). The area covered by the pad rotates continuously in the developed model. Because of that, the heat flux condition is applied whenever the area of the disk is covered by the pad. In areas not covered by the pad, the convection condition is applied at the friction plate. The convection condition is also applied in zone III and II as there is air flow between the shaft-bearing couple and the inner circumferential surface of the disk, see Figure 4.2. The insulation boundary condition is applied at zone IV due to the axial symmetry of the disk. The uniform initial temperature distribution in the disk is given $T(r,\theta,z,t=0)=27$ °C and it is the same as the ambient air temperature T_∞. Equations for boundary conditions at zones I, II and III are

$$\begin{aligned}
&k_d\frac{\partial T}{\partial z}+\rho_d\,c_d\,\frac{\Delta z}{2}\frac{\partial T}{\partial t}=q_d \text{ at zone I)}\\
&k_d\frac{\partial T}{\partial z}+\rho_d\,c_d\,\frac{\Delta z}{2}\frac{\partial T}{\partial t}=h_\omega\left(T_\infty-T_w\right) \text{ at zone I)}\\
&-k_d\frac{\partial T}{\partial r}+\rho_d\,c_d\,\frac{\Delta r}{2}\frac{\partial T}{\partial t}=h_d\left(T_\infty-T_w\right) \text{ at zone II)}\\
&k_d\frac{\partial T}{\partial r}+\rho_d\,c_d\,\frac{\Delta r}{2}\frac{\partial T}{\partial t}=h_d\left(T_\infty-T_w\right) \text{ at zone III)}
\end{aligned} \tag{4.8}$$

In order to have a realistic heat flux boundary condition, a method is developed to create variable time-step sizes to be implemented in the model. The area covered by the pad (rotates anti-clockwise) travels an angular distance of $\theta_{unit}=2\pi/\,n_\theta$ in the azimuthal direction during each time step. Here, n_θ is the number of nodes in the azimuthal direction. Firstly, the total number of time steps for the simulation is obtained by calculating the total angular distance θ_{total} traveled by the pad

$$\begin{aligned}
&\omega_0=\frac{V_0}{R_w} \text{ and } t_{total}=\frac{0-\omega_0}{a_{dec}}\\
&\theta_{total}=\omega_0\,t_{total}+\frac{1}{2}a_{dec}\,t_{total}^2
\end{aligned} \tag{4.9}$$

By using θ_{total} and θ_{unit} , the total number of time steps becomes $n_t=\frac{\theta_{total}}{\theta_{unit}}$. Angular velocity as a function of time is calculated by

$$\omega(t)_n = \sqrt{\omega(t)_{n-1}^2 + 2\alpha_{dec}\,\theta_{unit}} \tag{4.10}$$

This equation gives the angular velocity value for each time step from the first one to n_t. Here, subscript n represents the current time instant. Finally, using the array of angular velocity obtained from (4.10) , the array of non-uniform time step-size is obtained

$$t_n = t_{n-1} + \frac{\left[\omega(t)_n - \omega(t)_{n-1}\right]}{\alpha_{dec}} \tag{4.11}$$

Using (4.10) and (4.11) , the pad area through which the heat flux boundary condition is implemented rotates by the amount of θ_{unit} at pre-defined variable angular velocity in each time step. The solution of the governing equation (4.7) is also carried out with the obtained non-uniform time-step size to match the time-dependent heat flux boundary condition.

Time evolution of the braking force in the brake test-rig according to EN 14535-3 has two main phases; initially, the brake-force increases linearly from 0 to F_{fill} (N) until the time of filling of the brake cylinder t_{fill} and just after that instant, the force reaches its maximum constant value F_{max} [84]. Figure 4.3 represents the non-dimensional braking force history starting from the beginning to end of braking with the highlighted t_{fill} , F_{fill} and F_{max} parameters.

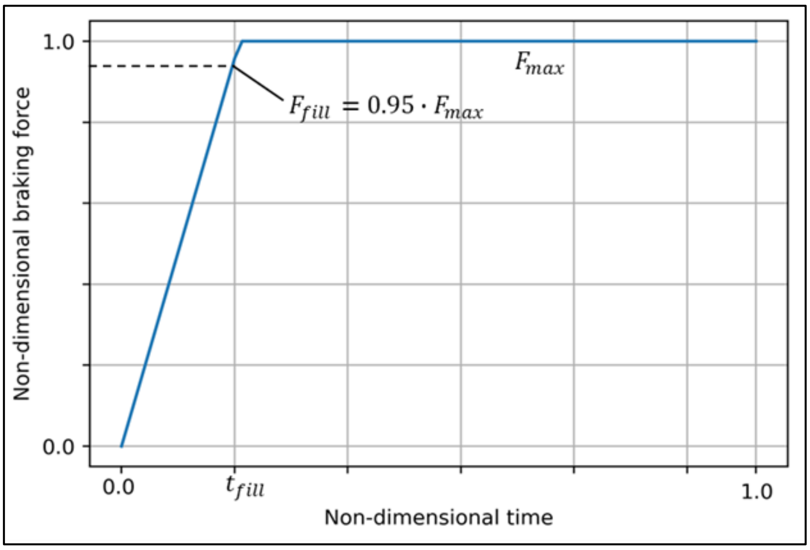

Figure 4.3. Non-dimensional braking force history during a braking process

Time-dependent HTC for the friction plate of the disk in still air can be calculated using the mean Nusselt number derived from convective heat transfer experiments. They are given as

$$Nu_m = \frac{h\, r_d}{k_{air}} = K_m \cdot \mathrm{Re}_\omega^{c_R}\left(t\right)$$
$$\text{where } \mathrm{Re}_\omega = \frac{\omega\left(t\right)\, r_{o,d}^2}{\nu} \tag{4.12}$$

K_m values is governed by the flow behavior (laminar, transition, or turbulent), Prandtl number of the air, and the temperature distribution at the disk surface [85]. Due to the transient nature of the braking process, correlations that best corresponds to laminar [86], transition [16] and turbulent flow [60] cases over the heated rotating disk are considered.

$$h_\omega = \begin{cases} \dfrac{0.36\,\mathrm{Re}_\omega^{0.5}\,k_{air}}{r_{o,d}}, & \mathrm{Re}_\omega < 1.95\times10^5 \\ \dfrac{10^{-19}\,\mathrm{Re}_\omega^{4}\,k_{air}}{r_{o,d}}, & 1.95\times10^5 \le \mathrm{Re}_\omega < 2.5\times10^5 \\ \dfrac{0.0149\,\mathrm{Re}_\omega^{0.8}\,k_{air}}{r_{o,d}}, & 2.5\times10^5 \le \mathrm{Re}_\omega \end{cases} \tag{4.13}$$

Three range of rotational Reynold numbers Re_ω in equation (4.13) represent laminar, transition, and turbulent flow cases, respectively.

4.3. Grid Convergence Analysis

An investigation for mesh independence is done with the following total number of nodes: 22,680 (V1), 41,580 (V2), 83,160 (V3), 122,760 (V4), 236,160 (V5), and 314,880 (V6). Comparing the maximal temperatures, it was observed that the difference between V4 and V6 -which has the finest mesh structure- was about 1%. However, the calculation time has been quadrupled. Therefore, V4 has been chosen with node numbers for radial, azimuthal and axial directions; 31, 360, and 11, respectively. Mesh independence investigation and other mentioned properties of the developed numerical model are implemented in a way that considers criteria in "Editorial Policy Statement on the Control of Numerical Accuracy" of the ASME Journal of Fluids Engineering. This statement is also based on previous studies focusing on the accuracy of CFD models [87,88].

4.4. Material Parameters

All the disk and pad parameters used in the developed model that are also used in the Simcenter STAR-CCM+ model is given in Table 4.1. Thermal and geometrical parameters of the gray cast iron disk and pad are taken from Grzes et al. [25] for the simulation. Mechanical properties of the gray cast iron disk material is taken from [89].

4.5. Thermal Model in Simcenter STAR-CCM+

Simcenter STAR-CCM+ software is a well-established and validated 3-d CFD and multi-physics calculation tool [26]. It uses the finite-volume method for the CFD and computational heat transfer calculations. The same configuration of the developed model with the same mesh structure is built in Simcenter STAR-CCM+. Also, it includes the geometry and thermophysical properties of the pad, which is not considered in the developed model. Geometry and mesh view of the model in Simcenter STAR-CCM+ with temperature acquisition locations are shown in Figure 4.4. The point marked as z = 25 mm in the figure is located at the friction plate of the disk and z = 0 mm is located at inner side of the disk (with zero heat flux condition), they are used for the temperature evolution presentations. The inner points between 0 mm and 25 mm are not shown in this figure but they are between these two points. Z line probe in z-direction is used for recording axial thermal distributions at several time instants. These locations are used both for the developed model and the Simcenter STAR-CCM+ model.

Table 4.1. Physical and geometrical properties of components [25,89]

Property	Disk	Pad
Thermal conductivity, k (W/ (m K))	51	1,59
Specific heat, c (J/ (kg K))	500	770
Density, ρ (kg/m^3)	7100	2450
Thickness, d (mm)	55	25
Outer radius, r_o (mm)	320	318
Inner radius, r_i (mm)	175	178
Area of the pad, A_p (mm^2)	-	33,982 x 10^3
Coverage angle of the pad, ϕ_p (deg)	-	57
Elasticity modulus, E (GPa)	92.99	-
Poisson ratio, υ	0,26	-
Thermal expansion coefficient, α (1/K)	1,55 x 10^{-5}	-

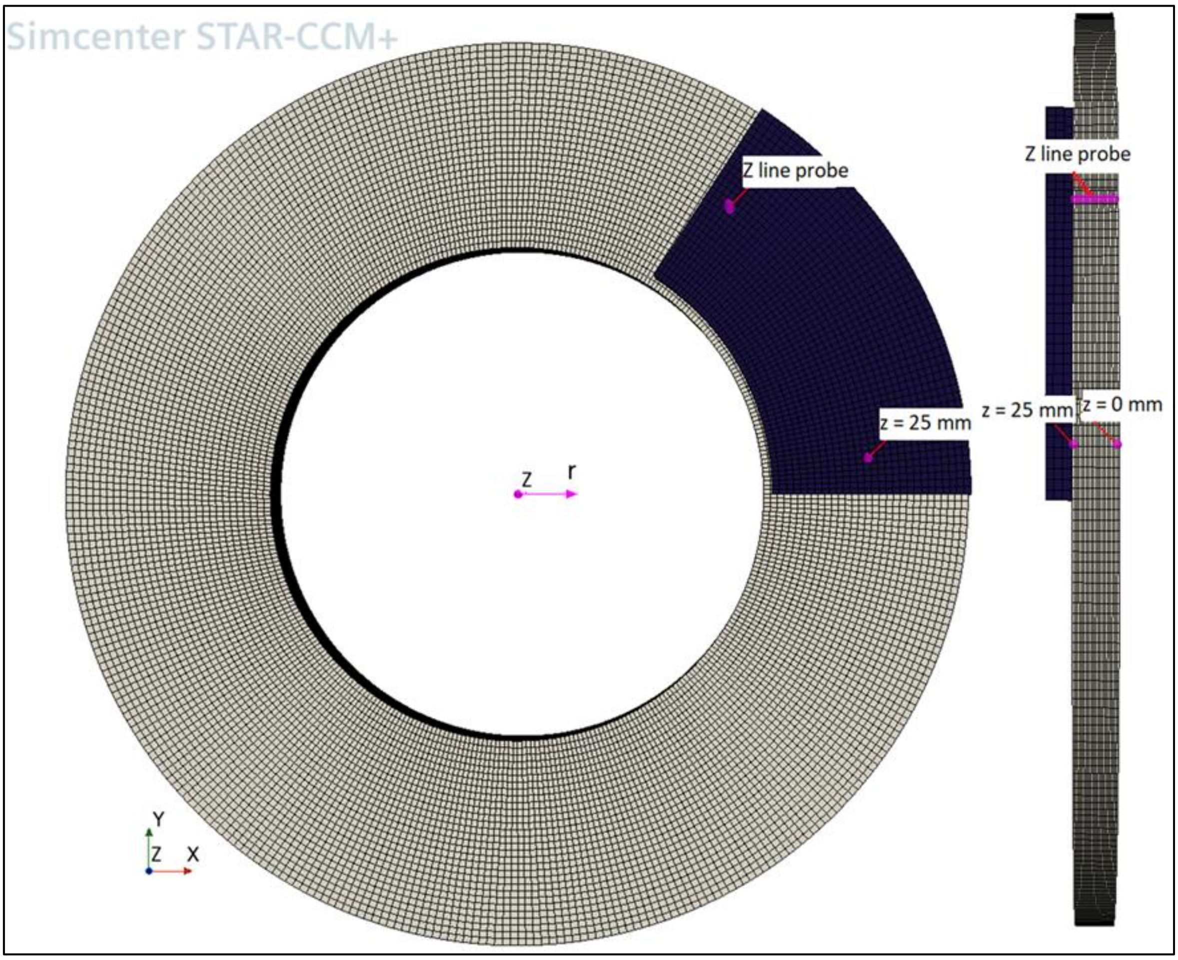

Figure 4.4. Mesh view of the model in Simcenter STAR-CCM+

Four sets of arrays as tabular data are imported from Python. These arrays are time-dependent 1) time-step sizes and 2) angular velocity of the disk for the solution of the discretized governing equation and 3) heat flux profile, and 4) convection coefficients on the friction plate. Boundary conditions for all pad surfaces except for the heat flux in the contact area are chosen as adiabatic since the pad is surrounded by covering materials on its outer surfaces. In this model, the disk rotates, and the pad is static.

Furthermore, this configuration is extended by including the temperature-dependent thermal conductivity and specific heat of the disk. The temperature-dependent data are taken from a study [90] (see Table 4.2 for the variables) that investigated the thermo-mechanical behavior of a gray cast-iron disk with almost the same thermal properties as in the current study. In this way, it is possible to investigate the effect of temperature-dependent properties on the thermal stress distribution of the disk. Hence, comparison between the developed model and Simcenter STAR-CCM+ has also been possible.

Table 4.2. The temperature-dependent properties of gray cast iron disk [90]

Temperature ℃	Specific heat (J/ (kg K))	Thermal conductivity (W/ (m K))
20	469	59,7
100	500	53,7
200	550	50
300	592	46,6
400	630	43,4

4.6. Braking Parameters

The first comparison is made between the outcome of Grzes et al. [25] and the newly developed model using the braking parameters and constant HTC for zone I), II) and III) for braking from 110.1 km/h until the stop. Braking parameters are given in Table 4.3. After that, the developed model and Simcenter STAR-CCM+ are simulated by time-dependent correlation in the zone I with the initial speed of 120 km/h, and their results are compared. Then, the Simcenter STAR-CCM+ model with and without variable thermal properties are simulated, and their results are presented. Then, results of the test cases are shown for the prediction capability of the developed model with higher speeds and various friction coefficients. Graphical representations of thermal stress distributions, using fitting functions obtained from axial thermal distribution, are given for all the cases except the first comparison with Grzes et al. [25] .

In the latest phase of the study, the developed model with constant and variable convection configurations are compared.

Table 4.3. Braking parameters with respect to the braking cases [25]

Parameter	Value
Friction coefficient, μ	0,317
Total braking time, t_{total} (s)	22,12 (110,1 km/h) 24,13 (120 km/h)
Filling time, t_{fill} (s)	4,3
Force at the first phase, F_{fill} (N)	47400
Max brake force, F_{brake} (N)	49500
Constant HTC on disk surfaces, h_d $(\mathrm{W/m^2K})$	100 (110,1 km/h) 109,1 (120 km/h) 127,15 (140 km/h) 145,32 (160 km/h)

4.7. Calculation of Axial Thermal Stress Distribution

Thermal stress distribution over any chosen axial line in the brake disk can be calculated by a flat plate assumption. This approach was validated in the study [34] where brake disk cracks were experimentally investigated. In that study, an expression was derived for the calculation of thermal stresses as a function of the axial temperature distribution *T(z)* of the disk along a chosen line in normal direction to *r*,θ plane as shown in Figure 4.2 (b) and thermo-mechanical properties of the disk using the stress analysis presented in [35]. This model reflects the fact that the brake pressure created by pads does not cause stresses in the disk to exceed the material's elastic limit. The relevant thermal stress distribution in axial direction is given by

$$\sigma_T(z) = \frac{\alpha_T E}{1-\upsilon}\left[-T(z) + \frac{1}{d_d}\int_0^{d_d} T(z)\,dz\right] \tag{4.14}$$

The thermal stress term in the equation (4.14) represents the thermal stress in radial and circumferential direction which are equal to each other according to the assumption that the temperature distribution is symmetrical about middle axial plane of the disk [34]. In general, the temperature field *T(r*,θ*,z,t)* is a function depending on the three spatial coordinates and time. Hereby, the equation can be used for predicting the radial and circumferential thermal stress distribution of the disk when the temperature values from a chosen axial line along the disk thickness at a desired time instant are obtained. One condition for the correct use of it is that the temperature values must be taken at an instant when this line is under the pad pressure. Therefore, the location of Z line probe as shown in Figure 4.4 over which the thermal stress distribution is calculated is chosen such that the maximum temperature levels are reached in this region and it is located inside the area covered by the pad. Apart from that, the equation can be used to obtain the evolution of thermal stress of a point that can be on the friction plate near of which the highest temperature gradients occur.

The resulting thermal stress equation can be seen as a simplified method for the prediction of thermal stress distribution if the chosen locations fulfill the condition mentioned above. Therefore, the equation (4.14) is also utilized in the current study for the axial thermal stress distribution over Z line probe and evolution of thermal stress distribution at several axial points (z = 0, 15 and 25 mm).

Steps of calculation of the thermal stress distribution are explained in the following:

1) Based on numerical simulations, temperature values $T(r,\theta,z,t)$ from the developed or Simcenter STAR-CCM+ model are obtained.
2) A 1-d array of temperature T(z) is created in Python by giving the coordinates of Z line probe (whose r,θ values are known) and choosing any desired time instant. Therefore, this array represents the axial temperature distributions $T(z)$ along the Z line probe for a chosen time instant.
3) A fifth-degree polynomial function $T_{fit}(z)$ from $T(z)$ are created in Python by using polyfit function that uses the least square method to fit the calculated values. Also, the polyint function is used to obtain antiderivative (indefinite integral) of a Tfit (z).
4) The resulting polynomial function $T_{fit}(z)$ is evaluated by using z-coordinate values of Z line probe as inputs.
5) Anti-derivative of Tfit (z) function is evaluated in the interval from 0 to dd.

Then, the obtained values from these evaluations are used in equation (4.14) to obtain the thermal stress distribution over the Z line probe at several time instants.

5. RESULTS AND DISCUSSION OF THERMAL MODEL

To compare the results correctly, temperature evolutions from the disk-pad surface starting from z = 25 mm in the axial direction, consistent with Grzes et al. [25] presentation, are recorded and shown in Figure 5.1. The location of axial point z =25 mm and z = 0 mm for temperature evolutions and Z line probe for axial temperature distribution are shown in Other axial points used for temperature evolutions that are not shown in Figure 4.4 are z = 23, 20 ,15, 10, 5 and 2 mm. (Dashed lines show the results of Grzes et al.)

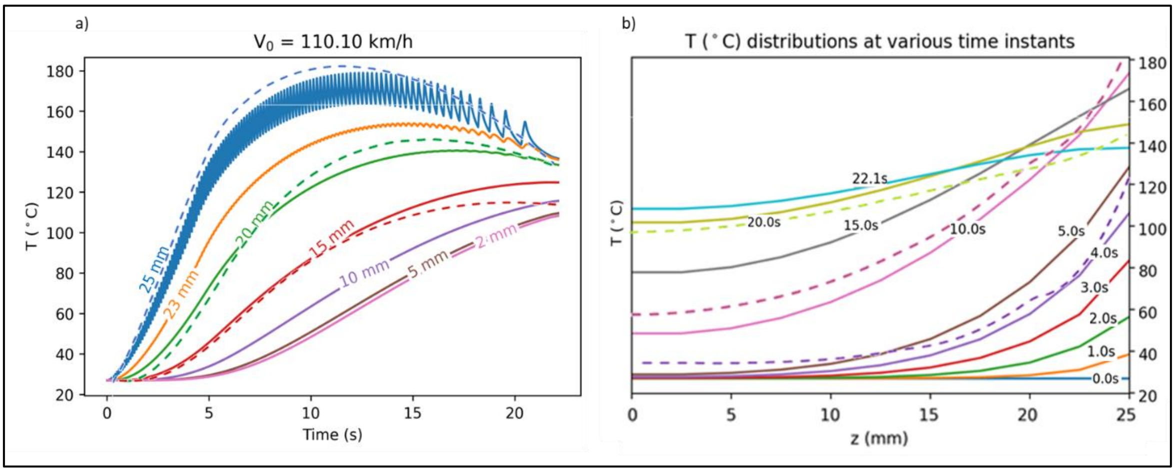

Figure 5.1. Comparison of the developed model with Grzes et al.

Temperature evolutions taken from points 20 mm and 15 mm as shown in Figure 5.1 suggest that the developed model shows a good similarity both in terms of tendency and magnitudes when compared to the results of Grzes et al. However, the developed model slightly underpredicts the temperature values at the friction plate (25 mm) with a maximum difference of 6.7 ℃ (186.2℃ in Grzes et al. 179.6 ℃ in the model). The lower temperature values, at the friction plate, could stem from the application of convective boundary conditions with the time derivative term. The existence of the term in boundary condition equations (4.8) causes a slightly higher rate of cooling than the case without the term which can be comprehended by reviewing equation (4.8). Also, in the developed model the effect from rotation is depicted with a good resolution at points 25 mm and 23 mm such that each peak in the curve corresponds to a tour of the disk. One possible inference can be made regarding the combined complex effect of the friction heat flux to the friction plate and conductive heat flux from friction plate to the inner nodes and convective heat flux to the environment on the temperature evolution curve at 25 mm in Figure 5.1 a). Until the filling time t_{fill} = 4.3s instant, the amplitudes of oscillations are small and after that point where the velocity is still high and F_{max} is reached, amplitude of oscillations are increasing as expected. At some point after the middle of the breaking (highest level of temperatures occurs near this point) amplitudes of oscillations are decreasing at a slower rate although the friction heat flux is decreasing which could be due to the lower levels of conductive heat flux to the inner nodes that have overall high temperatures caused by the periodic friction heating.

The axial temperature distributions from a chosen z line probe for several time instants are presented in Figure 5.1 b). Comparison of axial temperature distributions also shows that the developed model resembles the results of Grzes et al. as can be seen from Figure 5.1 b).

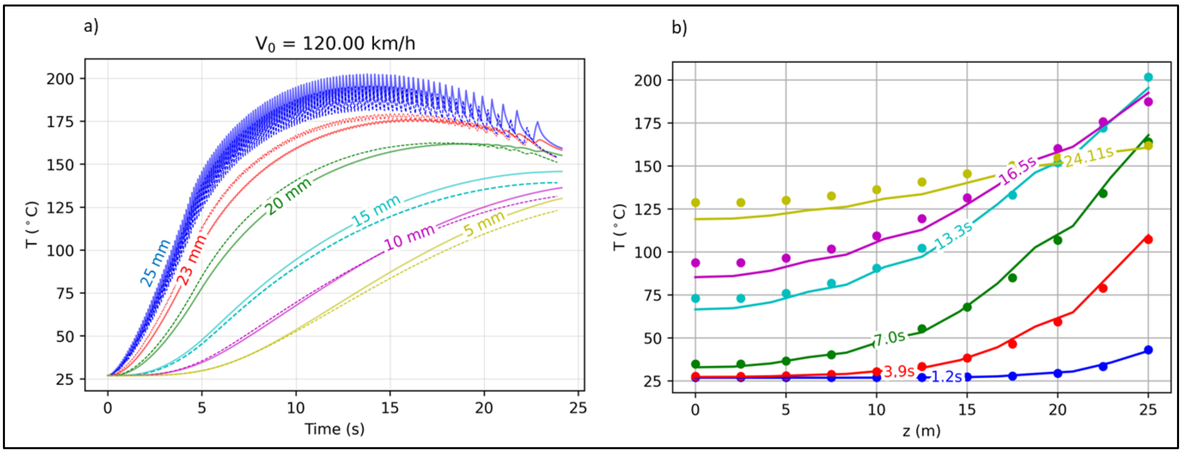

Figure 5.2. Comparison of the developed model and Simcenter STAR-CCM+

The developed model with the Simcenter STAR-CCM+ model with the initial speed of 120 km/h is shown in Figure 5.2 a) where dashed lines and show the results of Simcenter STAR-CCM+ model and b) where curves show the results of Simcenter STAR-CCM+ model. Each model includes a time-dependent convection condition on the friction plate of the disk. It can be seen from the figure that both the temperature evolutions and axial temperature distributions are in good agreement. The maximum temperature difference between the models is about 6 ℃.

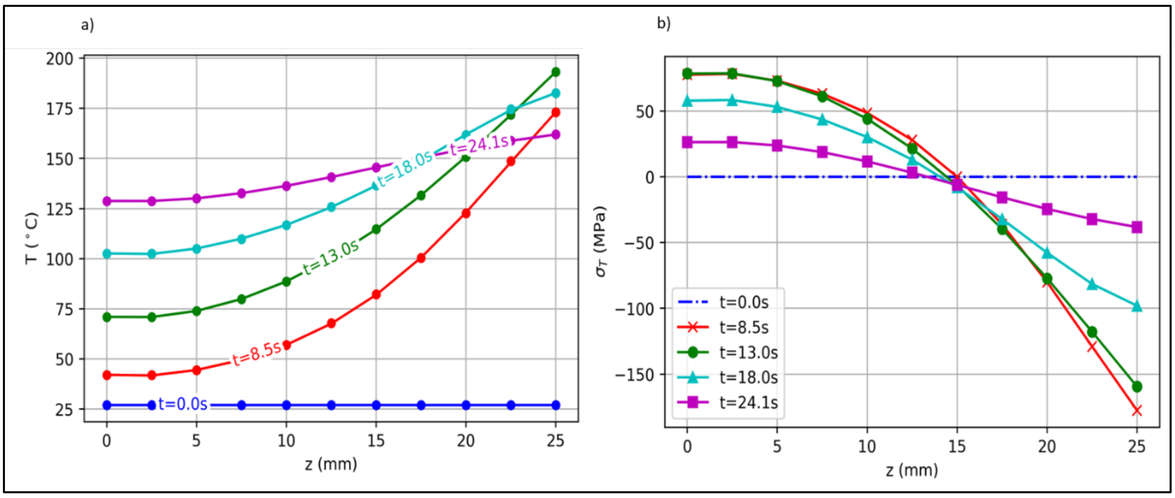

Figure 5.3. Temperature and thermal stress distributions in the Z line probe

Fitting functions (dots show the calculated results) using the results of the model and thermal stress distributions created by these functions are shown in Figure 5.3. The polynomial fitting functions are in the form of equation (5.1)

$$T_{fit}(z) = \beta_1 z^5 + \beta_2 z^4 + \beta_3 z^3 + \beta_4 z^2 + \beta_5 z + \beta_6 \qquad (5.1)$$

Coefficients for each temperature distribution in Figure 5.3 are given in Table 5.1. The degree of all polynomial fitting functions is five and created functions match the actual results- as shown with dots in Figure 5.3 a) - quite well. Time instants of axial temperatures are chosen such that thermal stress variations can be seen clearly. Figure 5.3 b) shows implicitly temperature gradients through the thickness of the disk and the resulting thermal stress distributions at several times instants during the braking. As expected, just before the braking (t = 0 s) there is no temperature variation through the thickness and therefore, the thermal stresses are zero. At the instants of 8.5 s and 13 s where the highest temperature levels and gradients occur then the maximum compressive stress levels at the friction plate and tensile stress at the inner surface are reached. And as the thermal gradient levels decrease, a proportional decrease in thermal stress levels at next time instants are observed. Thermal stress evolutions from 3 axial points are shown in Figure 5.4 and as it is seen clearly, the oscillating compression stress is more pronounced with the highest amplitude on the friction plate (z = 25 mm). At the inner surface (z = 0 mm), small amplitude and small oscillating thermal stress behavior is observable. Near the middle axial section (z = 15 mm), the lowest thermal stress levels and oscillations are observable. Tendencies and variations throughout time and space shown in Figure 5.3 b) and Figure 5.4 are in good agreement with the temperature distributions that obtained from the developed model. More importantly, obtained the thermal stress predictions in Figure 5.3 b) results in an expected behavior as reported in several studies [91,92].

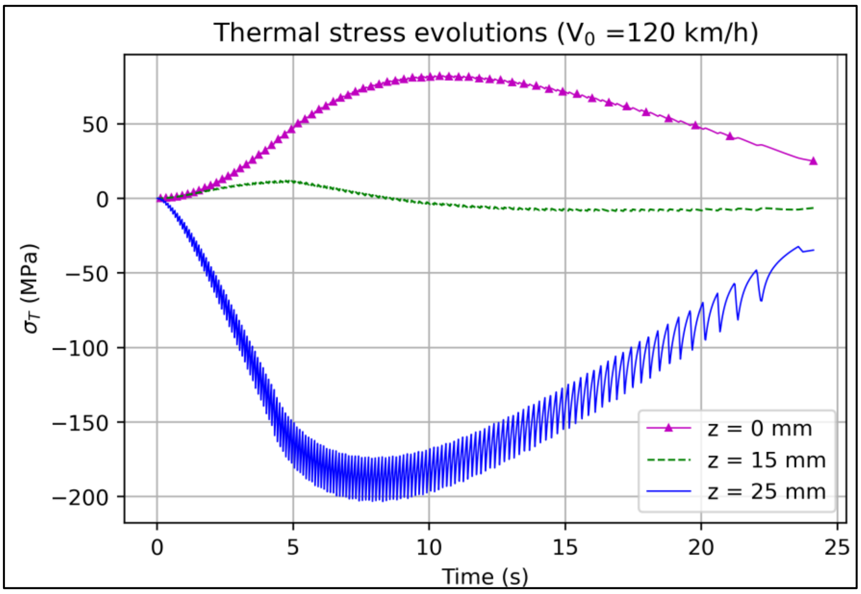

Figure 5.4. Thermal stress evolutions at several locations

The variation of thermal stress distributions with time are in agreement with the outcome of these previous studies which shows cyclic behavior of thermal stress throughout the braking process. Also, it is reported in [32,93] that, the compressive stress history evolution as shown Figure 5.4 is a significant contributing factor for the fatigue cracks in disks caused under a repeated braking condition.

Table 5.1. Coefficients of fitting polynomial functions

Time (s)	β_1	β_2	β_3	β_4	β_5	β_6
0	27	$1{,}37 \times 10^{-11}$	$-2{,}60 \times 10^{-9}$	$2{,}20 \times 10^{-7}$	$-8{,}28 \times 10^{-6}$	$1{,}16 \times 10^{4}$
8,5	42,10	-955,13	$39{,}05 \times 10^{4}$	$-2{,}87 \times 10^{7}$	$1{,}74 \times 10^{9}$	$-3{,}29 \times 10^{10}$
13	70,99	-702,50	$28{,}14 \times 10^{4}$	$-5{,}98 \times 10^{6}$	$3{,}27 \times 10^{8}$	$-7{,}23 \times 10^{9}$
18	102,62	-863,15	$35{,}02 \times 10^{4}$	$-2{,}09 \times 10^{7}$	$1{,}09 \times 10^{9}$	$-2{,}25 \times 10^{10}$
24,1	128,78	-266,70	$10{,}21 \times 10^{4}$	$1{,}77 \times 10^{6}$	$-2{,}08 \times 10^{8}$	$3{,}03 \times 10^{9}$

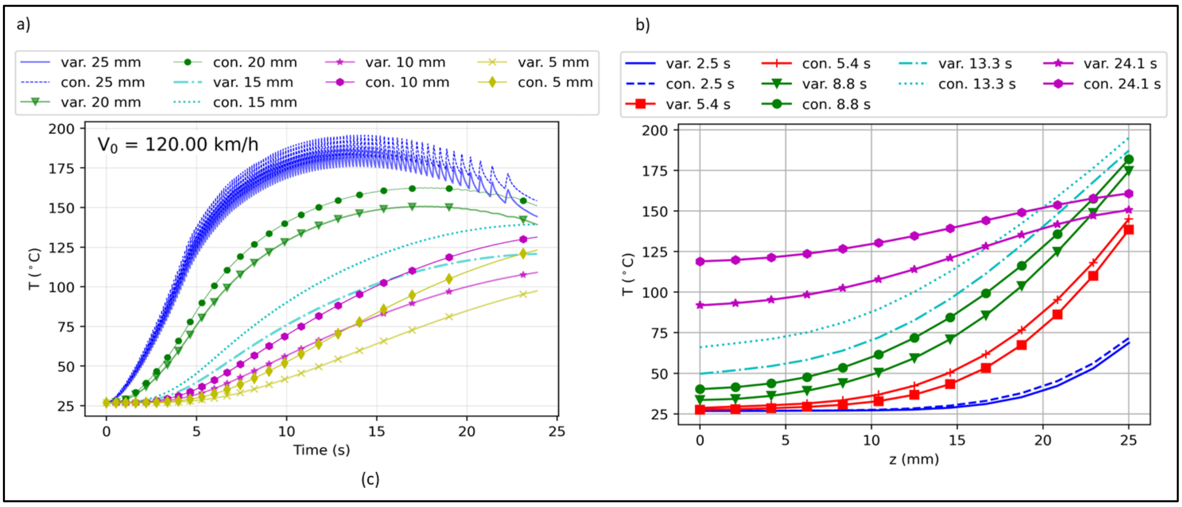

Figure 5.5. Comparison of the Simcenter STAR-CCM+ models

Investigation of the effect of thermal property variation on the temperature and thermal stress distribution is conducted by enhancing the existing Simcenter STAR-CCM+ model with variable thermal properties. The simulated case is the braking from an initial speed of 120 km/h until it stops. The same approach in presenting outcomes is also adopted here, and results are given in Figure 5.5. In these figures, var. means result of the variable thermal property model and con. means the result of constant thermal model. Temperature evolutions show that differences between the models vary in direct proportion with the temperature of the disk. This behavior is mainly driven by the specific heat increase with temperature increase. However, this difference is somewhat lower on the friction plate when compared to other points, as seen in Figure 5.5 a). One possible explanation could be that; at this surface friction heat flux has its direct effect on the temperature levels whereas the heat transfer at the inner locations is being driven only by conduction mechanism and therefore, less temperature differences between the models at the friction plate are observed. Similar thermal behavior at the friction plate side is also observed when the axial temperature distributions at several time instants are examined in Figure 5.5 b). The most significant difference between both models arises at the end of braking, where the average temperature values reach their maximum value. One other conclusion can be made that the effect of thermal conductivity is limited when compared to the effect of specific heat because gradients of axial temperature distributions do not differ significantly, whereas the sharp effect of conductivity would yield easily distinguishable higher gradients in the model with variable properties. This may be explained by the fact that the change in the thermal conductivity of the material is lower when compared to the change in the specific heat within the given temperature range (20-400 ℃), as seen in Table 4.2. Comparison of thermal stress distributions of two models shown in Figure 5.5 could suggest that the inclusion of variable thermal properties in calculations has no significant effect on predicting thermal stress distributions.

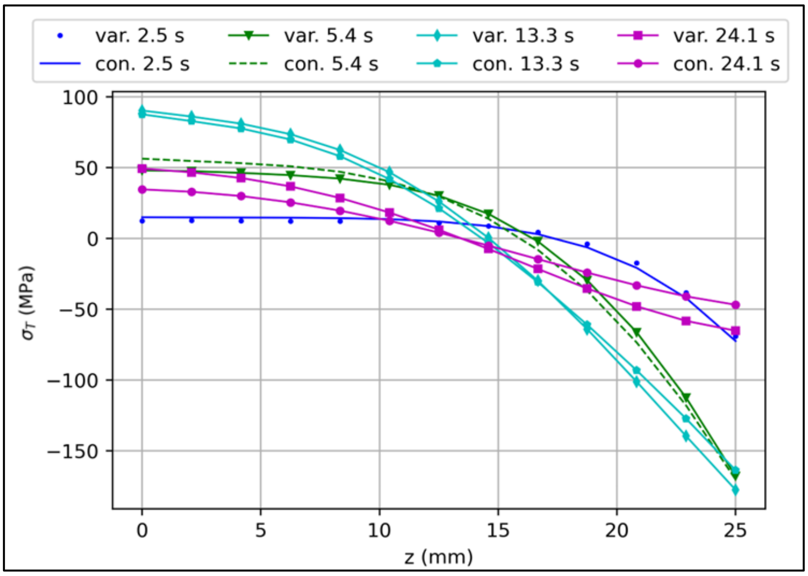

Figure 5.6. Comparison of thermal stress distributions

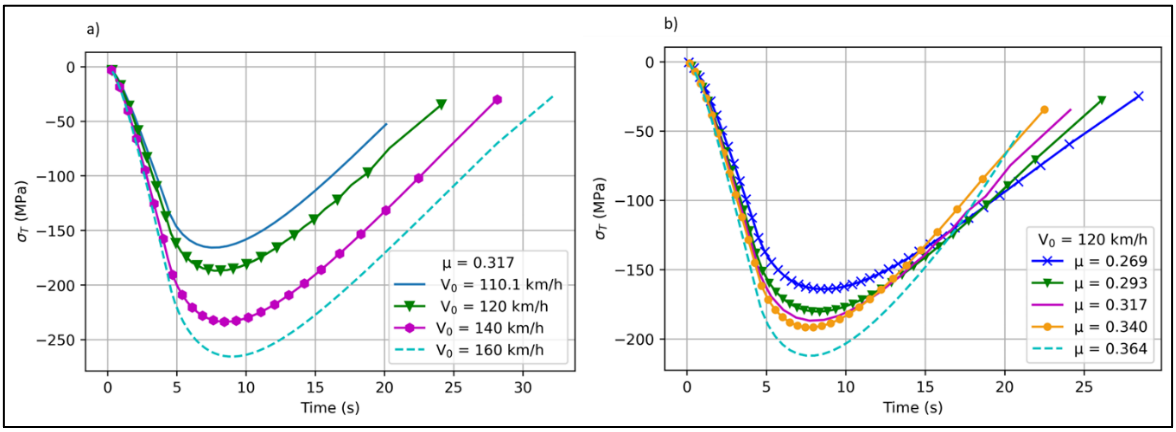

Figure 5.7. Simulation results of the developed model for test cases

Several test cases are setup using the developed model to show the applicability of the developed model for the thermal stress predictions under various braking scenarios. First test case is comparison of the thermal stress predictions using the developed model with the initial speeds of 110.1, 120 ,140 and 160 km/h (with constant HTCs). Friction coefficient is taken as 0.317 as it is the base value in the experimental study by Grzes et al. Results of this case as shown in Figure 5.7 a). Compressive thermal stress evolutions for all initial speeds are shown as time-averaged values to clearly compare the curves. The results suggest that velocity has a main effect and on the thermal stress behavior that is an increase in the kinetic energy to be dissipated with increasing velocity resulting in higher temperature levels and higher gradients. This in the end effect maximum thermal stress levels proportionately. There is almost 100 MPa maximum thermal stress difference between the initial velocities of 110.1 and 160 km/h case.

Friction coefficient can vary around some average value depending on the conditions such as materials and environment for a given friction couple. It is also the case in the railway brake disk system and generally the friction coefficient can vary in the range of ± 15% as it is stated in an analytical-experimental study on the friction coefficient of a railway brake disk brake. Therefore, another considered test case in the current study is the effect of friction coefficient change on the brake disk thermal behavior. In addition to the already obtained results from the case of initial velocity 120 km/h with 0.317 friction coefficient, the developed model is simulated with friction coefficients. These values correspond to 15% change from the base value of 0.317 and the resulting time-averaged thermal stresses are shown in Figure 5.7 b). In the figure, it can be seen that the changes caused by ± 7.5% change in friction coefficient has minor effect whereas change caused by ± 15% has more pronounced effect on maximum thermal stress levels. Difference between thermal stress levels of 0.317 and 0.364 case is around 30 MPa. It can be roughly estimated that the disk under consideration with the given conditions in this study has a possibility to experience quite high thermal stress levels in the case of 160 km/h – 0.364 friction coefficient which needs to be taken into account together with the yield strength of the disk material in the initial designing or selection process.

An additional comparison is made to investigate the effect of time-dependent convection on the friction plate of the disk for the initial speeds of 110.1 and 120 km/h. There has been about 2% difference between the developed model with and without time-dependent convection when overall temperatures in the disk are compared. The model with time-dependent convection has yielded overall higher temperature values as expected. Differences in thermal stress distributions are also found to be negligible, and hence graphical results for comparison are not presented. These insignificant differences could be explained by the use of mean Nu numbers that is obtained from almost uniformly heated convective disk experiments. However, contour plots (scalar scene in Star-CCM+) of temperature distributions from the model with variable HTCs obtained via a post-processing library in Python are shown in the following.

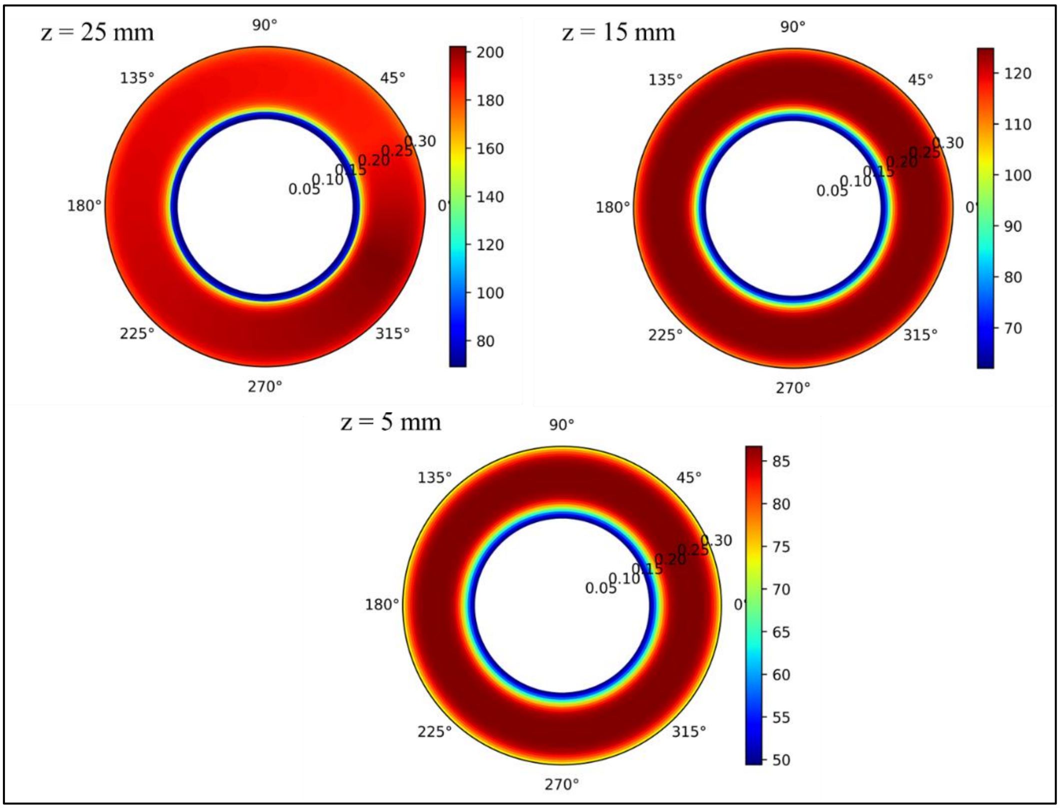

Figure 5.8. Contour plots from 13.3 s of 120 km/h braking case

Firstly, contour plots of temperature are shown in Figure 5.8 from three axial plane. The axial plane at z = 25mm is the friction plate and z = 15 and 5 mm is the inner axial planes. Following contour plots also have the same three axial plane. The plots are taken from braking with an initial speed of 120 km/h at 13.3 seconds, when the friction plate has the highest temperature levels. The plot from z = 25 mm has non-uniform temperature distribution reflected by i) rotation of pad ii) varying HTC over the radius (dependent on the rotational Reynolds number), iii) circumferential HTC in inner and outer radial sections. Figure 5.9 shows contour plots of temperature et the end of braking from the initial speed of 120 km/h. In the figure effect of lower levels of heat flux and less non-uniform (compared to the 13.3 s plot) temperature distribution can be observed.

The highest simulated braking case with initial speed of 160 km/h is shown in Figure 5.10 and 5.11 (maximum temperature levels and the end of braking, respectively). The effect of higher heat flux reflects more uniform temperature levels in friction plate in Figure 5.10.

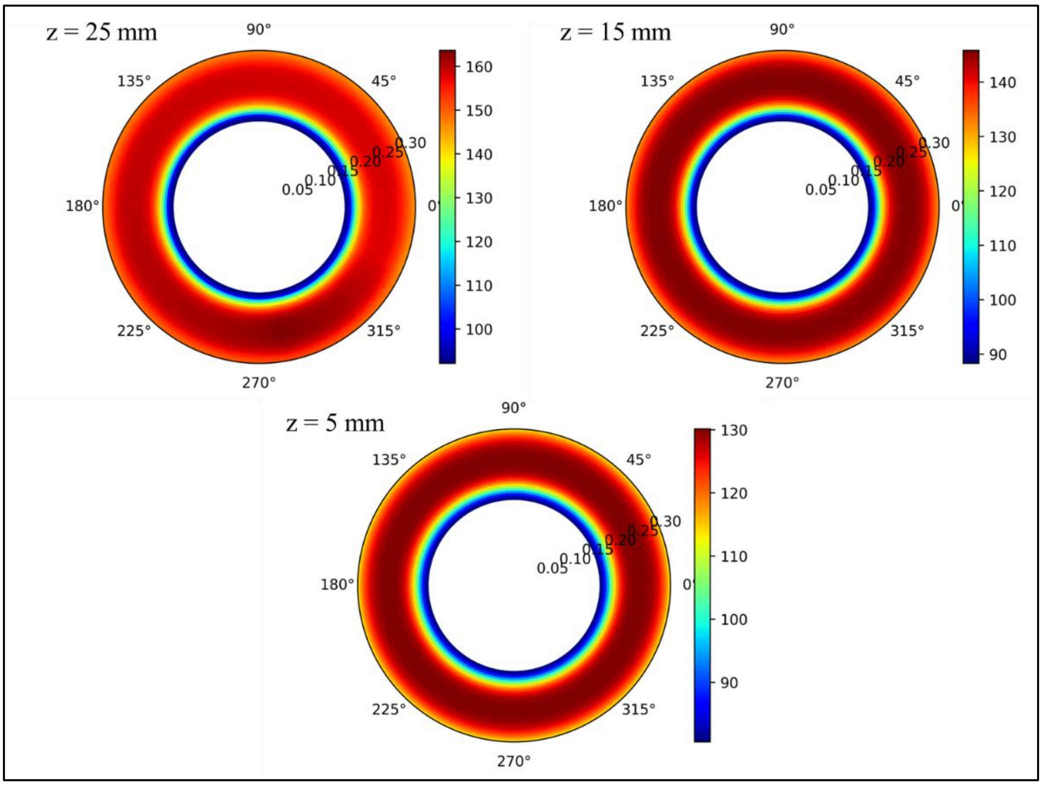

Figure 5.9. Contour plots from the end of 120 km/h braking case

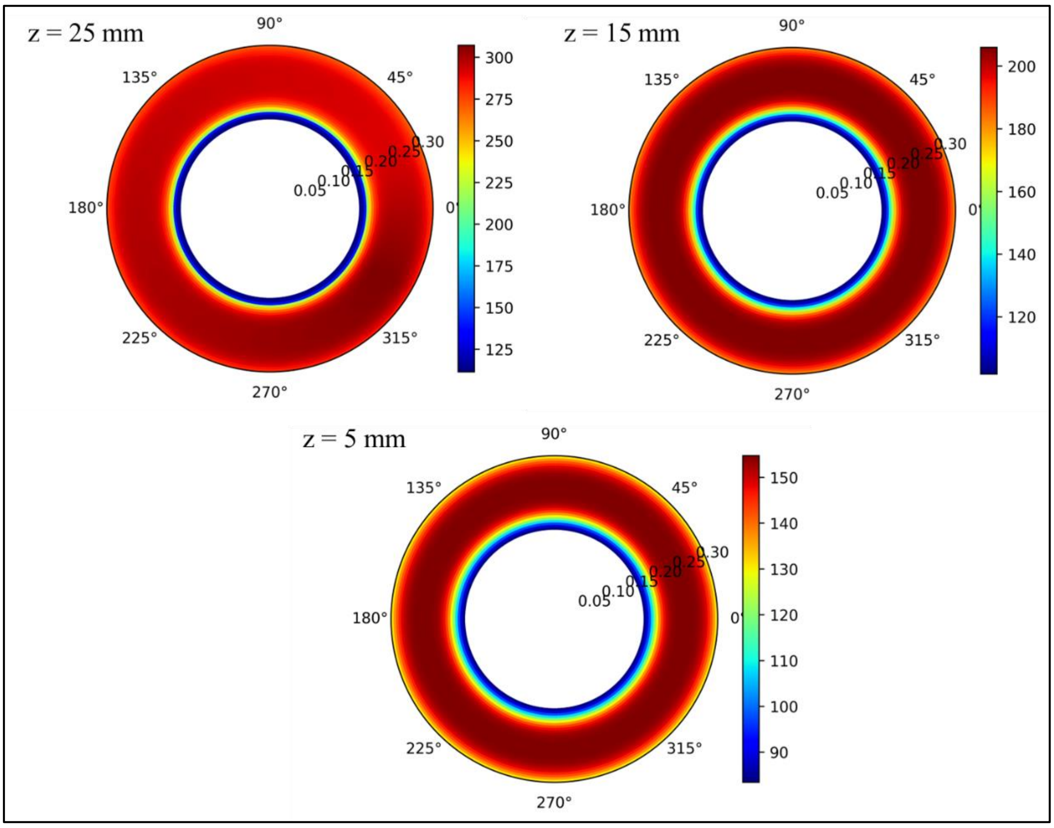

Figure 5.10. Contour plots from 17.8 s of 160 km/h braking case

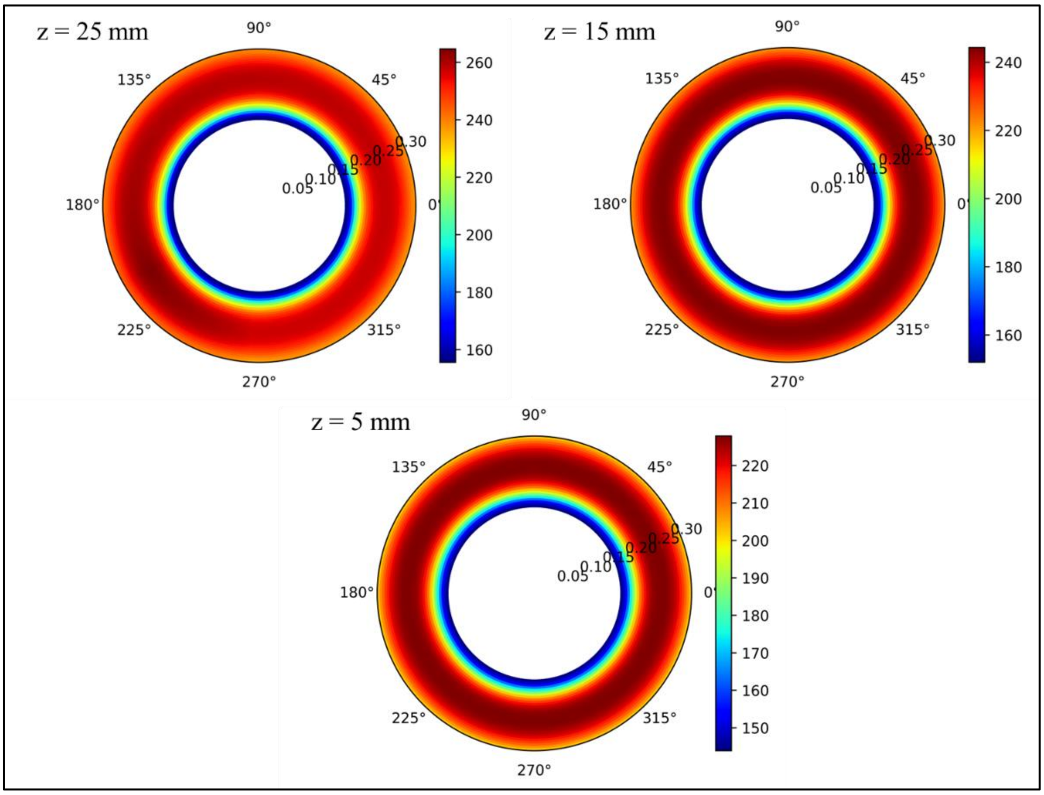

Figure 5.11. Contour plots from the end of 160 km/h braking case

A comparison of CPU times was also performed between the developed model and the Simcenter STAR-CCM+ model. A significant difference was observed between the CPU times of the developed model and the Simcenter STAR-CCM+ model (see Table 5.2). Considering the braking conditions with initial speeds of 110.1 km/h and 120 km/h, the developed model is on average 94.5 times faster than the Simcenter STAR-CCM+ model. Simulations are carried out on the same computer with 32 GB RAM and processor Intel(R) Core (TM) i7-4930K CPU @ 3.40GHz.

Table 5.2. Comparison of CPU times of models

Velocity (km/h)	The developed model (Python)	Simcenter STAR-CCM+
110.1	294 (s)	25,599 (s)
120	348 (s)	35,660 (s)

6. EXPERIMENTAL ANALYSIS ON FREE ROTATING DISK

Aim of this experimental study is to investigate and show the applicability of a novel experimental approach on a heated rotating disk for several rotational speeds. Then, experimental results will be used for the validation of the CFD model of free rotating disk. The investigations include the effect of the perturbation parameter on the onset of instability of the flow over a rotating disk. To have a non-invasive measurement system, the experimental setup does not include thermocouple and HWA. Transient temperature data with the help of an in-house developed Python code is performed to reconstruct the precise transient temperature distributions over the radius of the disk. The directly measured transient temperature distributions are used for calculation of the Nusselt number distributions for a range rotational speed and range of perturbation parameters. Details of the experimental method will be given in the following sections.

6.1. Test Rig

A test rig of heated rotating disk combined with a suitable IR camera can provide specific data from which a remarkable insight can be obtained on convective heat transfer. Particularly, local Nusselt number and its dependence on local rotational Reynolds number can be determined through the transient thermal behavior of the disk. Therefore, a specially designed test rig is employed in this investigation. The test rig in the study has already been used in several studies [63,69,94,95] on convective heat transfer over a rotating disk subjected to forced flow and the reader is referred particularly to the article [94] for a detailed explanation of the test rig. However, in those studies, the test rig was used for determination and analysis of mean Nu numbers under different flow configurations. In the current study, IR camera is utilized to evaluate the transient temperature distribution of the disk surface which is being heated through constant heat flux and hence having a sufficiently uniform temperature distribution. Therefore, the test rig is appropriate for the aim of determination of local Nu numbers with a lumped capacitance approach and the suitability of the approach will be explained in the next section.

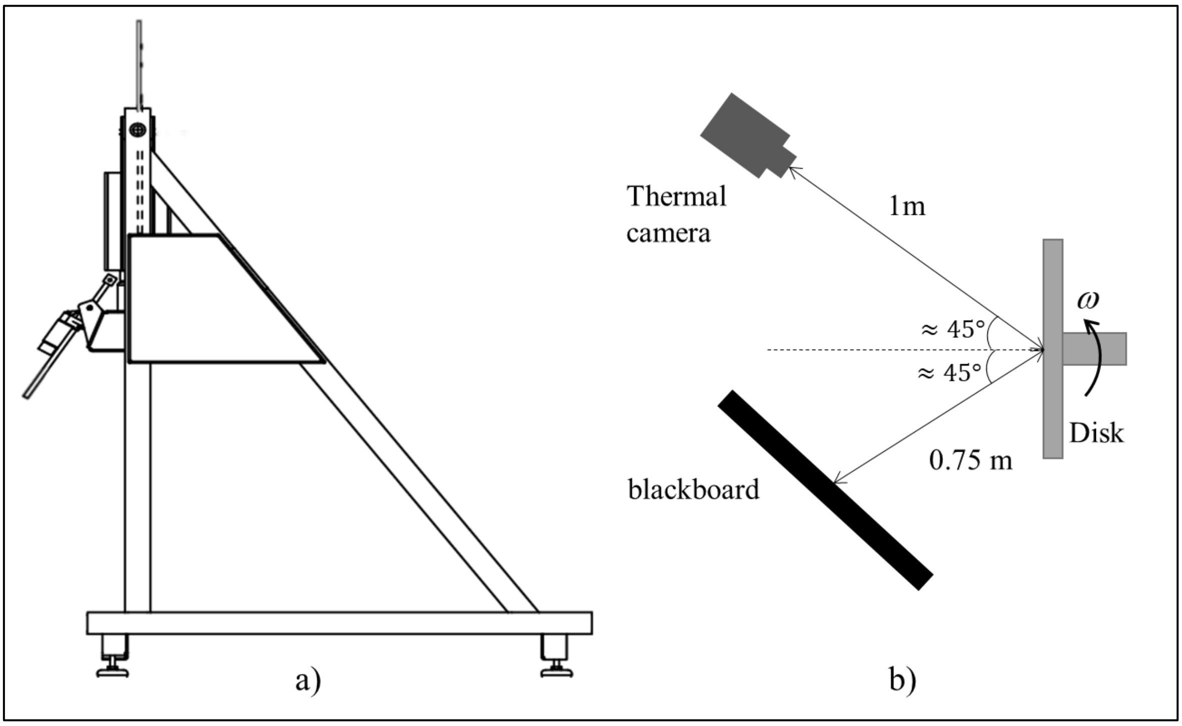

Figure 6.1. Construction of the measurement system and thermal camera

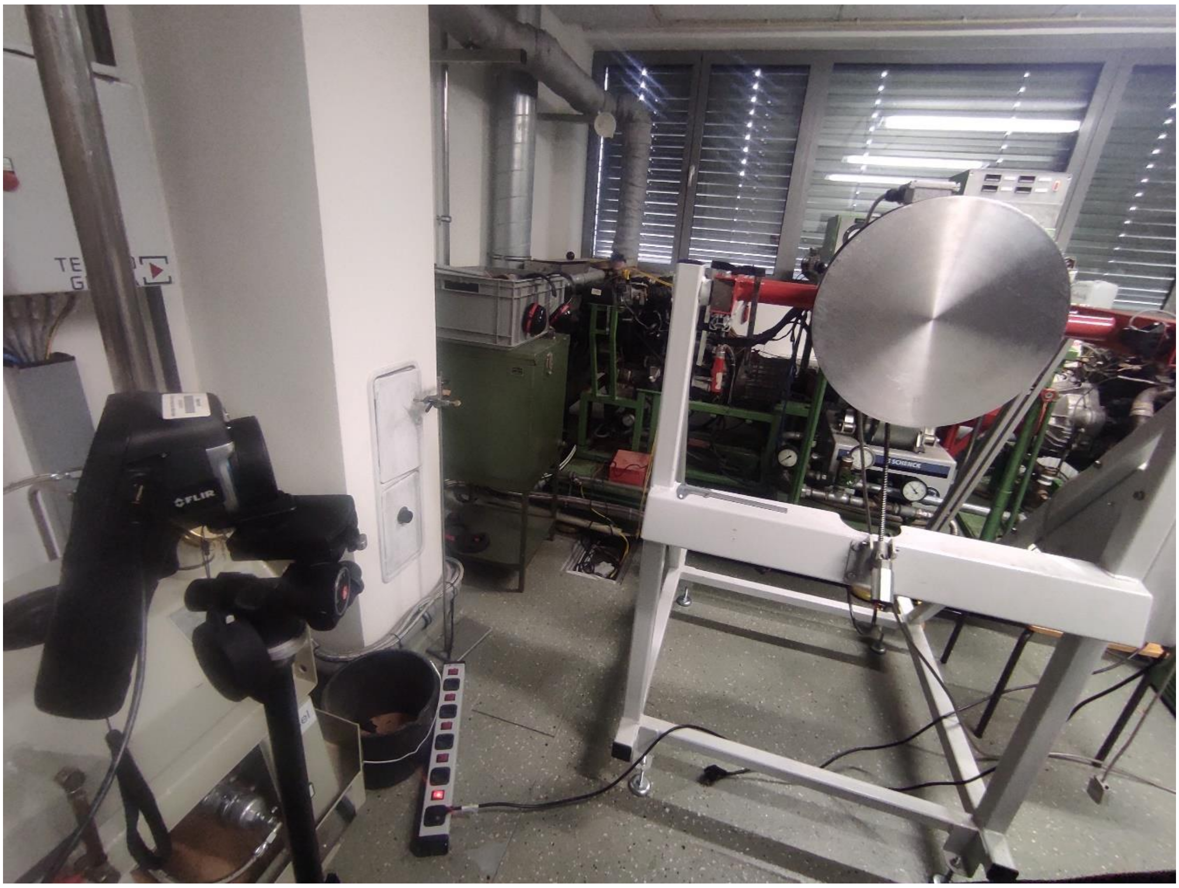

Figure 6.2. Heated rotating disk system with the thermal camera

Test rig is shown in Figure 6.1 and Figure 6.2, it consists of an electrically heated composite disk of radius R = 200 mm and total thickness of it is 55 mm (in Figure 6.3). The disk is connected to a shaft driven by an electric motor. The composite disk comprises of multiple layers joined to a 2 mm heating pad.

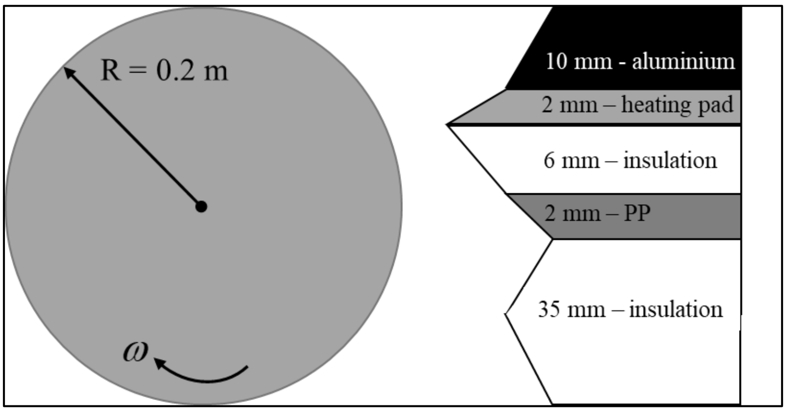

Figure 6.3. Construction of the heated disk

The surface of the aluminum disk is polished, and it has low emissivity. There were other shiny metallic components in the room. Regarding these facts, the thermal camera with a blackboard is used in dark room to reduce reflection effects and to have a minimum noisy temperature data from the surface of disk.

FLIR IR camera is used with the ResearchIR software whose functions is thermographic data acquisition and analysis designed for the R&D investigations. The software supports FLIR R&D cameras and provides an environment for factory and user calibrations [96]. Properties of the thermal camera FLIR E60 used in the study is given in Table 6.1.

Table 6.1. Properties of the thermal camera FLIR E60

Property	Value/range
Frequency	30 Hz
IR resolution	320 × 240 pixels
Thermal sensitivity	< 0,05°C @ +30°C / 50 mK
Spatial resolution (IFOV)	≈1,3 mm
Object temperature range	–20°C to +120°C
Property	Value/range
Frequency	30 Hz

The experiments are conducted with different duration times. This has been done to check the dependence of the test setup and the evaluation method on the test duration. After several test evaluations it has been found out that the method is applicable in the range 60-180 s which is a good compromise between accuracy and measurement time.

Sample raw thermal images in ResearchIR software from an experiment (no. 6 in Table 6.3) is given in Appendix-2. The raw thermal image of the heated disk in Figure 2.1 in Appendix-2 shows the temperature distribution just before the start of motor. The disk in this figure has a uniform temperature distribution around 40.3 ºC. Then, Figure 2.2 in Appendix-2 shows the raw thermal image after the motor has stopped.

6.2. Calculation of the Heat Transfer Coefficient

Heat transfer coefficients are calculated by the lumped capacitance approach. To use the approach, the condition $Bi = \left(\frac{hL}{k}\right) < 0.1$ must be satisfied. Another condition is that the cooling solid should have a sufficiently uniform temperature distribution [97]. The Biot number for the highest rotational speed is between 0.0012 - 0.0036 where the range of heat the transfer coefficient from previous theoretical/experimental correlations is lying between 30-90 W/m^{2}K for the given range of Reynolds number in this study. Initially, the disk has an isothermal temperature distribution just before the rotation starts and the constant heat flux to the disk from the back side provides a sufficiently uniform temperature distribution within the disk so that the second condition for the lumped capacitance approach is also satisfied.

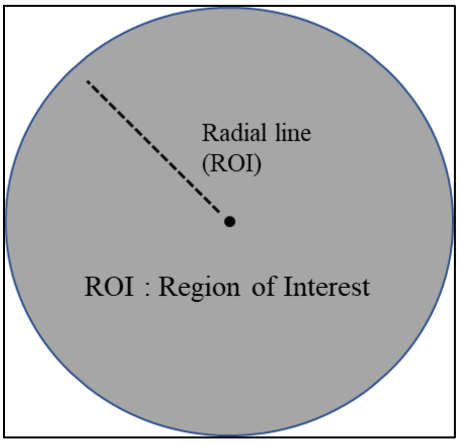

Figure 6.4. Schematic presentation of the radial line in ResearchIR software

ResearchIR software from the FLIR company allows the user to create ROI's (Region of Interest) on the measured object. A ROI provides the temperature distribution of a chosen section to be saved in a datasheet for only one time instant. A radial line is created in ResearchIR to determine the dependency of local Nusselt number on the local rotational Reynolds number, see Figure 6.4 for presentation of a ROI (radial line). The radial line is drawn slightly away from the geometric center of the disk surface towards the end edge of the disk. Thermo-optical interaction of the IR Camera with the shiny surface of the disk creates a bit unrealistically higher temperature just at the center of the disk despite a particular effort on avoiding the reflection effects in measurement room. Therefore, the start point of the radial line (Radius start in Table 6.3) is placed slightly away from the center of the disk. In addition, convection effects from the circumferential surface are avoided by placing the endpoint of the radial line (Radius end in Table 6.3) 9 mm away on average from the disk edge. The radial line consists of several pixels from each of which the transient temperature data are obtained by saving the measurement data to the PC. The online measurement mode in ResearchIR is activated while performing the measurements.

Thermal image is constructed through square-shaped pixels. A pixel has an extension in the axial direction that has the thickness of disk. Any radial line can in principle be said to consist of adjacent rectangular prisms. Accordingly, geometries of rectangular prisms that constitute a radial line will be used in the lumped capacitance approach. Schematic view of the lumped analysis is shown in Figure 6.5.

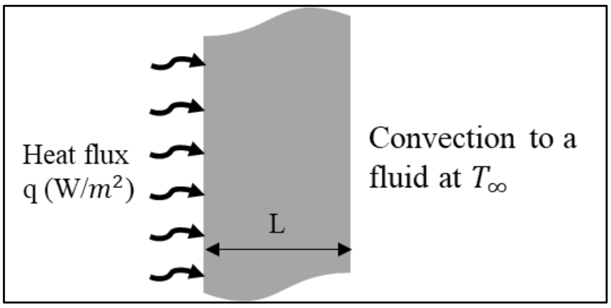

Figure 6.5. Schematic view of the lumped analysis of transient heat transfer [97]

Equation that gives the transient thermal behavior of a rectangular prisms (pixel) is given as [97]

$$A_{pix}q - A_{pix}h\left(T - T_\infty\right) = \rho c A_{pix} L_{pix} \frac{\partial T}{\partial t}$$

or (6.1)

$$q - h\left(T - T_\infty\right) = \rho c L_{pix} \frac{\partial T}{\partial t} \text{ for t>0}$$

with the initial condition $T\left(t=0\right) = T_0$. A variable Θ is defined for a convenience in the solution of the ordinary differential equation such that $\Theta\left(t\right) = T\left(t\right) - T_\infty$. Using Θ and the initial condition, equation becomes

$$\frac{d\Theta}{dt} + m_{lump}\Theta = Q_{lump} \text{ for t>0} \quad (6.2)$$

Variables in equation (6.2),

$$\Theta_0 = T_0 - T_\infty$$

$$m_{lump} = \frac{h}{\rho c L_{pix}} \text{ and } Q_{lump} = \frac{q}{\rho c L_{pix}} \quad (6.3)$$

The solution of the ordinary differential equation results in

$$\Theta = \Theta_0 e^{-m_{lump} t} + \frac{q}{h} - \frac{q}{h} e^{-m_{lump} t} \quad (6.4)$$

Equation (6.4) gives the temperature value of a pixel after the thermophysical, geometrical parameters and time instant are substituted into it. The equation is manipulated such that the heat transfer coefficient becomes an only unknown parameter.

$$h\Theta - h\Theta_0 \, e^{-m^*_{lump} h} - q + q\, e^{-m^*_{lump} h} = 0 \tag{6.5}$$

where,

$$m^*_{lump} = \frac{t}{\rho \, c_p \, L_{pix}} \tag{6.6}$$

The determination of heat transfer coefficient of each pixel is reduced to the problem of finding the real root of the equation (6.5). After heat transfer coefficients are determined, the Nusselt number is calculated for each pixel by substituting the local radius of each pixel in the equation (6.6).

$$Nu = \frac{h\, r}{k_{air}} \tag{6.7}$$

6.3. Uncertainty Analysis

Heat losses are calculated by means of electrical resistance. Thermal conductivity data from manufacturers are used for calculations together with the geometry of each component, see Figure 6.3. Heat losses (to the back side) are found to be less than 1% thanks to reliable insulation materials. A calculation according to the law of error propagation is done for Reynolds and Nusselt numbers. Relative errors for properties used in this study are given in Table 6.2. Thermophysical parameters are thermal conductivity and kinematic viscosity of air and thermal conductivity of the disk. For the Prandtl number the relative error is assumed as 0.25% given in the study [22].

Table 6.2. Relative errors for measured and calculated properties

Property	Relative error (%)
Temperature	1,66
Thermophysical parameters	1,00
Local radius (ResearchIR)	0,76
Rotational speed	0,50
Reynolds number	1,72
Heat transfer coefficient	1,79
Nusselt number	2,16

6.4. The film temperature and Property-Ratio Method

The temperature-dependent thermophysical properties of the fluids should be taken under consideration very carefully [22]. There are two methods mainly used for this kind of analyses namely arithmetic mean temperature of thermal boundary layer (film temperature) and property-ratio method. The film temperature method is calculated as

$$T_f = \frac{T_w + T_\infty}{2} \tag{6.8}$$

But this method may lead to unfavorable results when there are elevated temperature differences between wall and fluid temperature. To account for this problem, the property-ratio method is developed for the evaluation of skin friction coefficient and Nusselt number for the case of external flow over surfaces [48]. In the method, heat and momentum transfer are obtained through fluid properties depending on the ambient temperature and pressure of the undisturbed free-stream multiplied by a correction factor. The formulation for the evaluation of Nusselt number for air with Pr = 0.71 is given in the following

$$\frac{Nu}{Nu_{c.p.}} = \left(\frac{\rho_w \eta_w}{\rho_\infty \eta_\infty}\right)^{0.2493} \left(\frac{\Pr_w}{\Pr_\infty}\right)^{-0.397} \left(\frac{c_{p,w}}{c_{p,\infty}}\right)^{0.5} \tag{6.9}$$

Although it is stated that for air, the use of film temperature method is sufficient, both methods are used for a comparison of them in the context of the current study.

Furthermore, there are several temperature ranges in the experimental configuration, therefore, Sutherland's law [98] is used for the calculation of kinematic viscosity and the thermal conductivity of air for any given ambient, wall and film temperature.

$$\nu = \nu_{ref} \left(\frac{T}{T_{ref}} \right)^{3/2} \frac{T_{ref} + S}{T + S} \tag{6.10}$$

$$k = k_{ref} \left(\frac{T}{T_{ref}} \right)^{3/2} \frac{T_{ref} + S}{T + S_k} \tag{6.11}$$

6.5. Results of Experimental Study

Details of parameters for each experiment are given in Table 6.3. Range of different rotational speed and perturbation parameter is considered to study the effects of heating on the stability of the flow over a rotating disk. Aim of the first experiment is to analyze the laminar flow over the disk. The Reynolds number is chosen such that there is only a laminar boundary layer existing over the whole radius of the disk. Other experiments are performed at higher Reynolds numbers resulting in laminar, transitional and turbulent regime coexisting over the radius of the disk. Radius start and end parameters is explained in the section 6.2.

Table 6.3. Experimental parameters

No	Re_ω	ω (rad/s)	Radius start (m)	Radius end (m)	$T_{w,0}$ (ºC)	T_∞ (ºC)	ε	Duration (s)
1	83908	34,55	0,005	0,194	52,1	22,2	0,1012	100
2	292666	125,66	0,010	0,190	50,8	21,2	0,1006	180
3	295755	125,66	0,010	0,191	54,5	22,4	0,1086	180
4	315191	138,22	0,007	0,188	55,1	22,5	0,1103	120
5	325330	138,22	0,013	0,191	57,5	23,1	0,1161	120
6	373575	157,07	0,008	0,192	40,3	23,1	0,0581	100
7	369694	157,07	0,013	0,191	47,4	23,4	0,0820	95

The outcomes of the experiment are compared with those obtained from early investigation by de Vere [20] and somewhat recent investigation by Pelle&Harmand [53]. In the following, local Nusselt correlation for laminar part of the flow (low Reynolds number) as given in equation (3.77) is shown in graphical presentation of the results. These laminar curves are represented with local Reynolds number that are calculated by radial distance of each pixel in the radial line.

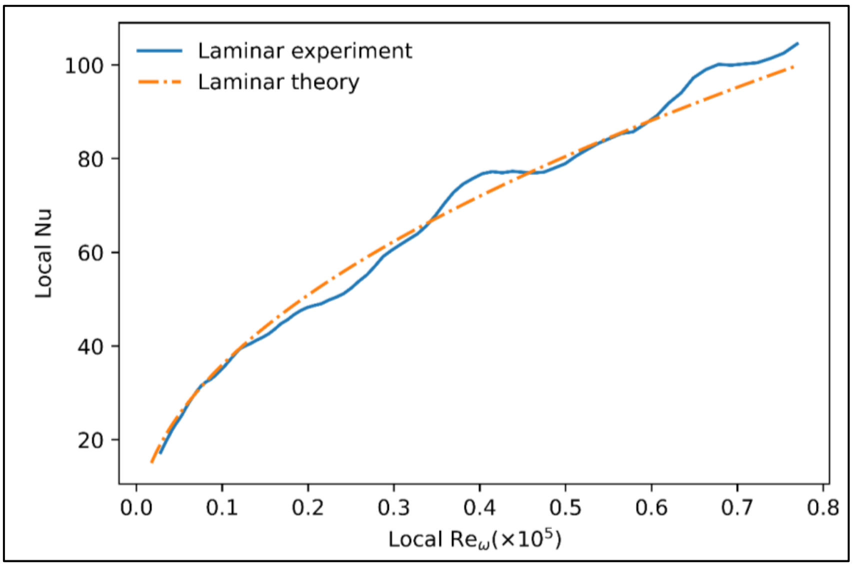

Figure 6.6. Laminar local Nu distribution with respect to local Re_ω

The result of the experiment at a rotational speed of 34.55 rad/s, with the laminar boundary layer covering the whole of the disk radius, is shown in Figure 6.6. The local Nusselt number dependence on local Reynolds agrees well with the theoretical/experimental correlation. The coefficient of equation (3.77) here is taken as $K = 0.36$. This value was also found to be more suitable in a relatively late study in this research area [42].

Figure 6.7 shows three plots with three different rotational speeds, each plot has two experimental graphs with different perturbation parameter and results of two previous studies with corresponding theoretical laminar Nusselt number distribution. The experiments with the highest rotational speed of 157.07 rad/s are shown in Figure 6.7 (top left). Both experimental curves show a similar trend to the local Nusselt number dependence at other velocities. They also correlate well with the corresponding theoretical laminar curve.

Graphs for the rotational speed of 125.66 rad/s are shown in Figure 6.7 (top right), results of both experiments fall in the range that is between the de Vere [20] and Pelle&Harmand [53]. However, both experiments up to about $Re_\omega = 9 \times 10^4$ correlate better with the theoretical laminar curve than the de Vere and Pelle&Harmand. It is stated in de Vere's paper that laminar part of the rotational flow field correlates well with the study [19] that concluded the K value in equation (3.77) as 0.38. On the basis of this, the laminar part of de Vere's curve follow tends to be somewhat higher.

The Figure 6.7 (bottom) shows the experimental results having 138.22 rad/s rotational speed. In this figure, it can also be said that the experimental curves are in good agreement with de Vere and again fall within the range of both previous studies. There is also a rather early deviation from laminar behavior, which can be attributed to the fact that it has the highest perturbation parameter among the others.

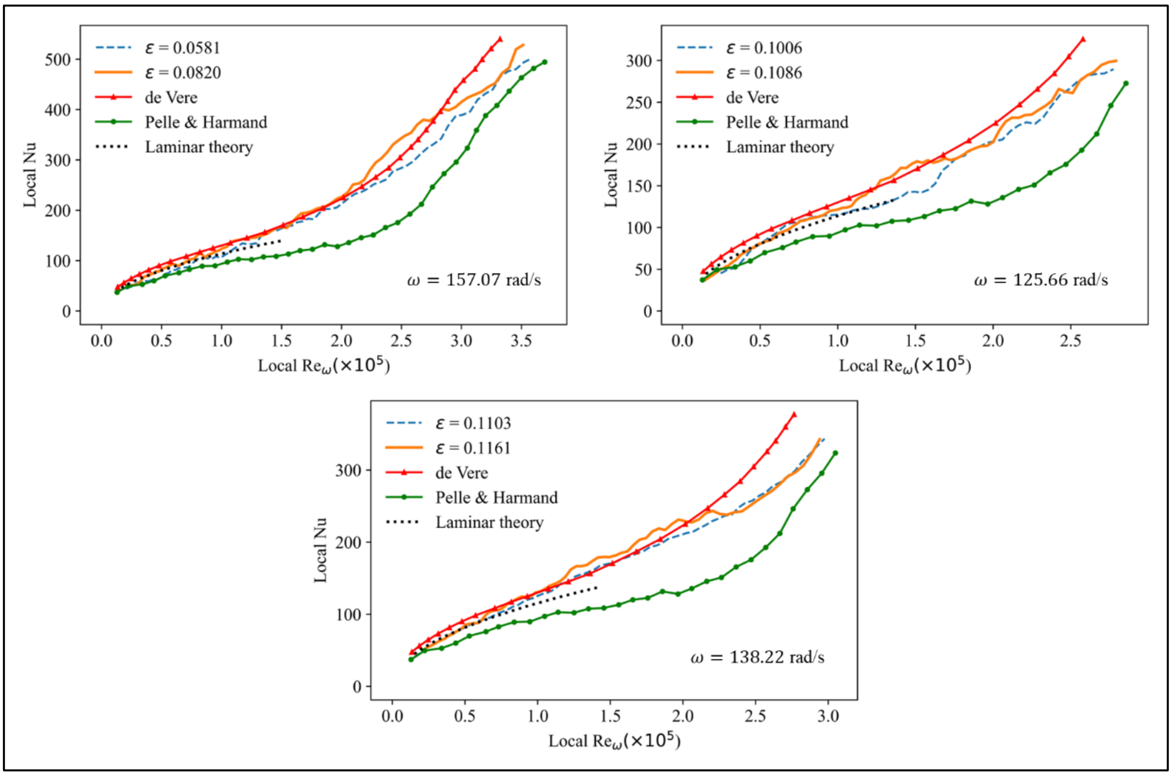

Figure 6.7. Local Nusselt distribution with respect to local Re_ω

An important observation about the experimental curves at any given rotational speed is that those with greater perturbation parameter result in slightly higher local Nusselt numbers. This is particularly visible after $Re_\omega = 10^5$ for rotational speeds of 125.66 rad/s and 138.22 rad/s. For the rotational speed of 157.07 rad/s, the curve with a perturbation parameter of 0.0820 tends to be higher than the 0.0581 curve after about $Re_\omega = 1.5 \times 10^5$. And in general, all experiments follow a pattern closer to de Vere than to Pelle&Harmand.

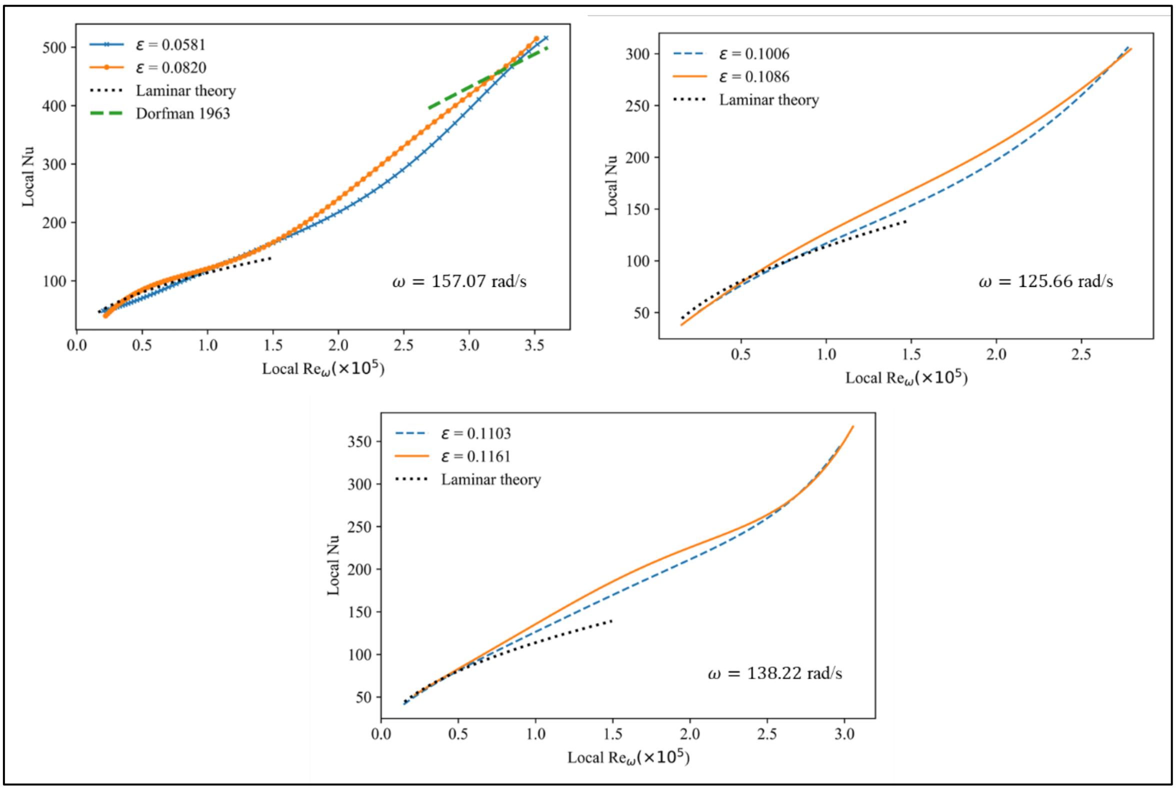

Figure 6.8. Fitted local Nusselt distribution with respect to local Re_{ω}

The fifth-degree polynomial functions from the local Nusselt distributions are generated in Python by utilizing polyfit function that employs the least square method to fit the measured values. The local Nusselt distribution and the local Reynolds number of each experiment are used as input parameters to the Python function.

Fitted local Nusselt distribution results are compared to each other together with the corresponding laminar flow as shown in Figure 6.8. It can be again observed that the increase in perturbation parameter results in an early instability. All three rotational speed show the same pattern when looking at the Figure 6.8 that an increase in the perturbation parameter results in an early departure from the laminar behavior at a given rotational speed. Another observation is that although the difference in the perturbation parameter is higher between $\varepsilon = 0.0581$ and $\varepsilon = 0.0820$ for the case of 157.07 rad/s than in the others, there is no stronger-earlier deviation from laminar behavior as expected. This may indicate that the early departure from stability at a given speed is not proportionally affected by variations in the perturbation parameters. An alternative explanation could be that the effect of perturbation parameter may only be pronounced after a certain-higher levels of the parameter.

Research has mainly focused not on the turbulent part of the flow, but rather on the laminar part and the onset of instability. Nevertheless, for the case of 157.07 rad/s it was realized that the after about $Re_\omega = 2.75 \times 10^5$ the tendency of the local Nusselt number follows the correlation given by Dorfman [60] for the turbulent regime of convective flow over a rotating disk, see Figure 6.7 (top left). Other rotational speeds are also compared but they do not follow the Dorfman relation as the case of 157.07 rad/s, they are somewhat below that curve. This is not surprising as the turbulence starts after at least at $Re_\omega = 2.65 \times 10^5$ and on average $Re_\omega = 3.1 \times 10^5$ according to a quite detailed review of Re_ω for the end of transition as given in Shevchuk's book [62].

The final remark on the experimental results is that the evaluation of the local Nusselt number using the property ratio method makes almost no difference compared to the film temperature method, as expected for the fluid air. Therefore, the results evaluated by the property-ratio method have not been presented.

7. CFD MODELING AND SIMULATION

In this chapter, two related CFD models that are built for the simulation of heated free rotating disk and the brake disk with complex geometry will be explained. The main properties of the CFD models are that they are

- three-dimensional,
- unsteady,
- includes transition and turbulence modeling (only for free rotating disk) and
- simulate the conjugate heat transfer.

Firstly, the CFD model of heated free rotating disk will be presented and then the CFD model of the brake disk with the complex geometry will be presented.

7.1. The CFD Model of Heated Free Rotating Disk

The capability of conjugate heat transfer modelling with rotating walls in Simcenter Star-CCM+ is used for the modelling of conjugate heat transfer on a free rotating disk. The simulated experimental case is the 25 Hz with $\varepsilon = 0.082$ (see Table 6.3, no. 2). The RANS modeling method is chosen in the CFD part of the thesis. Implicit unsteady analysis is found to be appropriate when modelling the rotating walls. The disk is the aluminum material, and the fluid is the air. The thermophysical and geometrical properties of disk are given in Table 7.1 and thermophysical properties of air are given Table 7.2.

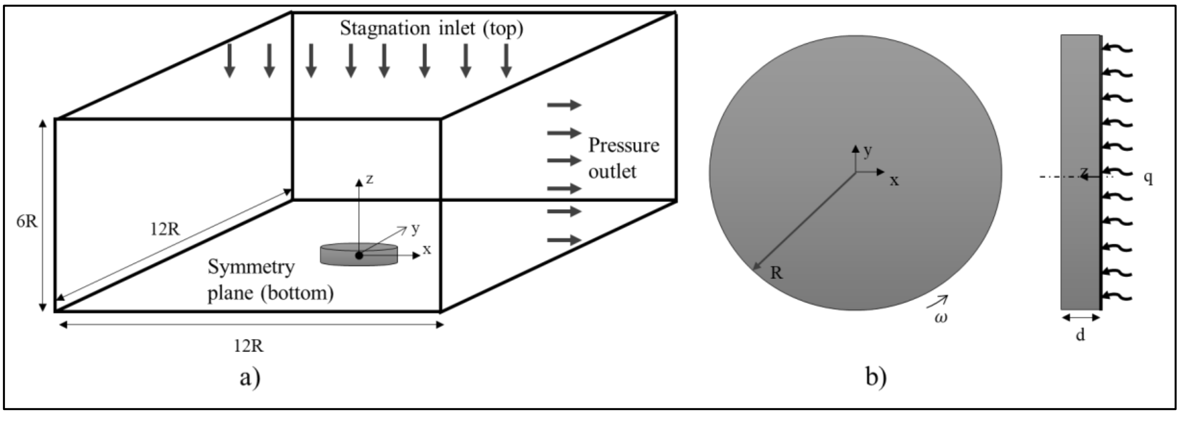

Figure 7.1. Schematic presentation of CFD model of the rotating disk

Geometry

Geometry of the disk in the model is taken directly from the disk in the experimental setup. Geometry of the external air domain is chosen with respect to important and related studies [99,100] on convective heat transfer over a rotating disk. Although the study in [99,100] focused on a LES (Large Eddy Simulation), the considerations in these studies are used as a starting point. The optimum size of the air domain in x and y axes (parallel to disk plane) are 12R and in z axis it is 6R which is parallel to the axis of rotation, see Figure 7.1 a) for a disk with the surrounding air domain and b) disk with the heat flux detail (not to scale).

Table 7.1. Thermophysical and geometrical properties of the disk

Property	Value
Thermal conductivity, k (W/ (m K))	237
Specific heat, c (J/ (kg K))	903
Density, ρ (kg/m^3)	2702
Thickness, d (m)	0,010
Radius, R (m)	0,2
Surface area, A_d (m^2)	0,1256

Turbulence with the transition modeling

Choice of the modeling of the turbulence is important when a rotating disk case is under investigation. Having a suitable mesh, the correctness of the findings is contingent on the selection of the turbulence model, which must be performed separately for each problem to be analyzed [75]. SST (Menter) K-Omega turbulence model [28] is employed as it has been shown to give more accurate results for rotating flows [101,102]. Turbulence modeling is enhanced with Gamma γ-model [27] which works with the SST (Menter) K-Omega turbulence model. The Gamma γ-model is a locally correlated transition model; it predicts the transition by solving one transport equation of intermittency that depends on local variables. There are some benefits in this model compared to the prior model [103], including a simplified formulation and enhanced implementation in CFD codes with moving walls.

The correlation for the critical Reynolds number, $Re_{\theta c}$, consists of two local variables, three model parameters and one function.

$$\mathrm{Re}_{\theta c}\left(Tu_L, \Gamma_{\theta L}\right) = C_{TU1} + C_{TU2}\, e^{\left(-C_{TU3} Tu_L F_{PG}\left(\Gamma_{\theta L}\right)\right)} \tag{7.1}$$

Where, Tu_L is the local turbulence intensity and F_{PG} the model correlation function. The formulation itself is rather simple and the parameters of this model are more accessible for modifications than in the previous transition model. The first parameter C_{TU1} specifies the minimum value for $Re_{\theta c}$. This is necessary because the exponent is approaching zero, while the local turbulence Tu_L is gaining elevated values. The equation reaches its maximum value when Tu_L approaches zero levels, hence the sum of $C_{TU1} + C_{TU2}$ determines the maximum value of $Re_{\theta c}$. Parameter C_{TU3} inside the exponent controls the rate of change of turbulence intensity.

Table 7.2. Thermophysical properties of the air

Property	Value
Specific heat, c (J/ (kg K))	1003,62
Density, ρ (kg/m^3)	1,184
Sutherland temperature for viscosity, S (K)	110,4
Reference temperature, T_{ref}	273,15
Reference kinematic viscosity, ν_{ref} (m^2/s)	1,42-5
Reference thermal conductivity, k_{ref} (W/ (m K))	0,0241
Sutherland temperature for conductivity, S_k (K)	194

Mesh

Polyhedral mesh feature of Simcenter Star-CCM+ is used for the mesh generation. Stretching prism layer is created on solid walls for the best resolution of the boundary layer in the model. Detail views of the mesh of CFD model is shown in Figure 7.2, where a) shows the view of air domain with inlet (top) and pressure outlets, b) shows the solid disk with symmetry plane at the bottom and c) shows the mesh in the y-z plane with zoomed in view of prism layer section.

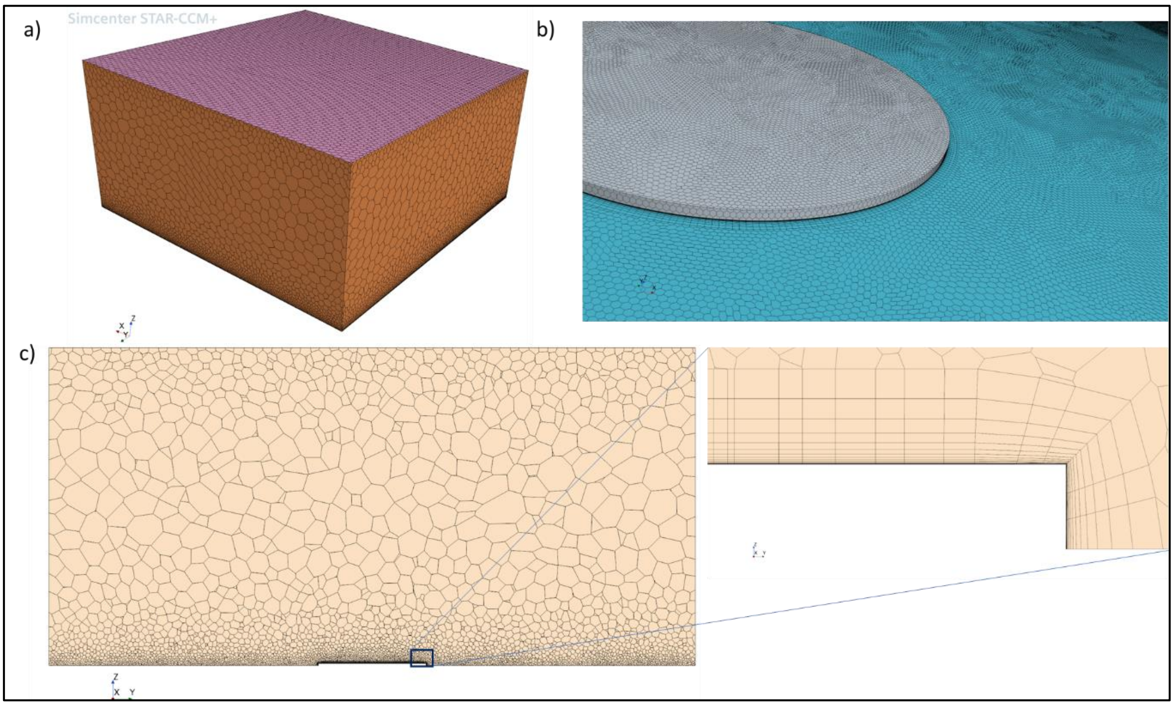

Figure 7.2. Views of the mesh of the CFD model

Thickness of the turbulent boundary layer is predicted through the power law. The equation for the estimation of thickness of turbulent boundary layer is

$$\delta_{turb} = 0.5261R\left(\frac{\nu}{R^2\omega}\right)^{1/5} \tag{7.2}$$

The prism layer thickness is assigned according to the result of equation (7.2) in the CFD model. For a general 1/n power law, the coefficients of necessary parameters can be found from [61].

$$\chi^2 = \frac{4(3n+2)(2n+1(n+1))}{n^2\left(16n^3+85n^2+145n+66\right)} \tag{7.3}$$

Using the parameter χ, radial and tangential shear stresses at the edge of the disk can be estimated [24]

$$\tau_r = 0.0225\rho\chi^{7/4}(r\omega)^{7/4}\left(\frac{\nu}{\delta}\right)^{1/4}\left(1+\frac{1}{\chi^2}\right)^{3/8} \tag{7.4}$$

$$\tau_\theta = -0.0225\rho\left(r\Omega\right)^{7/4}\left(\frac{\nu}{\delta}\right)^{1/4}\left(1+\chi^2\right)^{3/8} \tag{7.5}$$

Total shear stress is calculated using equations (7.4) and (7.5). After that, friction velocity $U_\tau = \sqrt{\tau_w / \rho}$ is calculated. Using the friction velocity, maximum size of near-wall cell is calculated $y_{wall} = y^+\nu / U_\tau$ which is 1.087×10^{-5} m. The optimum magnitude for y^+ in transition modelling is 1 as suggested by the inventors of the Gamma γ-model. So that 1 is chosen for y^+ in the calculation of size of near-wall cell.

<u>Boundary conditions</u>

Air: Rotational motion is defined in the air regions that are in contact with the disk walls. Boundary conditions for the top side is stagnation inlet and four side walls are pressure outlets. The bottom is symmetry plane so that the flow does not have any imposed shear resistance on it, see Figure 7.2.

Disk: Rigid body motion (rotation) is applied for the disk body. Uniform heat flux is defined at the bottom of the disk. Top and side walls of the disk are in contact with the air domain see Figure 7.2. In contacting regions, the implicit energy coupling option is activated for the conjugate solution of the solid domain with the fluid domain.

Grid convergence is checked using four different cell numbers, see Figure 7.3. The optimum number of cells in terms of computational time is sought in terms of radial velocity distribution, one of the key boundary layer parameters. The radial velocity distributions are taken from the boundary layer lying in expectedly laminar part (at the r = 0.08 m) and compared with the velocity distribution calculated by von Karman similarity equations and its label is “Theory” in the figure. After performing the analysis, grid number 1,273,899 labeled as "Star-CCM+ Grid 3" in the figure, is found to be optimal in terms of the compromise between the computational time and the accuracy. It can be stated that for all grid numbers there is a deviation from the exact solution after about z = 0.001 m. However, CFD model is developed with the main purpose of convective heat transfer investigations. Looking at the u_r distribution of "Star-CCM+ Grid 3" at the very-near wall from the simulation, it matches the theory well, see Figure 7.3 (zoomed in view). Consequently, it can be stated that the model can mimic the convective behavior effectively. Capability of the model will also be presented in the following validation section.

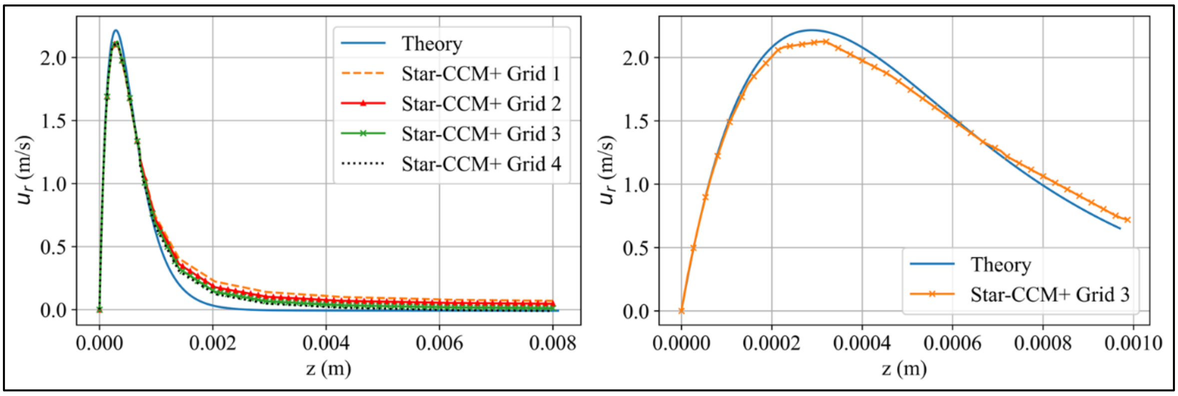

Figure 7.3. The radial velocity distribution in the laminar boundary layer

<u>Solver parameters</u>

Time step size is 0.001 s and total simulation time is 95 s.

7.1.1. Validation of the model

Validation of the model of the rotating disk validated by literature data in terms of key flow parameters. Also, transient radial temperature distributions obtained from the current study and simulations are compared to prove the accuracy of the model regarding its thermal outcomes.

The resulting tangential skin friction of the CFD model is compared with Cochran [64] and the experimental study on turbulent flow over rotating disk in still air by Itoh&Hasegawa [73] , see Figure 7.4. According to figure, tangential skin friction distribution over the radius (also with the local rotational Reynolds number) agrees quite well both in laminar and turbulent region. It is seen from figure that after about $Re_\omega = 8.5 \times 10^4$ laminar flow breaks down and instability starts and then after about $Re_\omega = 2.2 \times 10^5$ transition to turbulence occurs.

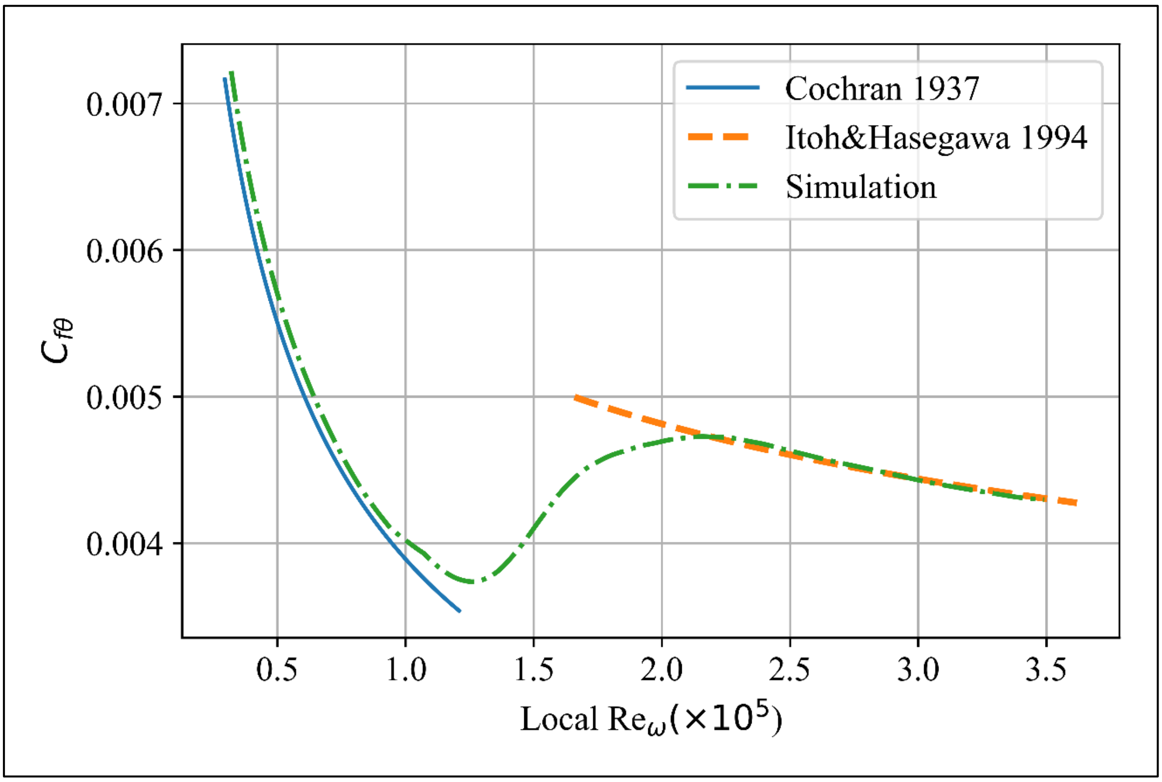

Figure 7.4. Comparison of tangential skin friction

Furthermore, normalized TKE distribution of the CFD model is compared_with the experimental results of Itoh&Hasegawa [73], the curves are shown in Figure 7.5. Results of Star-CCM+ is taken from near the edge of disk, i.e., at r = 0.195 m, because that Itoh&Hasegawa [73] reported the TKE distribution for $Re_\omega = 4 \times 10^5$ and in doing so the Re_ω values are matched. Comparison is realized in terms of TKE normalized by friction velocity U_τ as presented in Itoh&Hasegawa [73]. Normalized TKE distributions shows a good agreement when the Figure 7.5 is observed.

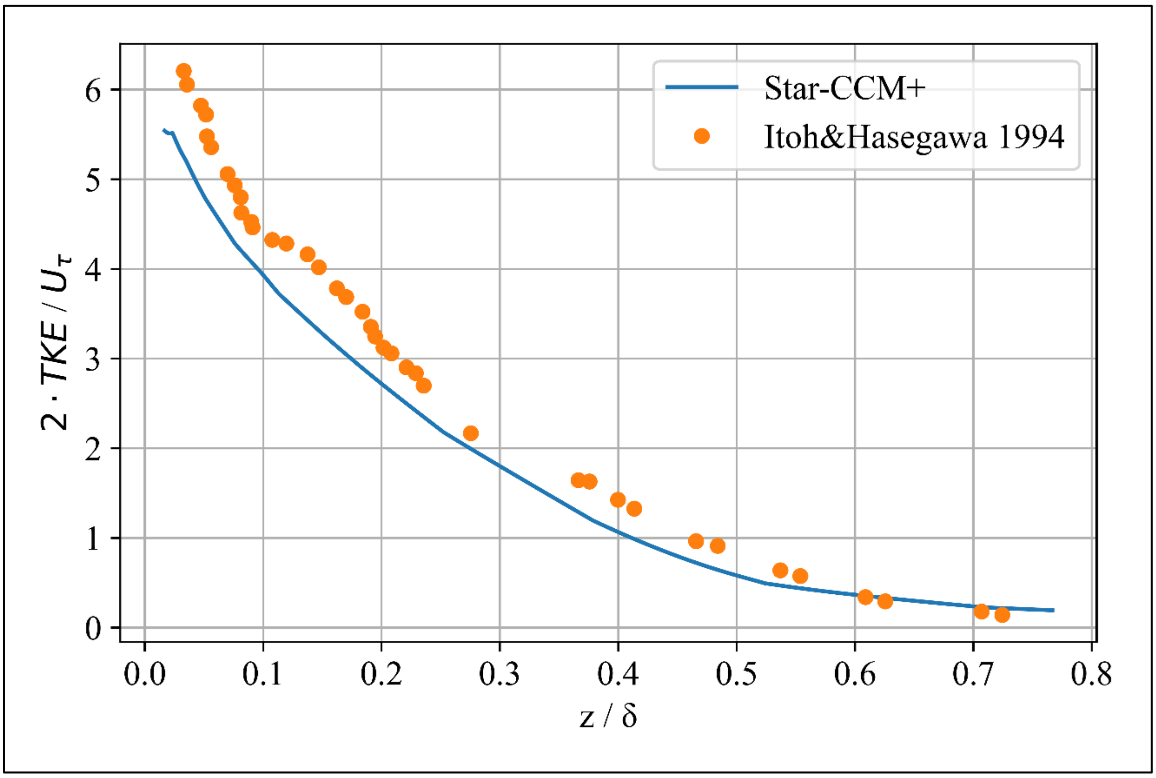

Figure 7.5. Comparison of normalized TKE

Tangential velocity distributions through the boundary layer are shown for several radial locations together with the corresponding tangential velocity distribution obtained by von Karman's similarity solution, see Figure 7.6. Flow behavior is clearly laminar at the $r* = 0.4$ and at the $r* = 0.6$ deviation from the laminar flow behavior has already been visible. Finally, at the $r* = 0.75$ the flow is no longer laminar at all with a sharp tangential velocity gradient.

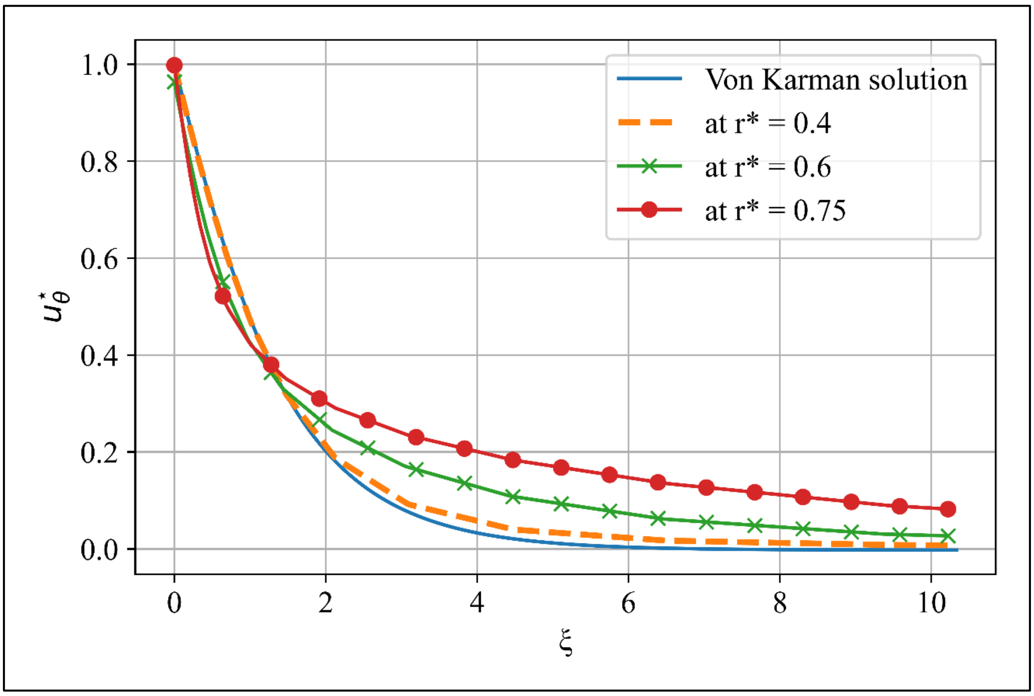

Figure 7.6. Comparison of non-dimensional tangential velocity distributions

Similarly, a comparison is done for the temperature distribution through the boundary layer at several radial locations, see Figure 7.7. Same behavior is also observed when looking at the temperature distributions. It can be said that the CFD model is well capable at capturing the main flow and thermal parameters with a good degree of accuracy, including the signature of a flow having a transition region.

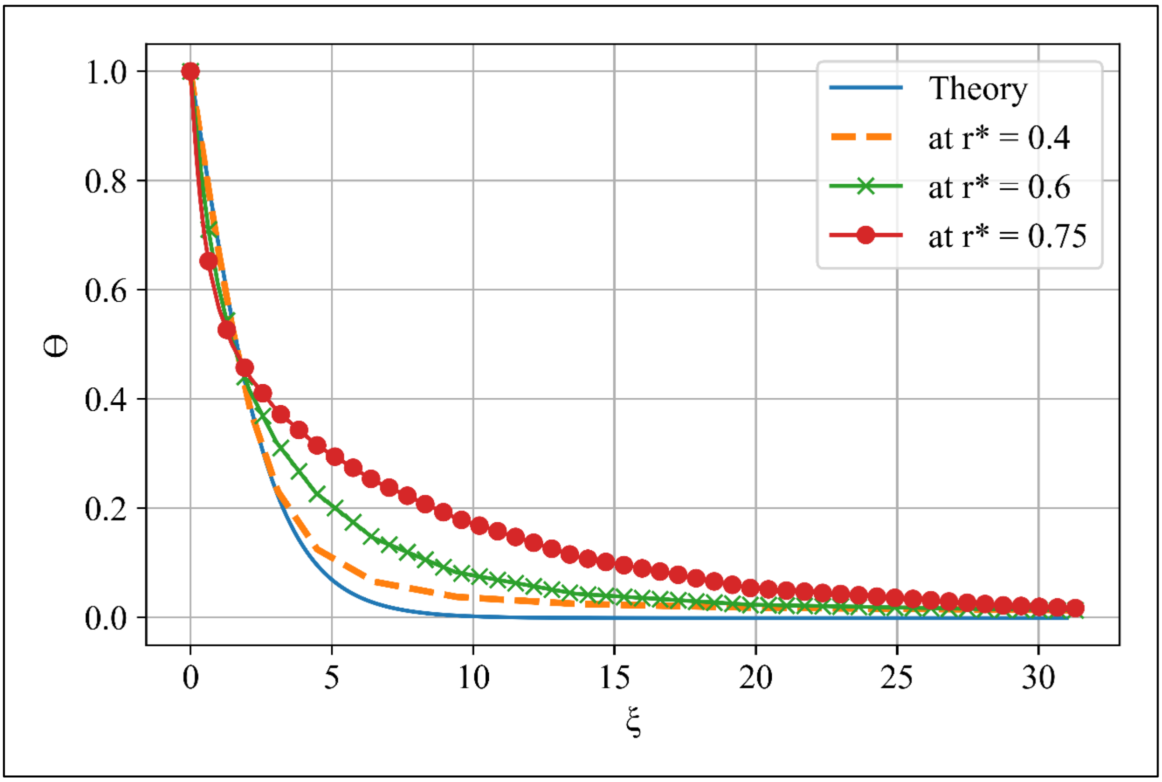

Figure 7.7. Comparison of non-dimensional temperature distributions

Next step in validating the model is done through the comparison of the model with experimental results. The comparisons are based on thermal characteristics such as the temperature and the local Nusselt number distribution along the radial line from both cases. Results are taken from the experiment number 7 (see, Table 6.3) as the boundary conditions of the CFD model is based on that experiment.

Temperature distributions over a radial line obtained from the experiment and simulations are shown in Figure 7.8. All the time instants of simulation in the figure have a good match with the experimental results. Therefore, it is clear that the cooling behavior of the uniformly heated disk with constant heat flux is well captured through the CFD model of the rotating disk.

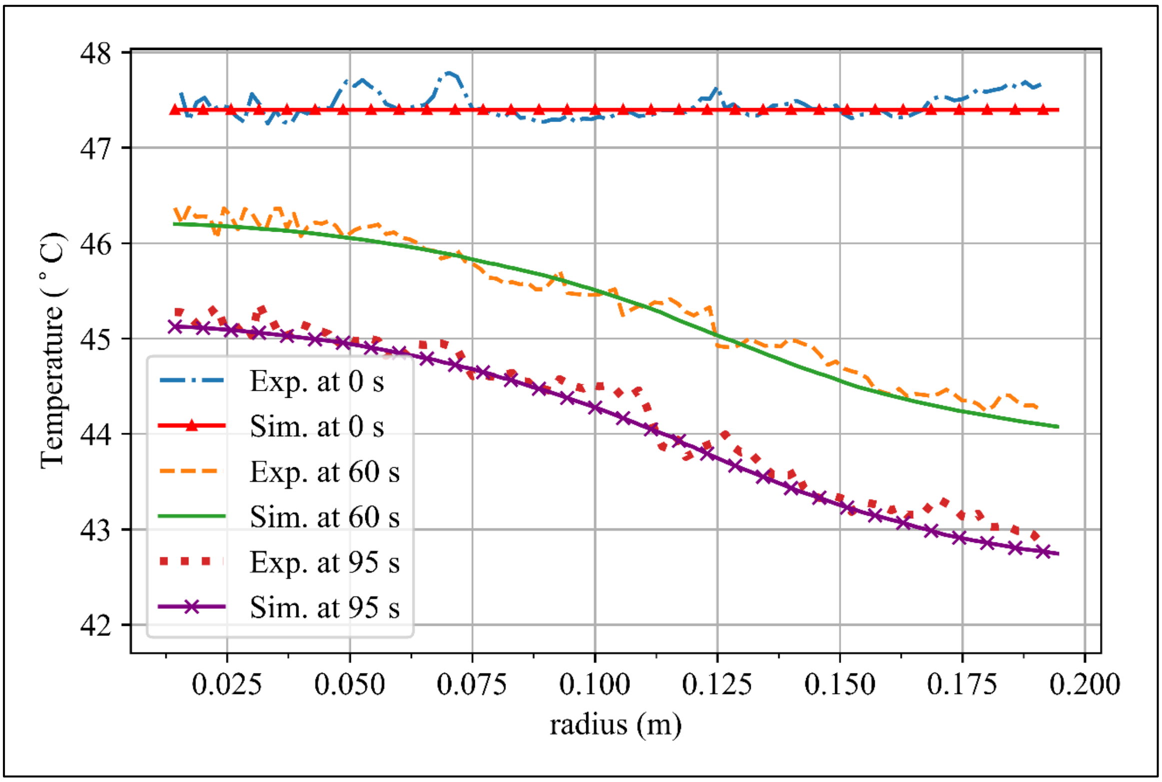

Figure 7.8. Comparison of temperature distributions over the radius

Final comparison is made in terms of the local Nusselt number dependence on local Reynolds number, see Figure 7.9 that includes zoom in view for the range of local Reynolds number $5 - 11 \times 10^4$. According to the figure, the local Nusselt number distribution of the simulation follows a similar trend to that of the experiment. The model and experimental results are particularly in alignment in laminar part that is approximately up to Re_ω = 8.5×10^4. Then, both curves follow a higher gradient than the laminar curve with respect to the local Reynolds number. It shows that the boundary conditions and given parameters for the transition modelling lead to a range of desirable results in terms of aerothermal parameters.

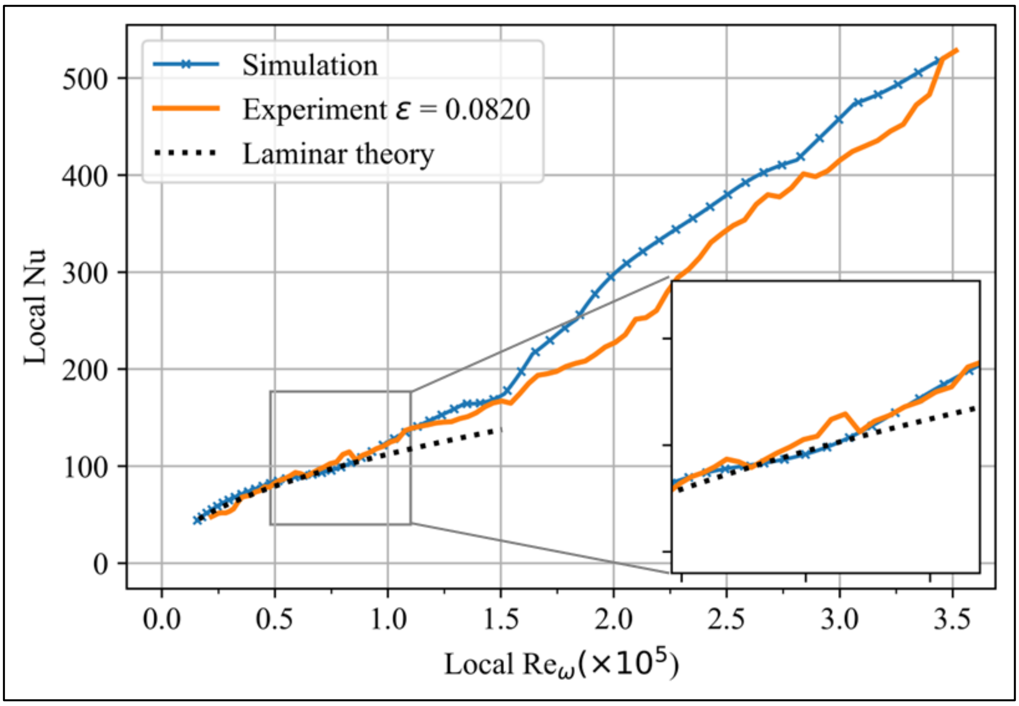

Figure 7.9. Comparison of local Nusselt number distribution

7.2. The CFD Modeling of the Brake Disk

The CFD model of heated free rotating disk with transition-turbulence modeling has yielded valuable results when they are compared with the flow related parameters from the reliable literature data and the experimental data from experiment in this thesis study. Therefore, it is hypothesized that the methodology and assumptions in the CFD model of the heated free rotating disk can also be used for a brake disk. Such a CFD model of brake disk with cooling ribs can also yield reliable results for the case of free constant rotation case (drag braking case in test rig).

The geometry of the brake disk is similar to a commercial brake disk used in modern railway vehicles, see Figure 7.10. Some simplifications are applied on the actual geometry for two reasons, firstly, it is a usual practice in CFD modeling of complex engineering systems/parts. Secondly, the actual geometry is provided by a private manufacturer so that confidentiality criteria is sought. Nevertheless, the main geometrical parameters of the disk are the same as those used in the thermal modelling section, namely the inner and outer radius. Again, the assumption of axial symmetry is used in this model. The shape of the cooling ribs is a truncated cone with base diameter of 30 mm and tip diameter of 14 mm. Length of the ribs is 40 mm. Thickness of the friction plate is 15 mm. There are 4 rows of ribs namely a, b, c and d with rib a having lowest radial position while rib d has the highest one. This is called one set of rows and there are 36 sets of rows in circumferential direction. That makes total number of ribs 144.

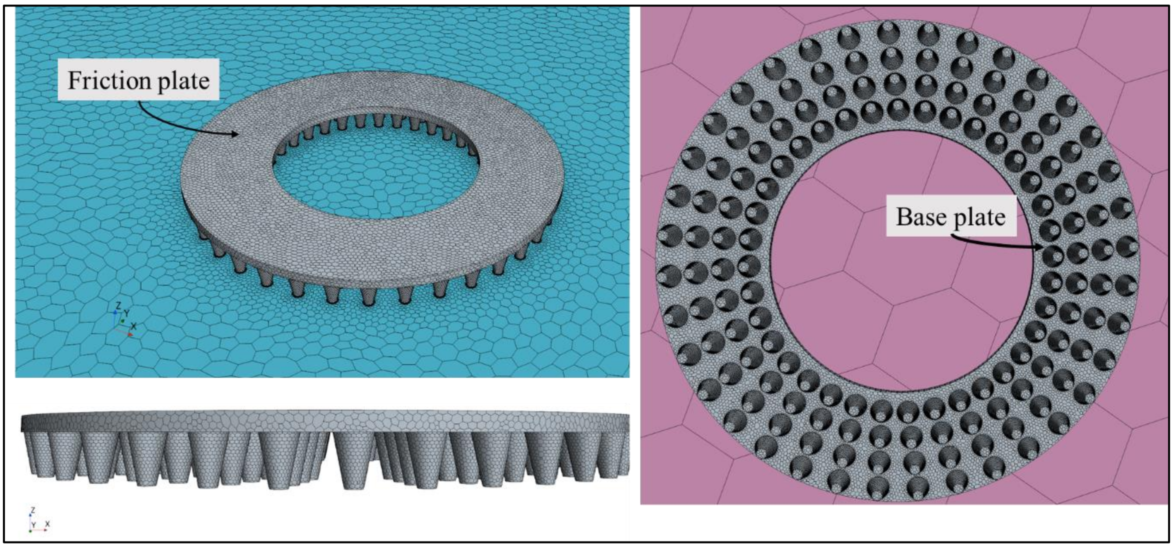

Figure 7.10. View of the railway brake disk geometry with the mesh structure

Boundary conditions for the laminar case

The conjugate heat transfer model of the railway brake disk is created. Angular velocity of 20 rad/s (velocity is V = 32.4 km/h and rpm is 191 for a wheel radius of 0.45 m) is defined for the rigid body rotation of railway brake disk. Uniform heat flux $q = 7 \times 10^4$ W/m^2 is applied at the friction plate which is a reasonable assumption reported by previous [39,40] studies on drag braking. Again, symmetry plane is applied at the bottom side with which the ribs are in the contact. Therefore, there is also adiabatic conditions on tip of the ribs. The initial temperature of the disk is 100 $°C$ and ambient air is at 23 $°C$. Time step size is 0.001 s and total simulation time is 6 s.

7.2.1. Results of the CFD model of brake disk

Results of the CFD model of the brake disk is presented in terms of velocity vector plots and thermal parameters. Figure 7.11 shows the velocity vectors at z = 17 mm which is the plane 2 mm above friction plate. The brake disk rotates around z axis in positive direction. Velocity vector is mainly composed of tangential and radial components while former has a higher contribution. According to the figure it can be stated that the flow above the brake disk resembles the free rotating disk laminar flow. Flow around the ribs at z = - 17 mm which is the plane 2 mm below the base plate is shown in Figure 7.12. This scalar tangential velocity bar is filtered between 0.02 – 6.18 m/s to achieve better visualization. The flow across truncated cone-shaped ribs seems rather complicated as there are narrow passages between the ribs. Ribs rotates with a relatively low speed and they cause the air to move around them. There is low momentum levels created by lower tangential (linear) speeds of ribs especially in row b and row c since they are trapped by row a and row c. Furthermore, there is no parallel or impinging flow into the brake disk.

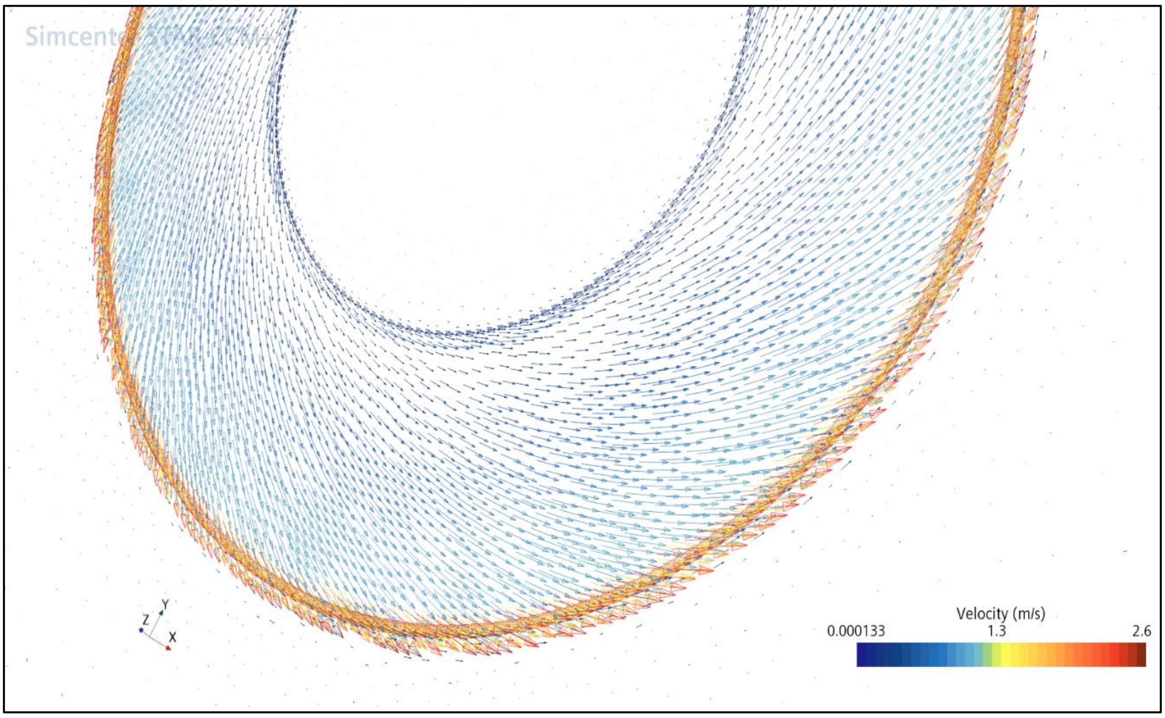

Figure 7.11. Velocity vector scene at z = 17 mm

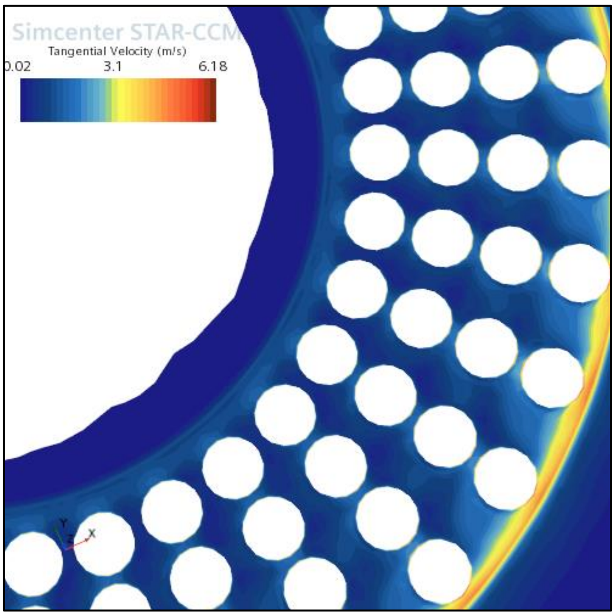

Figure 7.12. Tangential velocity scalar scene at z = -17 mm

The temperature distribution of friction plate as a contour plot (scalar scene in Star-CCM+) is shown in Figure 7.13. The friction plate with a great amount of heat flux yields uniform temperature distributions around 111 ℃. However, this plot is provided to show the effect of cooling ribs. That is, in the presence of ribs in the axial extension of the friction plate, lower temperatures are observed than in the neighboring regions, which is an expected outcome. The temperature distribution of base plate with ribs are shown in Figure 7.14. It is also seen in the figure that the ribs provide a cooling effect on the brake disk.

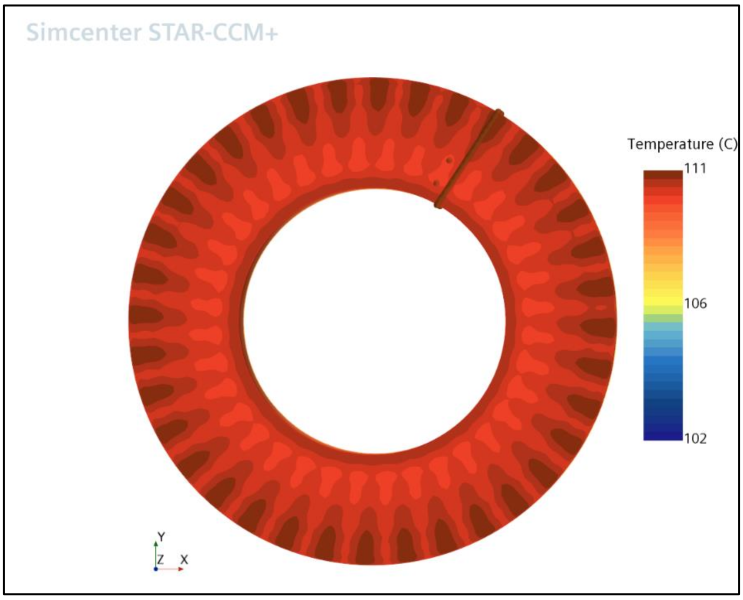

Figure 7.13. The temperature distribution of friction plate

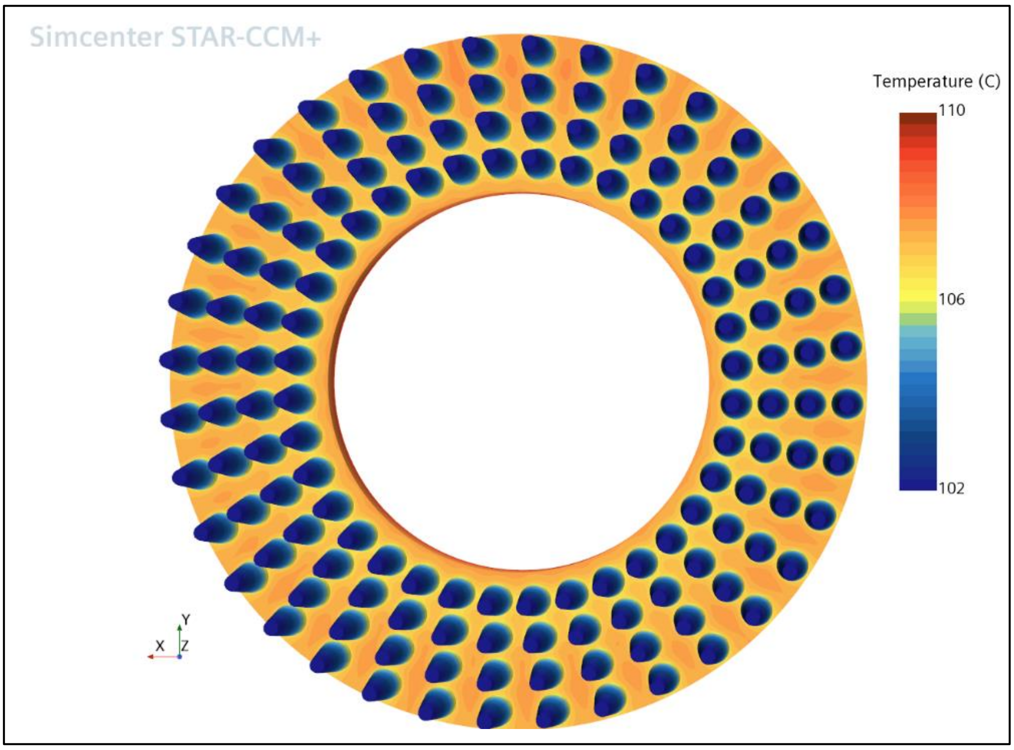

Figure 7.14. The temperature distribution of base plate

Detail view of the ribs is shown in Figure 7.15. There is a negative temperature gradient from the friction plate to the tip of the ribs. Also, the locations of rib a, b, c, d and the radial line for next plots are shown in Figure 7.15.

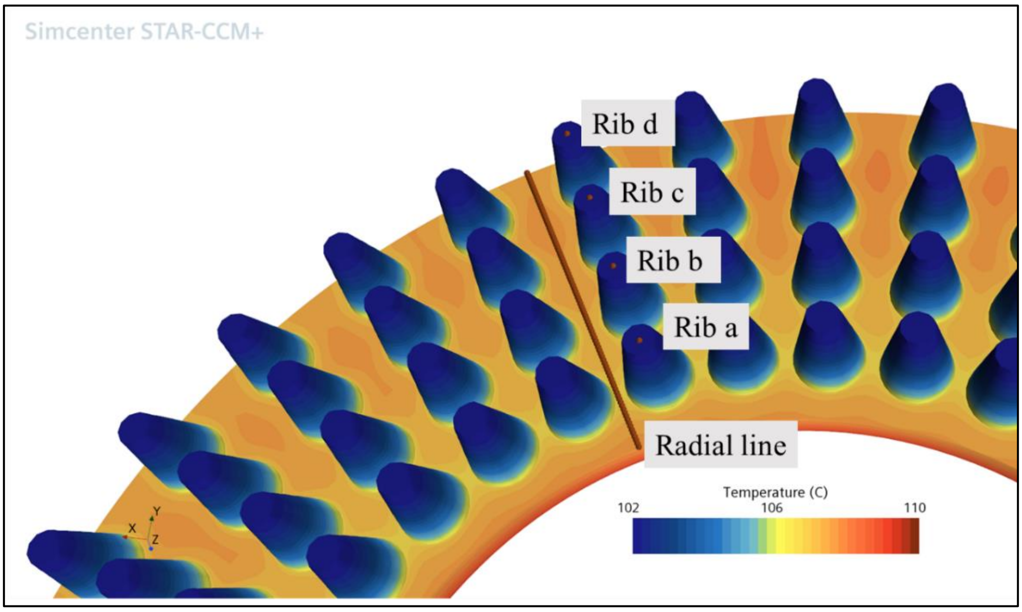

Figure 7.15. Detail view of the temperature distribution of ribs

Temperature distribution from a set of rows (rib a, b, c and d) are shown in Figure 7.16. Each curve represents temperature of the line that passes through the center of a rib from the friction plate to the tip of the ribs.

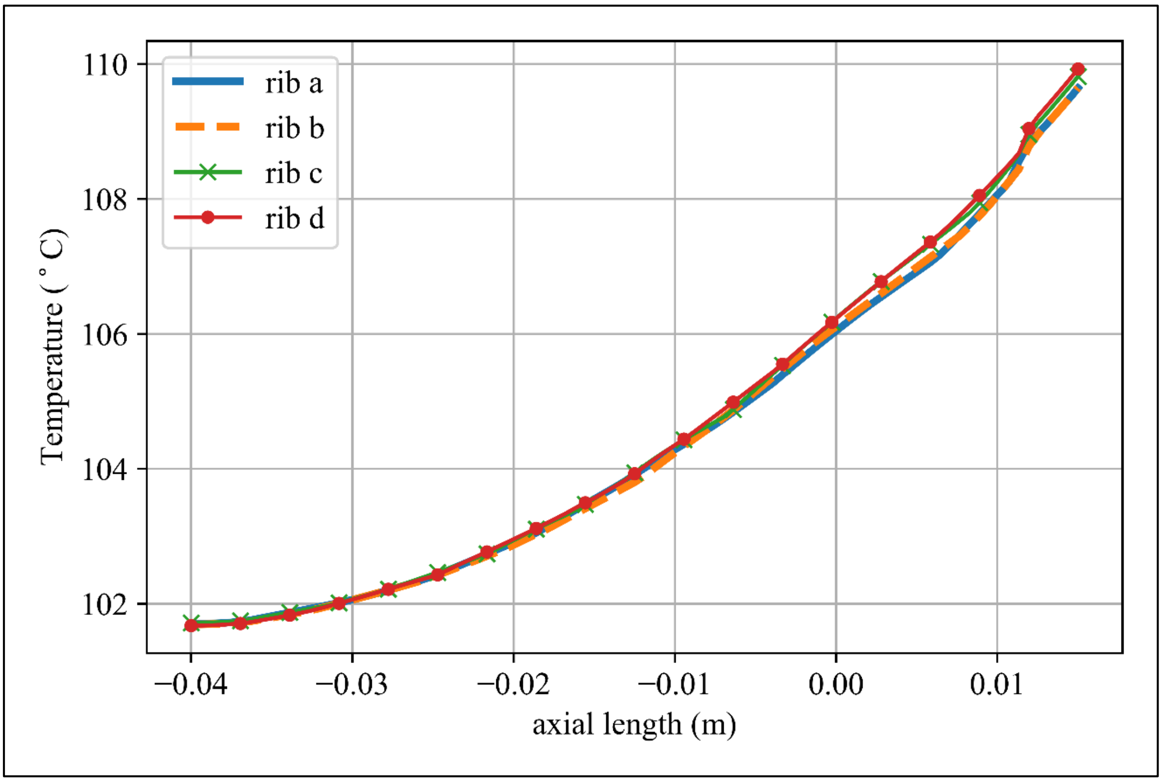

Figure 7.16. Temperature distribution of each rip in a set of rows

Heat transfer coefficient (HTC) distribution over a radial line in base plate (in middle space of two set of rows, see Figure 7.15) is shown in Figure 7.17.

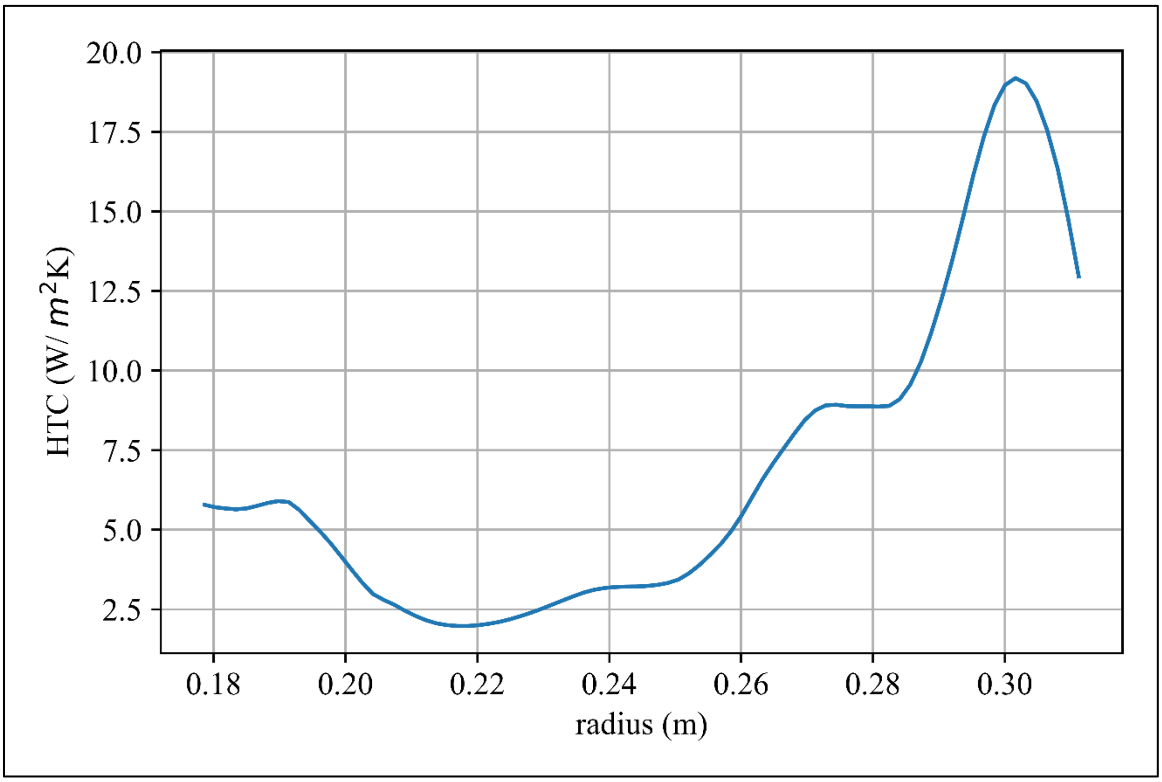

Figure 7.17. The HTC distribution over a radial line in base plate

The HTC distribution over a radial line has a value around 2.5 – 5 W/m^2 K up to r = 0.26 m and then it suddenly grows with the radius. The lower level of HTC is high likely caused by natural convection-like effect in the area around row b and row c. This can be deduced firstly from the fact that simulated case is the free rotating disk case (no parallel or impinging flow into the brake disk surface). Secondly, the range of HTC is rather lower in r = 0.2 to r = 0.25 m and here the HTC values are representative of a natural convection case for the air. The sudden increase after r = 0.26 the is caused by higher tangential velocity and the fact that the air is free to move at the outer radius whereas around row b and row c, the air basically trapped. It is important to notice that the tangential velocity distribution in Figure 7.12 is in line with this HTC distribution.

Friction plate yields almost uniform HTC distribution which approximately is 11 W/m^{2}K. If the Nusselt correlation is manipulated with Nusselt definition for laminar flow as in the following

$$\left.\begin{array}{l} Nu = \dfrac{h\,r}{k} \\ Nu = K\,\mathrm{Re}_{\omega}^{c_R} \end{array}\right\rangle \frac{h\,r}{k} = K\left(\frac{\omega r^2}{\nu}\right)^{0.5} \Rightarrow$$
$$h = K\left(\frac{\omega}{\nu}\right)^{0.5} k \tag{7.6}$$

Then HTC can be expressed as independent from the radius shown in equation (7.6). Using (7.6) gives h = 10.84 W/m^{2}K which agrees quite well with 11 W/m^{2}K value obtained in Star-CCM+. Therefore, it can be hypothesized that the CFD model predicts the convective heat transfer coefficients satisfactorily well. In turn, outcomes of the CFD can be utilized in a thermal model for drag braking simulations.

8. CONCLUSIONS AND RECOMMENDATIONS

In the first part of the thesis, a model of a train brake disk is developed for transient thermal distribution and axial thermal stress distribution in Python programming language with optimized numerical calculation libraries. Model is built with the consideration of criteria established by "Journals of Fluid Engineering" on the accuracy of CFD models. Simulation results of the model are compared with a numerical-experimental study on train brake disk with the same parameters. The developed model has shown good agreement with the previous research. Furthermore, two models, one with the same configurations as the developed model and the other one with variable thermal parameters, are built in Simcenter STAR-CCM+, a well-established and validated commercial CFD and computational heat transfer tool.

The developed model is shown to be capable of fast, robust, and accurate with more realistic boundary conditions considering the transient nature of brake disk in terms of thermal behavior. The model can be used to predict the temperature distribution and axial thermal stress distributions of a disk beforehand and possibly with fewer experiments in the early stages of the development phase. Therefore, obtaining quick and valuable insights before the challenging experiments phase is possible in terms of the functionality and safety requirements of a railway brake disk. Using the new model, parametrical and optimization studies focusing on the thermal behavior, thermal stress, and lightweight improvements on disk can be carried out with a higher resolution. Then, questions such as where and when the maximum temperatures occur can be answered due to the specific heat flux implementation and the solution method with variable time-step size in the developed model. Also, predictions for the thermal stress behavior under various conditions with moderate accuracy can be carried out with developed model and thermal stress prediction method adapted in this study.

Other findings from the study are that for a given gray cast iron material, constant thermal property approach is not a very suitable option when temperature evolutions/distributions are to be correctly estimated, especially for higher speeds that yield more prolonged braking duration and higher temperature levels. On the other hand, the constant property approach overestimates the temperature values, which is favorable when the safety margin is considered. Also, the effect of specific heat of the material is more pronounced than the effect of thermal conductivity on the thermal behavior of the disk. However, the inclusion of variable thermal properties does not result in significant differences for thermal stress distributions.

In the second part, the results of an experimental study employing an electrically heated rotating disk in still air together with its CFD modeling (including conjugate heat transfer and transition modeling) were reported. Local surface temperatures of the disk were measured employing an IR camera and specialized ResearchIR software. Then, using the python code with a novel approach, heat transfer coefficients were determined over the disk radius. Effect of the heating strength (perturbation parameter) on the stability of the rotational flow field over the disk were investigated systematically under different rotational speeds. Also, results are compared in terms of thermophysical values calculated by the property-ratio method and film temperature method. Experimental results are compared with reliable studies in the field, and the outcomes are in good agreement with those studies. A novel approach in setting up the experiment together with the evaluation of the results through the lumped capacitance approach seems to be promising. Another important result of the experimental work is that for the first time the qualitative variation of the onset of instability with the heating strength for the air flow on a rotating disk has been demonstrated by an experimental method. This finding also indicates that for a heated rotating disc (and indirectly the brake disc), the flow becomes turbulent over a smaller radius as the heating power increases. New thermal modeling studies in the area should consider this fact when using empirical correlations for laminar and turbulent regime.

An experimental setup with the highest rotational speed is modelled in Simcenter Star-CCM+. The main features of the model are that it is transient, three-dimensional and includes the simultaneous solver (conjugate) with a relatively recent transitional model. The CFD model of the rotating disk is compared firstly with the key flow parameters such as skin friction distribution and turbulent kinetic energy reported in previous studies with similar experimental configurations. These parameters were quite in good agreement and the signature of a transitional flow was also observed through transitional model included in the developed CFD model. Apart from that, thermal parameters are compared which showed that cooling behavior of the disk surface was in quite good agreement with the experimental setup in this study. Another key comparison shows that such a model can provide local

Nusselt distributions over the rotating disk with rotational Reynolds number up to 4×10^5 with a good accuracy.

The methodology of the CFD model of the rotating disk is utilized in building the railway brake disk model in Star-CCM+. The railway brake disk has truncated-cone shaped cooling ribs with a complex geometry. Again, axial symmetry is utilized when modeling the brake disk so that the size of the computational domain has been reduced. The simulation is done with the angular velocity of 20 rad/s which results in a largely laminar flow regime over friction plate. The velocity field seems to be accurately obtained when looking at the vector plot both in friction and base plate with the later having a more complex flow structure due to the rows of ribs in circumferential direction. Although the temperature distribution is almost uniform at the friction plate, effect of existence of ribs reflected in temperature contour plot (scalar scene). The temperature contour plots from the base plate side and temperature distributions of ribs also supports the accuracy of the conjugate heat transfer model with an axial heat flux as a boundary condition. Then, HTC values obtained and presented both for the friction plate and the base plate sides. The HTC value of the friction plate matches the Nusselt number correlation quite well for the rotating disk case. There is no corresponding measurement values for the base plate. However, when the rotation, no inflow boundary condition together with the velocity distribution at the base plate are considered, the HTC distribution seems logical having a low value on the vicinity of inner rows of ribs (natural convection) and higher values on the vicinity of innermost and outermost rib side. These HTC values can be used in a thermal code such as the developed one in first part of this thesis.

The simulation of the CFD modeling of railway brake disk with a complex geometry yields satisfactorily results regarding the drag braking case for a relatively low speed. However, these outcomes must be validated with experiments having a same configuration. Apart from that, higher rotational speeds up to 50 rad/s resulting a linear velocity of 80 km/h, must be simulated. This velocity range corresponds to laminar, transition and turbulent flow regimes coexisting on the friction plate. This case is more challenging and a requirement determined by standards in railway industry for newly designed brake disks. Finally, a validated CFD model then can be used with different cooling rib geometries to investigate their cooling effect on the brake disk.

REFERENCES

1. Gfatter, G., Berger, P., Krause, G., and Vohla, G. (2003). *Basics of Brake Technology*. München: Knorr-Bremse.

2. Kim, D. J., Lee, Y. M., Park, J. S., and Seok, C.-S. (2008). Thermal stress analysis for a disk brake of railway vehicles with consideration of the pressure distribution on a friction plate. *Materials Science and Engineering: A*, 483, 456-459.

3. Degallaix, G., Dufrénoy, P., Wong, J., Wicker, P., and Bumbieler, F. (2007). Failure Mechanisms of TGV Brake Discs. *Key Engineering Materials*, 345, 697-700.

4. Abbasi, S., Wahlström, J., Olander, L., Larsson, C., Olofsson, U., and Sellgren, U. (2011). A study of airborne wear particles generated from organic railway brake pads and brake discs. *Wear*, 273(1), 93-99.

5. Octau, C., Meresse, D., Watremez, M., Schiffler, J., Lippert, M., Keirsbulck, L., and Dubar, L. (2020). Characterization of particulate matter emissions in urban train braking - An investigation of braking conditions influence on a reduced-scale device. *Environmental Science and Pollution Research*, 27, 18615-18631.

6. Kim, S.W., Park, K., Lee, S.H., Kang, K.H., and Lim, K.T. (2008). Thermophysical properties of automotive metallic brake disk materials. *International Journal of Thermophysics*, 29(6), 2179-2188.

7. Breuer, B., and H. Bill, K. (2017). *Bremshandbuch*, Berlin: Springer Vieweg.

8. Wasilewski, P. (2018). Friction Heating in Railway Brakes: A Review of Numerical Models. *Archives of Computational Methods in Engineering*, 27(1), 45-58.

9. Anderson, D., Tannehill, J.C., and Pletcher, R.H. (2016). *Computational fluid mechanics and heat transfer*. London: Taylor and Francis, 23.

10. Rodriguez, S. (2019). *Applied Computational Fluid Dynamics and Turbulence Modeling*. Switzerland: Springer Nature AG, 45.

11. Galindo-Lopez, C. H., and Tirovic, M. (2008). Understanding and improving the convective cooling of brake discs with radial vanes. *Proceedings of the Institution of Mechanical Engineers, Part D: Journal of Automobile Engineering*, 222(7), 1211-1229.

12. Ghadimi, B., Kowsary, F., and Khorami, M. (2013). Thermal analysis of locomotive wheel-mounted brake disc. *Applied Thermal Engineering*, 51, 948-952.

13. Duzgun, M. (2012). Investigation of thermo-structural behaviors of different ventilation applications on brake discs. *Journal of Mechanical Science and Technology*, 26(1), 235-240.

14. Luo, Z., and Zuo, J. (2014). Conjugate heat transfer study on a ventilated disc of high-speed trains during braking. *Journal of Mechanical Science and Technology*, 28, 1887-1897.

15. Cobb, E. C., and Saunders, O. A. (1956). Heat Transfer from a Rotating Disk. *Proceedings of the Royal Society of London. Series A, Mathematical and Physical Sciences*, 236(1206), 343-351.

16. Popiel, C. O., and Bogusławski, L. (1975). Local heat-transfer coefficients on the rotating disk in still air. *International Journal of Heat and Mass Transfer*, 18(1), 167-170.

17. Booth, G. L., and de Vere, A. P. C. (1974). Convective heat transfer from a rotating disc in a transverse air stream. *Heat transfer 1974; Proceedings of the Fifth International Conference*, Tokyo, 2, 30-34.

18. Elkins, C. J., and Eaton, J. K. (2000). Turbulent heat and momentum transport on a rotating disk. *Journal of Fluid Mechanics*, 402, 225-253.

19. Goldstein, S. (1935). On the Resistance to the Rotation of a Disc Immersed in a Fluid. *Mathematical Proceedings of the Cambridge Philosophical Society*, 31(2), 232-241.

20. de Vere, A. P. C. (1975). *Convective Heat Transfer from a Rotating Disc in a Transverse Air Stream*. Doctoral Thesis, University of Leicester, Leicester.

21. Wiesche, S. aus der, and Helcig, C. (2022). Effect of heating on the stability of the three-dimensional boundary layer flow over a rotating disk. *E3S Web of Conferences*, 345, 02007.

22. Helcig, C., aus der Wiesche, S., and Shevchuk, I. v. (2017). Prandtl Number Effect on the Laminar Convective Heat Transfer From a Rotating Disk. *Journal of Heat Transfer*, 139(10), 101702.

23. Miller, R., Griffiths, P. T., Hussain, Z., and Garrett, S. J. (2020). On the stability of a heated rotating-disk boundary layer in a temperature-dependent viscosity fluid. *Physics of Fluids*, 32(2), 024105.

24. Childs, P. R. N. (2011). *Rotating Flow*. London: Elsevier, 91.

25. Grzes, P., Oliferuk, W., Adamowicz, A., Kochanowski, K., Wasilewski, P., and Yevtushenko, A. A. (2016). The numerical-experimental scheme for the analysis of temperature field in a pad-disc braking system of a railway vehicle at single braking. *International Communications in Heat and Mass Transfer*, 75, 1-6.

26. Siemens Digital Industries Software Simcenter STAR-CCM+, version 2021.1.

27. Menter, F. R., Smirnov, P. E., Liu, T., and Avancha, R. (2015). A One-Equation Local Correlation-Based Transition Model. *Flow, Turbulence and Combustion*, 95(4), 583-619.

28. Menter, F. R. (1994). Two-equation eddy-viscosity turbulence models for engineering applications. *AIAA Journal*, 32(8), 1598-1605.

29. Atkins, M. D., Kienhöfer, F. W., Kang, K., Lu, T. J., and Kim, T. (2021). Cooling Mechanisms in a Rotating Brake Disc With a Wire-Woven-Bulk Diamond Cellular Core. *Journal of Thermal Science and Engineering Applications*, 13(4), 041006.

30. Zewang, Y., Chun, T., Mengling, W., Jiajun, Z., and Chao, C. (2021). Modeling and Model Validation of Thermal Behavior of Railway Disc During Single Braking. *Journal of Thermal Science and Engineering Applications*, 13(5), 051017.

31. Wiesche, S. aus der (2002). Heat transfer and thermal behaviour of a rotating disk passed by a planar air stream. *Forschung im Ingenieurwesen*, 67(4), 161-174.

32. Gao, C. H., Huang, J. M., Lin, X. Z., and Tang, X. S. (2007). Stress Analysis of Thermal Fatigue Fracture of Brake Disks Based on Thermomechanical Coupling. *Journal of Tribology*, 129(3), 536-543.

33. Kim, D. J., Seok, C. S., Koo, J. M., We, W. T., Goo, B. C., and Won, J. I. (2010). Fatigue life assessment for brake disc of railway vehicle. *Fatigue and Fracture of Engineering Materials and Structures*, 33(1), 37-42.

34. Limpert, R. (1972). An Investigation of Thermal Conditions Leading to Surface Rupture of Cast Iron Rotors. *SAE Transactions*, 81(3), 1507-1520.

35. Boley, B. A., and Weiner, J. H. (1960). *Theory of Thermal Stresses*. New York: Dover Publications, 82.

36. Dalal, Y. S. (2017). *Effect of Design Parameters on Thermal Performance of a Vane Type Disc Brake Rotor*. Master Thesis, Western Michigan University, Michigan.

37. Limpert, R. (1975). *Cooling analysis of disc brake rotors*. Canada: SAE Technical Papers, 3.

38. Vdovin, A., and le Gigan, G. (2020). Aerodynamic and thermal modelling of disc brakes - Challenges and limitations. *Energies*, 13(1), 1-12.

39. Tang, J., Bryant, D., and Qi, H. (2014). *Coupled CFD and FE Thermal Mechanical Simulation of Disc Brake*. EuroBrake, 13-15 May, Lille, France.

40. Grivc, U., Deržič, D., and Muhič, S. (2019). Numerical optimisation and experimental validation of divided rail freight brake disc crown. *Journal of Modern Transportation*, 27(1), 1-10.

41. Latour, B., Bouvier, P., and Harmand, S. (2011). Convective heat transfer on a rotating disk with transverse air crossflow. *Journal of Heat Transfer*, 133(2), 021702.

42. Trinkl, C. M., Bardas, U., Weyck, A., and aus der Wiesche, S. (2011). Experimental study of the convective heat transfer from a rotating disc subjected to forced air streams. *International Journal of Thermal Sciences*, 50(1), 73-80.

43. Lingwood, R.J. (1996). An experimental study of absolute instability of the rotating-disk boundary-layer flow. *Journal of Fluid Mechanics*, 314, 373405.

44. Malik, M. R., Wilkinson, S. P., and Orszag, S. A. (1981). Instability and transition in rotating disk flow. *AIAA Journal*, 19(9), 1131-1138.

45. Kobayashi, R., Kohama, Y., and Takamadate, C. (1980). Spiral vortices in boundary layer transition regime on a rotating disk. *Acta Mechanica*, 35(1-2), 71-82.

46. Schlichting, H. (1960). *Boundary Layer Theory*. New York: McGraw-Hill, 325.

47. Herwig, H., Wickern, G., and Gersten, K. (1985). Der Einfluß variabler Stoffwerte auf natürliche laminare Konvektionsströmungen. *Wärme- und Stoffübertragung*, 19(1), 19-30.

48. Gersten, K., and Herwig, H. (1984). Impuls-und Wärmeübertragung bei variablen Stoffwerten für die laminare Plattenströmung (in German). *Wärme und Stoffübertragung*, 18(1), 25-35.

49. Schäfer, P., Severin, J., and Herwig, H. (1995). The effect of heat transfer on the stability of laminar boundary layers. *International Journal of Heat and Mass Transfer*, 38(10), 1855-1863.

50. White, F.M. (2006). *Viscous fluid flow*. New York: McGraw-Hill, 86.

51. Cardone, G., Astarita, T., and Carlomagno, G. M. (1997). Heat Transfer Measurements on a Rotating Disk. *International Journal of Rotating Machinery,* 3, 912069.

52. Pellé, J., and Harmand, S. (2009). Heat transfer study in a rotor-stator system air-gap with an axial inflow. *Applied Thermal Engineering*, 29(8-9), 1532-1543.

53. Pellé, J., and Harmand, S. (2007). Heat transfer measurements in an opened rotor-stator system air-gap. *Experimental Thermal and Fluid Science*, 31(3), 165-180.

54. Astarita, T., Cardone, G., and Carlomagno, G. M. (2002). Spiral Vortices Detection on a Rotating Disk. *23rd International Congress of Aeronautical Sciences, proceedings*, Toronto, Canada, September, 1-8.

55. Cebeci, T., and Bradshaw, P. (1984). *Physical and Computational Aspects of Convective Heat Transfer*. Berlin: Springer-Verlag, 43.

56. Davidson, P. (2015). *Turbulence: An Introduction for Scientists and Engineers*. Oxford: Oxford University Press, 155.

57. Versteeg, H. K., and Malalasekera, W. (2007). *An Introduction to Computational Fluid Dynamics*. London: Pearson, 41.

58. Launder, B. E., and Spalding, D. B. (1974). The numerical computation of turbulent flows. *Computer Methods in Applied Mechanics and Eneryg*, 3, 269-289.

59. Kármán, T. V. (1921). Über laminare und turbulente Reibung (in German). *ZAMM - Journal of Applied Mathematics and Mechanics / Zeitschrift für Angewandte Mathematik und Mechanik*, 1(4), 233-252.

60. Dorfman, L. A. (1964). *Hydrodynamic resistance and the heat loss of rotating solids*, Edinburgh: Oliver & Boyd, 25.

61. Owen, J. M., and Rogers, R. H. (1989). *Flow and heat transfer in rotating-disc systems, Vol. 1: Rotor-stator systems*. Baldock: Research Studies Press, 122.

62. Shevchuk, I. V. (2009). *Convective Heat and Mass Transfer in Rotating Disk Systems*. Berlin, Heidelberg: Springer Berlin Heidelberg, 38.

63. Helcig, C. (2018). *Experimentelle Untersuchung des konvektiven Wärmeübergangs an rotierenden Scheiben*. Doctoral Thesis, Technische Universität München, München.

64. Cochran, W. G. (1934). The flow due to a rotating disc. *Mathematical Proceedings of the Cambridge Philosophical Society*, 30(3), 365-375.

65. Kibel, I. A. (1947). *Prikladnaya Matematika i Mekhanika, PMM. Journal of Applied Mathematics and Mechanics*, 11(6), 8-15.

66. Millsaps, K., and Pohlhausen, K. (1952). Heat Transfer by Laminar Flow from a Rotating Plate. *Journal of the Aeronautical Sciences*, 19(2), 120-126.

67. Sparrow, E. M., and Gregg, J. L. (1959). Heat Transfer From a Rotating Disk to Fluids of Any Prandtl Number. *Journal of Heat Transfer*, 81(3), 249-251.

68. Dorfman, L. A. (1964). Hydrodynamic resistance and the heat loss of rotating solids. *Wear*, 7(3), 307.

69. aus der Wiesche, S., and Helcig, C. (2016). *Convective Heat Transfer From Rotating Disks Subjected To Streams Of Air*, London: Springer International Publishin, 75.

70. Wilkinson, S. P., and Malik, M. R. (1985). Stability experiments in the flow over a rotating disk. *AIAA Journal*, 23(4), 588-595.

71. Watanabe, T. (1989). Effect of surface roughness on boundary layer transition in a rotating disk. *Transactions of the Japan Society of Mechanical Engineers Series B*, 55(515), 1842-1846.

72. Watanabe, T. (1988). Stability of Boundary Layers along a Rotating Disk with Uniform Suction. *ZAMM - Journal of Applied Mathematics and Mechanics / Zeitschrift für Angewandte Mathematik und Mechanik*, 68(1), 21-24.

73. Itoh, M., and Hasegawa, I. (1994). Turbulent Boundary Layer on a Rotating Disk in Infinite Quiescent Fluid. *Japan Society of Mechanical Engineers International Journal Series B,* 37(3), 449-456.

74. Shevchuk, I. V. (2016). *Modelling of convective heat and mass transfer in rotating flows*. Basel: Springer, 154.

75. Shevchuk, I. V. and Avramenko, A. A. (2022). *Modelling of Convective Heat and Mass Transfer in Nanofluids with and Without Boiling and Condensation*. Basel: Springer, 102.

76. Ferziger, J. H., Peric, M., and Street, R. L. (2020). *Computational Methods for Fluid Dynamics*, Basel: Springer, 254.

77. Dorfman, A. S. (2009). *Conjugate problems in convective heat transfer*. Florida: CRC Press, 8.

78. Ghadimi, B., Kowsary, F., and Khorami, M. (2013). Thermal analysis of locomotive wheel-mounted brake disc. *Applied Thermal Engineering*, 51(1-2), 948-952.

79. Limpert, R. (2011). *Brake Design and Safety*. Canada: SAE international, 96.

80. Harris, C.R., Millman, K.J., van der Walt, S.J., Gommers, R., Virtanen, P., Cournapeau, D., Wieser, E., Taylor, J., Berg, S., Smith, N.J., Kern, R., Picus, M., Hoyer, S., van Kerkwijk, M.H., Brett, M., Haldane, A., del Río, J.F., Wiebe, M., Peterson, P., Gérard-Marchant, P., Sheppard, K., Reddy, T., Weckesser, W., Abbasi, H., Gohlke, C., and Oliphant, T.E. (2020). Array programming with NumPy. *Nature*, 585(7825), 357-362.

81. Lam, S. K., Pitrou, A., and Seibert, S. (2015). Numba: a LLVM-based Python JIT compiler. *Proceedings of the Second Workshop on the LLVM Compiler Infrastructure in HPC - LLVM '15*, 1-6.

82. Özişik, M. N. (2017). *Finite Difference Methods in Heat Transfer*. London: Taylor & Francis, 195.

83. Kreith, F., Manglik, R.M., and Bohn, M.S. (2011). *Principles of Heat Transfer*, Massachusetts: Cengage Learning, 243.

84. EN 14535-3 (2015). *Railway applications - Brake discs for railway rolling stock - Part 3: Brake discs, performance of the disc and the friction couple, classification*, European Committee for Standardization.

85. aus der Wiesche, S. (2018). Heat Transfer in Rotating Flows. Francis A. K. (Ed.), In *Handbook of Thermal Science and Engineering*, Berlin: Springer Reference, 647-690.

86. Trinkl, C. M., Bardas, U., Weyck, A., and Aus Der Wiesche, S. (2011). Experimental study of the convective heat transfer from a rotating disc subjected to forced air streams. *International Journal of Thermal Sciences*, 50(1), 73-80.

87. Celik, I. (1993). Numerical Uncertainty in Fluid Flow Calculations: Needs for Future Research. *Journal of Fluids Engineering*, 115(2), 194-195.

88. Roache, P. J., Ghia, K. N., and White, F. M. (1986). Editorial Policy Statement on the Control of Numerical Accuracy. *Journal of Fluids Engineering*, 108(1), 2.

89. Rashid, A., and Strömberg, N. (2013). Sequential simulation of thermal stresses in disc brakes for repeated braking. *Proceedings of the Institution of Mechanical Engineers, Part J: Journal of Engineering Tribology*, 227(8), 919-929.

90. Baron Saiz, C., Ingrassia, T., Nigrelli, V., and Ricotta, V. (2015). Thermal stress analysis of different full and ventilated disc brakes. *Frattura ed Integrita Strutturale*, 9 (34), 608-621.

91. Adamowicz, A. (2015). Axisymmetric Fe Model to Analysis of Thermal Stresses In A Brake Disk. *Journal of Theoretical and Applied Mechanics*, 53(2), 357-370.

92. Jiregna, I. T., and Lemu, H. G. (2021). Thermal stress analysis of disc brake using analytical and numerical methods. *IOP Conference Series: Materials Science and Engineering*, 1201(1), 012033.

93. Kim, D. J., Seok, C. S., Koo, J. M., We, W. T., Goo, B. C., and Won, J. I. (2009). Fatigue life assessment for brake disc of railway vehicle. *Fatigue & Fracture of Engineering Materials & Structures*, 33(1), 37-42.

94. Helcig, C., and aus der Wiesche, S. (2014). Convective Heat Transfer from a Free Rotating Disk Subjected to a Forced Crossflow. *In Turbo Expo: Power for Land, Sea, and Air*, American Society of Mechanical Engineers, 45721, V05BT14A012.

95. Helcig, C., and Aus Der Wiesche, S. (2013). The Effect of the Incidence Angle on the Flow Over a Rotating Disk Subjected to Forced Air Streams. *In Fluids Engineering Division Summer Meeting*. American Society of Mechanical Engineers, 55553, V01BT16A007.

96. FLIR Systems Inc (2022). *ResearchIR 4 User's Guide*.

97. Ozisik, M. N. (1985). *Heat Transfer: A Basic Approach*. New York: McGraw-Hill, 198.

98. Sutherland, W. (1893). LII. The viscosity of gases and molecular force. *The London, Edinburgh, and Dublin Philosophical Magazine and Journal of Science*, 36(223), 507-531.

99. aus der Wiesche, S. (2007). Heat transfer from a rotating disk in a parallel air crossflow. *International Journal of Thermal Sciences*, 46(8), 745-754.

100. aus der Wiesche, S. (2004). LES study of heat transfer augmentation and wake instabilities of a rotating disk in a planar stream of air. *Heat and Mass Transfer*, 40(3-4), 271-284.

101. Amano, R. S., Lucci, J. M., Guntur, K., and Song, B. (2012). Numerical study of the thermal development in a rotating cooling passage. *Heat and Mass Transfer*, 48(6), 1011-1022.

102. Moradi, T., Shahbazian, H., Hoseinalipour, M., and Sunden, B. (2023). Effects of wavy ribs on vortex generation and thermal-hydraulic performance in a rotating rectangular channel. *Applied Thermal Engineering*, 222, 119952.

103. Langtry, R. B. (2006). *A correlation-based transition model using local variables for unstructured parallelized CFD codes*. Doctoral Thesis, Universität Stuttgart, Stuttgart.

APPENDICES

APPENDIX-1**.** Discretized Equations for Thermal Modeling

All the terms in the governing equation (4.7) are discretized as in the following

$$\frac{\partial^2 T}{\partial r^2} = \frac{1}{\Delta r^2}\left(T_{i+1,j,k}^{m+1} - 2T_{i,j,k}^{m+1} + T_{i-1,j,k}^{m+1}\right)$$
$$\frac{1}{r^2}\frac{\partial^2 T}{\partial \theta^2} = \frac{1}{r_i^2 \Delta\theta^2}\left(T_{i,j+1,k}^{m+1} - 2T_{i,j,k}^{m+1} + T_{i,j-1,k}^{m+1}\right)$$
$$\frac{\partial^2 T}{\partial z^2} = \frac{1}{\Delta z^2}\left(T_{i,j,k+1}^{m+1} - 2T_{i,j,k}^{m+1} + T_{i,j,k-1}^{m+1}\right)$$
$$\frac{1}{r}\frac{\partial T}{\partial r} = \frac{1}{r_i \Delta r}\left(T_{i+1,j,k}^{m+1} - T_{i,j,k}^{m+1}\right)$$
$$\frac{1}{\alpha}\frac{\partial T}{\partial t} = \frac{1}{\alpha\,\Delta t}\left(T_{i,j,k}^{m+1} - T_{i,j,k}^{m}\right)$$

Where *i, j* and *k* are the counters of the *r, θ* and *z* axes, respectively, and *m* is the time counter. The discretized derivatives can be expressed as follows:

$$T_{i,j,k}^{n+1} = T_{i,j,k}^{n} + \frac{\alpha\,\Delta t}{\Delta r^2}\left(T_{i+1,j,k}^{n+1} - 2T_{i,j,k}^{n+1} + T_{i-1,j,k}^{n+1}\right) + \frac{\alpha\,\Delta t}{r_i \Delta r}\left(T_{i+1,j,k}^{n+1} - T_{i,j,k}^{n+1}\right)$$
$$+ \frac{\alpha\,\Delta t}{r_i^2 \Delta\theta^2}\left(T_{i,j+1,k}^{n+1} - 2T_{i,j,k}^{n+1} + T_{i,j-1,k}^{n+1}\right) + \frac{\alpha\Delta t}{\Delta z^2}\left(T_{i,j,k+1}^{n+1} - 2T_{i,j,k}^{n+1} + T_{i,j,k-1}^{n+1}\right)$$

Fourier numbers for each coordinate can be defined in the above equation as

$$Fo_r = \frac{\alpha\Delta t}{\Delta r^2},\quad Fo_\theta = \frac{\alpha\Delta t}{\Delta\theta^2}\quad \text{and ,}\quad Fo_z = \frac{\alpha\Delta t}{\Delta z^2}$$

After arrangements of all variables using Fourier numbers, temperature values of current time for each node are obtained via the following equation

$$T_{i,j,k}^{n+1} = \frac{\begin{bmatrix} T_{i,j,k}^{n} + Fo_r\left(T_{i+1,j,k}^{n+1} + T_{i-1,j,k}^{n+1}\right) + \dfrac{Fo_r \Delta r}{r_i}\left(T_{i+1,j,k}^{n+1}\right) \\ + \dfrac{Fo_\theta}{r_i^2}\left(T_{i,j+1,k}^{n+1} + T_{i,j-1,k}^{n+1}\right) + Fo_z\left(T_{i,j,k+1}^{n+1} + T_{i,j,k-1}^{n+1}\right) \end{bmatrix}}{\left(2Fo_r + \dfrac{Fo_r \Delta r}{r_i} + 2\dfrac{Fo_\theta}{r_i^2} + 2Fo_z + 1\right)}$$

APPENDIX-1**.** (Continued) Discretized Equations for Thermal Modeling

Boundary conditions except for zone IV (insulation condition, i.e., zero heat flux through that wall) is given in the following

$$\left.\begin{aligned} & k_d \frac{\partial T}{\partial z} + \rho_d\, c_d\, \frac{\Delta z}{2} \frac{\partial T}{\partial t} = q_d\ , \\ & T_{i,j,nz}^{n+1} = \frac{T_{i,j,nz}^{n} + 2Fo_z T_{i,j,nz-1}^{n+1} + \dfrac{2\Delta t}{\rho c \Delta z} q_d}{1+2Fo_z} \end{aligned}\right\} \text{zone I)}$$

$$\left.\begin{aligned} & k_d \frac{\partial T}{\partial z} + \rho_d\, c_d\, \frac{\Delta z}{2} \frac{\partial T}{\partial t} = h_\omega \left(T_\infty - T_w\right)\ , \\ & T_{i,j,nz}^{n+1} = \frac{T_{i,j,nz}^{n}}{1+2Bi_z Fo_z + 2Fo_z} + \frac{2Bi_z\, Fo_z\, T_\infty + 2Fo_z\, T_{i,j,nz-1}^{n+1}}{1+2Bi_z\, Fo_z + 2Fo_z} \end{aligned}\right\} \text{zone I)}$$

$$\left.\begin{aligned} & -k_d \frac{\partial T}{\partial r} + \rho_d\, c_d\, \frac{\Delta r}{2} \frac{\partial T}{\partial t} = h_d \left(T_\infty - T_w\right)\ , \\ & T_{0,j,k}^{n+1} = \frac{T_{0,j,k}^{n}}{1+2Bi_r\, Fo_r + 2Fo_r} + \frac{2Bi_r\, Fo_r\, T_\infty + 2Fo_r\, T_{1,j,k}^{n+1}}{1+2Bi_r\, Fo_r + 2Fo_r} \end{aligned}\right\} \text{zone II)}$$

$$\left.\begin{aligned} & k_d \frac{\partial T}{\partial r} + \rho_d\, c_d\, \frac{\Delta r}{2} \frac{\partial T}{\partial t} = h_d \left(T_\infty - T_w\right)\ , \\ & T_{nr,j,k}^{n+1} = \frac{T_{nr,j,k}^{n}}{1+2Bi_r\, Fo_r + 2Fo_r} + \frac{2Bi_r\, Fo_r\, T_\infty + 2Fo_r\, T_{nr-1,j,k}^{n+1}}{1+2Bi_r\, Fo_r + 2Fo_r} \end{aligned}\right\} \text{zone III)}$$

APPENDIX-2. Raw Thermal Images

Sample raw thermal images are taken from ResearchIR are shown below. The images are taken from the experiment no. 6.

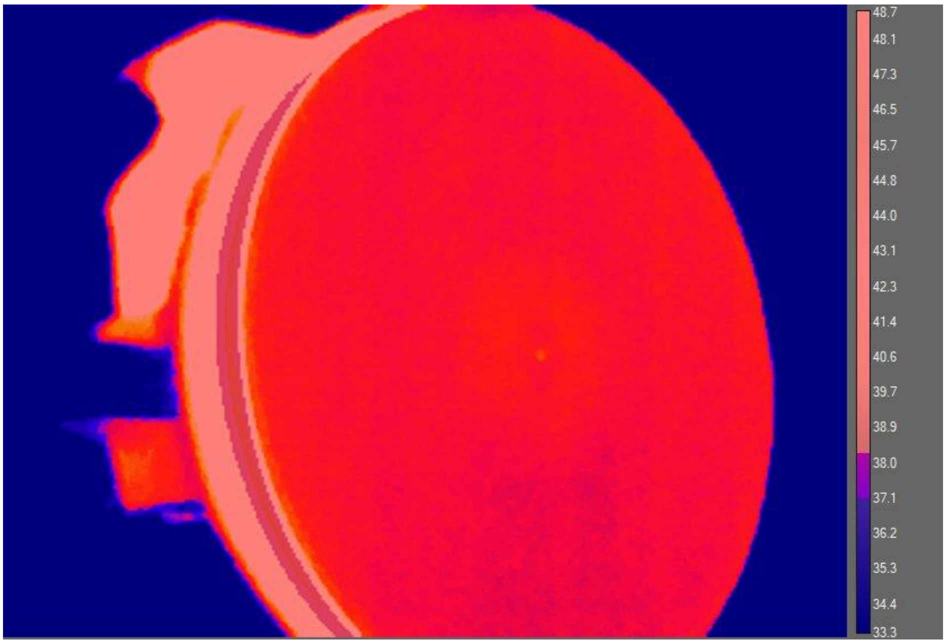

Figure 2.1. Thermal image of the disk just before the start of motor.

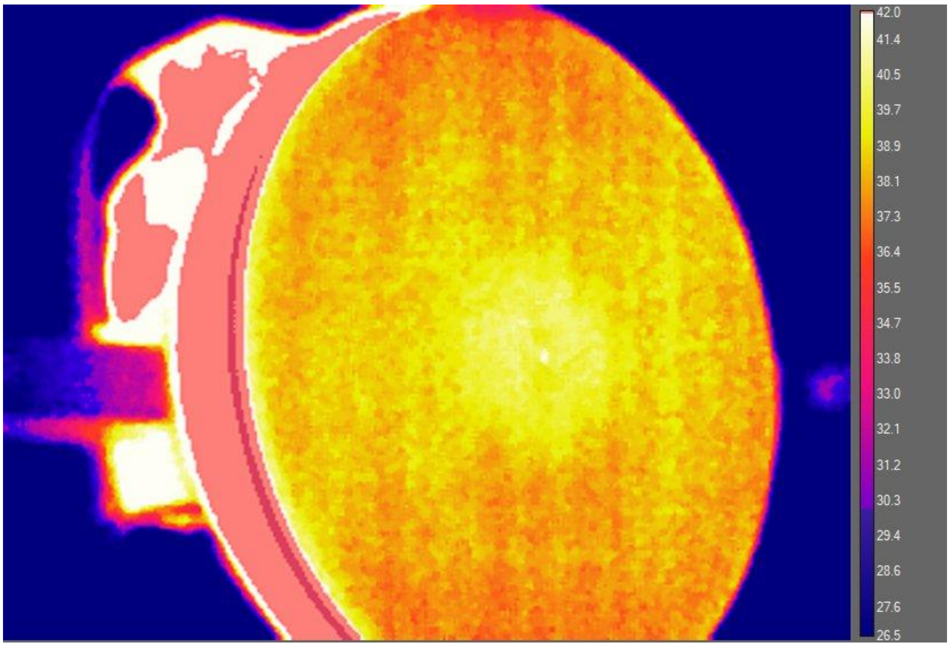

Figure 2.2. Thermal image of the disk just after the motor stopped

Gazili olmak ayrıcalıktır